

**Machine Vision for Improved Human-Robot Cooperation in  
Adverse Underwater Conditions**

A Thesis Proposal

By

**Md Jahidul Islam**

Department of Computer Science and Engineering  
University of Minnesota, Twin Cities

Supervised by **Prof. Junaed Sattar**

June 18, 2022

# Abstract

Visually-guided underwater robots are widely used in numerous autonomous exploration and surveillance applications alongside humans for cooperative task execution. However, underwater visual perception is challenging due to marine artifacts such as poor visibility, lighting variation, scattering, etc. Additionally, chromatic distortions and scarcity of salient visual features make it harder for an underwater robot to visually interpret its surroundings to effectively assist its companion diver during an underwater mission. In this paper, we delineate our attempts to address these challenges by designing novel and improved vision-based solutions. Specifically, we present robust methodologies for autonomous diver following, human-robot communication, automatic image enhancement, and image super-resolution. We depict their algorithmic details and describe relevant design choices to meet the real-time operating constraints on single-board embedded machines. Moreover, through extensive simulation and field experiments, we demonstrate how an autonomous robot can exploit these solutions to understand human motion and hand gesture-based instructions even in adverse visual conditions. As an immediate next step, we want to focus on relative pose estimation and visual attention modeling of an underwater robot based on its companion humans' body-pose and temporal activity recognition. We believe that these autonomous capabilities will facilitate a faster and better interpretation of visual scenes and enable more effective underwater human-robot cooperation.

# Contents

<i>Abstract</i>	i
<b>1 Introduction</b>	<b>2</b>
1.1 Developed Methodologies . . . . .	3
1.2 Proposed Research Direction . . . . .	4
<b>2 Related Work</b>	<b>6</b>
2.1 Autonomous Diver Following . . . . .	6
2.2 Underwater Human-Robot Communication . . . . .	7
2.3 Automatic Image Enhancement . . . . .	8
2.4 Underwater Image Super-resolution . . . . .	9
<b>3 Autonomous Diver Following</b>	<b>11</b>
3.1 Mixed Domain Periodic Motion (MDPM) Tracker . . . . .	11
3.1.1 Modeling the Motion Directions of a Diver . . . . .	11
3.1.2 HMM-based Search-space Pruning . . . . .	13
3.1.3 Frequency Domain Detection . . . . .	14
3.2 Deep Diver Detection . . . . .	14
3.2.1 CNN-based Model for Single Diver Detection . . . . .	15
3.2.2 Allowing Multiple Detections . . . . .	15
3.2.3 State-of-the-art Object Detectors . . . . .	16
<b>4 Human-Robot Communication</b>	<b>17</b>
4.1 Mapping Hand Gestures to Instruction Tokens . . . . .	17
4.2 Hand Gesture Recognition and Instruction Generation . . . . .	19
4.2.1 Region Selection . . . . .	19
4.2.2 CNN-based Model for Hand Gesture Recognition . . . . .	20
4.2.3 Deep Visual Detectors for Hand Gesture Recognition . . . . .	21
4.3 FSM-based Gesture to Instruction Decoder . . . . .	21
<b>5 Automatic Image Enhancement</b>	<b>22</b>
5.1 FUNIE-GAN Architecture . . . . .	22
5.2 Objective Function Formulation . . . . .	23
5.2.1 Paired Training . . . . .	24
5.2.2 Unpaired Training . . . . .	24

5.3	EUVP Dataset . . . . .	25
<b>6</b>	<b>Underwater Image Super-Resolution</b>	<b>26</b>
6.1	Deep Residual Multiplier (DRM) . . . . .	26
6.2	SRDRM and SRDRM-GAN Architecture . . . . .	27
6.3	Objective Function Formulation . . . . .	27
6.4	USR-248 Dataset . . . . .	28
<b>7</b>	<b>Implementation Details and Evaluation</b>	<b>30</b>
7.1	Systems: Robots and Embedded Platforms . . . . .	30
7.2	Systems: Model Training Pipeline . . . . .	31
7.2.1	Dataset Preparation . . . . .	31
7.2.2	Implementation and Training . . . . .	32
7.3	Experiments and Results . . . . .	32
7.3.1	Performance Evaluation: MDPM Tracker . . . . .	33
7.3.2	Performance Evaluation: Deep Diver Detection . . . . .	34
7.3.3	Field Experiments: Autonomous Diver Following . . . . .	35
7.3.4	Performance Evaluation: Robo-Chat-Gest . . . . .	37
7.3.5	Field Experiments: Robo-Chat-Gest . . . . .	38
7.3.6	User Study: Human-Robot Communication . . . . .	39
7.3.7	Qualitative Evaluation: FUnIE-GAN . . . . .	41
7.3.8	Quantitative Evaluation: FUnIE-GAN . . . . .	43
7.3.9	User Study: Automatic Image Enhancement . . . . .	44
7.3.10	Qualitative Evaluation: SRDRM and SRDRM-GAN . . . . .	46
7.3.11	Quantitative Evaluation: SRDRM and SRDRM-GAN . . . . .	47
<b>8</b>	<b>Proposed Research Direction</b>	<b>49</b>
8.1	Simultaneous Image Enhancement and Super-Resolution . . . . .	49
8.2	Robot-to-robot Relative Pose Estimation from Human Pose . . . . .	50
8.2.1	Background . . . . .	52
8.2.2	Preliminary Results: Structure from Motion using Human Pose . . . . .	52
8.3	Visual Attention Modeling . . . . .	54
8.3.1	Background . . . . .	54
8.3.2	Desired Capabilities . . . . .	55
<b>9</b>	<b>Conclusion</b>	<b>56</b>
<b>A</b>		<b>70</b>
A.1	Recursive formulation of $\mu^*(T)$ . . . . .	70
A.2	Algorithm for finding optimal motion direction ( $v^*$ ) . . . . .	70
<b>B</b>		<b>71</b>
B.1	Standard deep visual object detection models . . . . .	71

<b>C</b>	<b>72</b>
C.1 Instruction format in Robo-Chat-Gest . . . . .	72
C.2 Generating instructions using hand gestures . . . . .	72
<b>D</b>	<b>73</b>
D.1 Standard performance metrics for image-quality analysis . . . . .	73
<b>E</b>	<b>74</b>
E.1 Additional qualitative results for SRDRM and SRDRM-GAN . . . . .	74
E.2 Additional qualitative results for SRDRM and SRDRM-GAN . . . . .	75
E.3 Additional quantitative results for SRDRM and SRDRM-GAN . . . . .	75

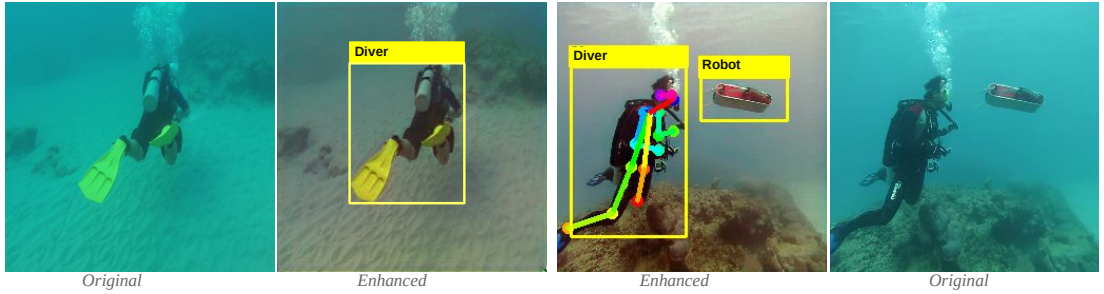
# Chapter 1

## Introduction

Underwater robotics is an area of increasing importance, with existing and emerging applications ranging from inspection and surveillance to data collection and mapping tasks. Since truly autonomous underwater navigation is still an open problem, underwater missions often require a team of human divers and autonomous robots to cooperatively perform tasks. The human divers typically lead the mission and operate the robots during task execution [1]. Such situations arise in numerous important applications such as undersea pipeline and ship-wreck inspection, marine life and seabed monitoring, and many other exploration activities [2, 3]. Without sacrificing the generality of the applications, we consider a single-robot setting where a human diver leads and interacts with the robot at certain stages of an underwater mission. The robot follows the diver and performs the instructed tasks during the operation. Such semi-autonomous behavior of a mobile robot with human-in-the-loop guidance reduces operational overhead by eliminating the necessity of teleoperation.

In human-robot collaborative settings, underwater robots typically rely on vision for exteroceptive perception. A practical alternative is to use acoustic sensors such as sonars and hydrophones. However, they are mainly used for target tracking [4, 5] as they are not suitable for interactive applications. Additionally, acoustic sensors face challenges in coastal waters due to scattering and reverberation. Furthermore, their usage is often limited by government regulations on the sound level in marine environments [2]. On the other hand, cameras are passive sensors, *i.e.*, they do not emit energy and hence are not intrusive to the marine ecosystem [6]. These are compelling reasons why visual sensing is more feasible for underwater applications.

Nevertheless, underwater visual perception is challenging due to the unfavorable visual conditions arising from generally degraded optics caused by factors such as limited visibility, variations in illumination, chromatic distortions, etc. Therefore, visual detection and tracking, servoing, detailed scene understanding, etc., are particularly hard problems in noisy underwater environments. Besides, real-time operating requirements and single-board computational constraints make it a notoriously challenging undertaking to ensure robust yet efficient perception performance. Such adverse operating conditions call for two major characteristics of perception algorithms: robustness to noisy visual data and fast on-board run-time. Consequently, they require careful and intuitive design, efficient implementation, and thorough performance validation by field experiments.



(a) Enhancing underwater image quality and improving visual perception performance; two scenarios are shown: autonomous diver following (left), and human-robot interaction (right).



(b) Communicating instructions to an underwater robot for dynamic task execution.

(c) Finding *interesting* image regions and *zooming in* to have a closer look.

Figure 1.1: A few illustrations of our vision-based solutions for autonomous diver following, hand gesture-based human-robot communication, automatic image enhancement, and image super-resolution. We are currently working on the problem of relative pose estimation and visual attention modeling.

## 1.1 Developed Methodologies

Our research so far has focused on enabling the computational capabilities of a visually-guided underwater robot for it to operate in human-robot cooperative settings amid noisy sensing conditions. As demonstrated in Figure 1.1, we provide efficient vision-based solutions for the following problems:

- **Autonomous diver following:** We develop two efficient methodologies for an underwater robot to visually detect and follow its companion diver. The first method detects the motion directions of a diver by keeping track of their positions through the image sequences over time. In this method [7], a Hidden Markov Model (HMM) is designed to filter the search space of all potential motion directions relying on image intensities in the spatial domain. The diver’s motion signature is subsequently detected in a sequence of non-overlapping image sub-windows exhibiting human swimming patterns in the frequency domain. The second method [1] uses deep visual features to detect divers in the RGB image space. In this method, a Convolutional Neural Network (CNN)-based model is trained on a large dataset of hand-annotated images that we collected from various field experiments [8]. The trained model is invariant to scale, color, and appearance of divers; additionally, it is robust to noise and image distortions [2, 9].
- **Human-robot communication:** Then we develop a simple interaction framework where a diver can use a set of intuitive and meaningful hand gestures to program new instructions

for the accompanying robot or reconfigure existing program parameters *on-the-fly*. In the proposed system [10], a CNN-based model is designed for hand gesture recognition; we also explore the usability of state-of-the-art deep object detectors. Once the hand gestures are recognized, a finite-state machine-based deterministic model efficiently performs the gesture-to-instruction mapping. These mapping rules are intuitively designed so that they can be easily interpreted and adopted by the divers [8]. The major advantage of this design is that a diver can communicate with underwater robots in a natural way using their hands (see Figure 1.1b), without using artificial tags (*e.g.*, AR-tags [11]) or requiring memorization of a complex set of language rules.

- **Automatic image enhancement:** Next, we design a conditional Generative Adversarial Network (GAN)-based model for underwater image enhancement in real-time. In the proposed model [12], we formulate an objective function that evaluates the perceptual image quality based on its global content, color, and local style information. For supervised training, we prepare a large-scale dataset of a paired and an unpaired collection of underwater images (of poor and good quality) that are captured during several oceanic explorations and field experiments; we make this dataset publicly available for contemporary researchers. Our trained model automatically enhances underwater images in terms of color, sharpness, and global contrast (see Figure 1.1a); more importantly, the enhanced images provide improved performances for underwater object detection and human pose estimation. Hence, the proposed model can be used as an image processing pipeline by visually-guided underwater robots in real-time applications.
- **Image super-resolution:** Subsequently, we design a deep residual network-based generative model for single image super-resolution (SISR) of underwater imagery [13]. We also provide an adversarial training pipeline for learning SISR from paired data. To supervise the training, we thoroughly prepare a large-scale dataset for  $2\times$ ,  $4\times$ , and  $8\times$  SISR models; we publicly release this dataset as well. Our qualitative and quantitative results suggest that the proposed model provides realistic high-resolution (HR) visualizations for low-resolution (LR) image patches (see Figure 1.1c), which is potentially useful in tracking fast-moving targets, attention modeling, and detailed understanding of underwater scenes. Therefore, visually-guided robots can use this to *zoom in* a particular region of interest for a more detailed perception.

We present the conceptual designs and implementation details of all the above-mentioned methodologies in this paper (in Chapter 3 through Chapter 6). Additionally, we discuss the relevant operational considerations and practicalities involved in their applications. Furthermore, we evaluate their performance and feasibility through extensive qualitative and quantitative experiments. We also perform several field experiments imitating real-world application scenarios; the results and relevant discussions can be found in Chapter 7.

## 1.2 Proposed Research Direction

We now present several research problems that we are currently working on and looking forward to pursuing further. Specifically, we are exploring the following three problems:

- **Simultaneous image enhancement and super-resolution:** We plan to design a single generative model that can simultaneously learn image enhancement and super-resolution from supervised training. Currently, we have two separate models that are used sequentially, *i.e.*, the output of one is propagated as input to another. We aim to achieve a faster inference by designing a single deep generative model.
- **Robot-to-robot relative pose estimation using human pose:** We are formulating a method to determine the 3D relative pose of pairs of communicating robots by using human pose-based key-points as correspondences. The use of mutually visible humans as *markers* can alleviate the problem of having limited natural landmarks in underwater scenes. Our preliminary experiments suggest that human pose-based key-points, once refined, can be used as reliable geometric correspondences for multi-view relative pose estimation. We are investigating more optimized solutions and conducting field experiments. We believe that the proposed estimation method will be useful in multi-robot cooperative settings [14, 15] in feature-deprived (and GPS-denied) underwater environment.
- **Visual attention modeling:** We are also working on designing a deep encoder-decoder model that can learn to predict salient regions in images. Hence, the objective is to filter visual attention to find *interesting* regions in the image space [16, 17]. Such saliency prediction can speed up visual search and facilitate a better scene understanding [18]. In human-robot collaborative settings, a robot can use the saliency map for efficient target localization, human action recognition, etc. Moreover, with spatio-temporal attention modeling, a robot can learn complex decision-making such as learning to imitate human attention behavior, *e.g.*, when to interact, where to look, etc. We are currently exploring all these aspects to implement their underlying computational modules. In the near future, we plan to conduct thorough qualitative and quantitative experiments for performance validation of these modules.

We believe that the above-mentioned features will be extremely useful for effective underwater human-robot collaboration. We present their methodological details, possible use-cases, and some preliminary results in Chapter 8.

# Chapter 2

## Related Work

The underwater domain poses unique challenges for artificial (as well as natural) sensing, particularly more so for vision. Visual perception is difficult for underwater robots because of light scattering, absorption, refraction, and the presence of suspended particulates. These phenomena stimulate poor visibility, variations in lighting, and chromatic distortions. Such adverse conditions call for two major characteristics of a perception algorithm: robustness to noisy sensory data and fast run-time in embedded computing platforms. In the following discussion, we present the existing visual perception methodologies for autonomous diver following and human-robot interaction. Additionally, we present state-of-the-art methods for image enhancement and super-resolution, which are useful to restore underwater image qualities and facilitate improved perception performance.

### 2.1 Autonomous Diver Following

Due to the operational simplicity and fast run-time, simple feature-based trackers [19, 20] are often practical choices for autonomous diver following. For instance, color-based tracking algorithms perform binary image thresholding based on the color of a diver’s flippers or suit. The thresholded binary image is then refined to track the centroid of the target (diver) using algorithms such as mean-shift, particle filters, etc. Ensemble learning methods such as Adaptive Boosting (AdaBoost) has also been used for diver tracking [21]; AdaBoost learns a strong tracker from a large number of simple feature-based trackers. Such ensemble methods are proven to be computationally inexpensive yet highly accurate in practice. Optical flow-based methods can also be utilized to track diver’s motion from one image frame to another. Optical flow is typically measured between two temporally ordered frames using the well-known Horn and Schunk formulation [22] driven by brightness and smoothness assumptions on the image derivatives. Therefore, as long as the target motion is spatially and temporally smooth, optical flow vectors can be reliably used for detection. Several other feature-based tracking algorithms and machine learning techniques have been investigated for diver tracking and underwater object tracking in general. However, these methods are applicable mostly in favorable visual conditions, *e.g.*, in clear visibility and favorable lighting conditions.

Color distortions and low visibility issues are common in deep water scenarios. It is shown in [23] that the human swimming cues in the frequency domain are stable and regular in noisy

conditions. Specifically, intensity variations in the spatio-temporal domain along a diver’s swimming direction have identifiable signatures in the frequency domain. These intensity variations caused by a diver’s swimming gait tend to generate high-energy responses in the 1-2 Hz frequency range. This inherent periodicity can be used as a cue for robust detection in noisy conditions. We generalize this idea in order to track arbitrary motions; our proposed tracker uses spatial-domain features to keep track of a diver’s potential motion directions using a Hidden Markov Model (HMM). Subsequently, it inspects the frequency-domain responses along those motion directions to find the most probable one to contain a diver’s swimming trajectory. We name this algorithm the *Mixed Domain Periodic Motion (MDPM)* tracker [7].

The Convolutional Neural Network (CNN)-based deep models can further improve the generalization performance by learning a feature representation from the image-space. The extracted features are used as inputs to the detector (*i.e.*, fully-connected layers); this end-to-end training process significantly improves the detection performance compared to using hand-crafted features. Once trained with sufficient data, these models are quite robust to occlusion, noise, and color distortions [24]. Despite the robust performance, the applicability of these models to real-time applications is often limited due to their slow running time on embedded devices. We investigate the performances and feasibility of the state-of-the-art object detectors for diver following applications. We also design a CNN-based model [1] that achieves robust detection performance in addition to ensuring that the real-time operating constraints are met.

## 2.2 Underwater Human-Robot Communication

Modulating robot motion based on human input in the form of speech, hand gestures, or keyboard interfaces has been explored extensively for terrestrial environments [25, 26, 27]. However, most of these human-robot communication modules are not readily applicable in underwater applications due to environmental and operational constraints [28]. Since visual communication is a more feasible and operationally simpler method [2], several of visual diver-robot interaction frameworks have been developed in the literature.

A gesture-based framework for underwater visual servo control was introduced in [29], where a human operator on the surface was required to interpret human gestures and modulate the corresponding robot movements. Due to challenging underwater visual conditions [28] and a lack of robust gesture recognition techniques, fiducial markers were used instead of free-form hand gestures as they are efficiently and robustly detectable under noisy conditions. In this regard, the most commonly used fiducial markers have been those with square, black-and-white patterns providing high contrast, such as AR-Tags [11] and April-Tags [30], among others. Circular markers with similar patterns such as the Photomodeler Coded Targets Module system and Fourier Tags [31] have also been used in practice.

Robo-Chat [32] is a visual language proposed for underwater diver-robot communication, for which divers use a set of AR-Tag markers printed on cards to display predefined sequences of symbolic patterns to the robot. These symbol sequences are mapped to commands using a set of grammar rules defined for the language. These grammar rules include both terse imperative action commands as well as complex procedural statements. Despite its utility, Robo-Chat suffers from two critical weaknesses. Firstly, because a separate marker is required for each

*token* (i.e., a language component), a large number of marker cards need to be securely carried during the mission, and divers have to search for the cards required to formulate a syntactically correct script; this whole process imposes a rather high cognitive load on the diver. Secondly, the symbol-to-instruction mapping is inherently counter-intuitive, which makes it inconvenient for rapidly programming a robot. The first limitation is addressed in [33], in which a set of discrete motions using a pair of fiducial markers is interpreted as a robot command. Different features such as shape, orientation, and size of these gestures are extracted from the observed motion and mapped to the robot instructions. Since more information is embedded in each trajectory, a large number of instructions can be supported using only two fiducial markers. However, this method introduces additional computational overhead to track the marker motion and needs robust detection of shape, orientation, and size of the motion trajectory. Furthermore, these problems are exacerbated by the fact that both robots and humans are suspended in a six-degrees-of-freedom (6-DOF) environment. Also, the symbol-to-instruction mapping remains unintuitive.

Since the traditional method for communication between scuba divers is with hand gestures, instructing a robot using similar hand gestures is more intuitive and flexible than using fiducial markers. There exist several hand gesture-based HRI frameworks [25, 26, 27] for terrestrial robots. Additionally, recent visual hand gesture recognition techniques [34, 35] based on CNNs are highly accurate and robust to noise and visual distortions [9]. A number of such visual recognition and tracking techniques have been successfully used for underwater tracking [24] and have proven to be more robust than other purely feature-based methods [2]. However, the feasibility of these models for hand gesture-based human-robot communication has not yet been explored in-depth, which we attempt to address in [10]. Moreover, we demonstrate that off-the-shelf deep visual detection models [36] can be utilized in our framework to ensure robust performance.

## 2.3 Automatic Image Enhancement

Automatic image enhancement is a well-studied problem [37, 38] in the domains of computer vision, robotics, and signal processing. The deep CNN-based models provide state-of-the-art performance for problems such as image colorization [39] and color/contrast adjustment [40]. Additionally, CNN-based residual and recurrent models are known to provide very good performance for image deblurring or dehazing [41], rain removal [42], and sparse inpainting [43]. These models learn a sequence of non-linear filters from a large number of paired training data, which provide significantly better performance compared to using hand-crafted filters. Moreover, the GAN-based models [44] have shown great success for style transfer [45] and image-to-image translation problems [46]. They employ a two-player min-max game where the ‘generator’ tries to fool the ‘discriminator’ by generating *fake* images that appear to be sampled from the *real* distribution. Simultaneously, the discriminator tries to get better at discarding fake images and eventually (in equilibrium) the generator learns to model the underlying distribution. Although such adversarial training can be unstable (typically happens when the discriminator becomes too good and the generator gives up), several improvements and choices of loss functions are proposed in the literature. For instance, Wasserstein GAN [47] improves the training

stability by using the earth-mover distance to measure the distance between the data distribution and the model distribution. Energy-based GANs [48] also improve training stability by modeling the discriminator as an energy function, whereas the Least-Squared GAN [49] addresses the vanishing gradients problem by adopting a least-square loss function for the discriminator. On the other hand, conditional GANs [50] allow constraining the generator to produce samples that follow a particular pattern or belong to a specific class, which is particularly useful in image-to-image translation problems. Specifically, conditional GANs are used to learn a pixel-to-pixel (Pix2Pix) mapping [46] between an arbitrary input domain (*e.g.*, distorted images) and the desired output domain (*e.g.*, enhanced images).

A major limitation of the above-mentioned models is that they require paired training data, which may not be available or can be difficult to acquire for many practical applications. The two-way GANs (*e.g.*, CycleGAN [51], DualGAN [52], etc.) solve this problem by using a ‘cycle consistency loss’ that allows learning the mutual mappings between two domains from unpaired data. Such models have been effectively used for unpaired learning of perceptual image enhancement [53, 54] as well. Furthermore, Ignatov *et al.* [55] showed that additional loss-terms for preserving the image-based content and texture information improve the performance of image quality enhancement using GANs.

Image enhancement techniques for underwater imagery are relatively less advanced, mostly due to the lack of large-scale datasets that contain images of multiple perceptual qualities of the same scenes. Traditional methods avoid instance-based learning by using a series of bi-lateral and tri-lateral filters [56, 57] in order to reduce noise and improve global contrast. In recent years, researchers have investigated the use of synthetic images [58, 59] to prepare paired training data and reported reasonable success. For instance, Li *et al.* [60] generate synthetic underwater images by aligning them with in-air RGBD images; the synthetic images are then used to prepare paired instances for adversarial training. Moreover, Fabbri *et al.* [9] perform style-transfer using CycleGAN to generate distorted underwater images for preparing paired training instances. However, performance of these methods for enhancing perceptual image quality heavily depend on the quality and neutrality of the synthetically generated images. Besides, they are often computationally too demanding to generate fast inference on single-board robotic platforms; consequently, their applicability for improving real-time underwater visual perception is limited. We attempt to address these aspects in [12].

## 2.4 Underwater Image Super-resolution

Single Image Super-resolution (SISR) is also a well-studied problem [61, 62, 63] in the area of signal processing and computer vision. Some of the classical SISR methods include statistical methods [64, 65, 66], patch-based methods [67, 68, 69], sparse representation-based methods [70], random forest-based method [71], etc. In recent years, with the rapid development of deep learning-based techniques, this area of research has been making incredible progress. In the pioneering work, Dong *et al.* [72] proposed a three-layer CNN-based end-to-end model named SRCNN, that can learn a non-linear LR-HR mapping without requiring any hand-crafted features. Soon after, Johnson *et al.* [73] showed that replacing the per-pixel loss with a perceptual loss (that quantifies image quality) gives better results for CNN-based SISR models. On the

other hand, Kim *et al.* proposed deeper networks such as VDSR [74], DRCN [75] and used contemporary techniques such as gradient clipping, skip connection, and recursive-supervision in order to improve the training further. Moreover, the sparse coding-based networks [76], residual block-based networks (*e.g.*, EDSR [77], DRRN [78]), and other CNN-based models [79], [80] have been proposed that outperform SRCNN for SISR. These methods, however, have rather complex training pipelines, and are often prone to poor performance for large scaling factors (*i.e.*,  $4\times$  and higher). Thus far, researchers have been trying to address these issues by using Laplacian pyramid-based networks (LapSRN) [81], dense skip connections (SRDenseNet) [82], deep residual networks (RDN) [83], etc.

The CNN-based SISR models learn a sequence of non-linear filters from a large number of training images. This end-to-end learning of LR-HR mapping provide significantly better performance [84] compared to using hand-crafted filters, or traditional methods based on bicubic interpolation. On the other hand, the GAN-based models can recover finer texture details [85, 86, 87] while super-resolving at large up-scaling factors. For instance, Ledig *et al.* showed that SRGAN [88] can reconstruct high-frequency details for an up-scaling factor of 4. Moreover, ESRGAN [89] incorporates a residual-in-residual dense block that improves the SISR performance. Furthermore, DeblurGAN [90] uses conditional GANs [50] that allow constraining the generator to learn a pixel-to-pixel mapping [46] within the LR-HR domain. Recently, inspired by the success of CycleGAN [51] and DualGAN [52], Yuan *et al.* [91] proposed a cycle-in-cycle GAN-based model that can be trained using unpaired data. However, such unsupervised training of GAN-based SISR models are prone to instability and often produce inconsistent results.

SISR techniques for underwater imagery, on the other hand, are significantly less studied. As mentioned in the previous section, this is mostly due to the lack of large-scale datasets (containing LR-HR pairs of images) that capture the distribution of the unique distortions prevalent in underwater imagery. The existing datasets are only suitable for underwater object detection [8] and image enhancement [12] tasks, as their image resolution is typically limited to  $256 \times 256$ , and they often contain synthetic images [9]. Consequently, the performance and applicability of existing and novel SISR models for underwater imagery have not been explored in depth. Nevertheless, a few research attempts have been made for underwater SISR which primarily focus on reconstructing better quality underwater images from their noisy or blurred counterparts [92, 93, 94]. Other similar approaches have used SISR models to enhance underwater image sequence [95], and to improve fish recognition performance [96]. Although these models perform reasonably well for the respective applications, there is still significant room for improvement to match the state-of-the-art SISR performance. We attempt to address these aspects in [13].

## Chapter 3

# Autonomous Diver Following

In the following sections, we present two methodologies for an underwater robot to visually detect and track a diver. Once the diver is localized in the image space, a visual servoing controller [97] regulates motion commands in 6-DOF space in order to follow the diver in a smooth trajectory. We will further discuss the operation of our visual servoing controller in Section 7.3.3.

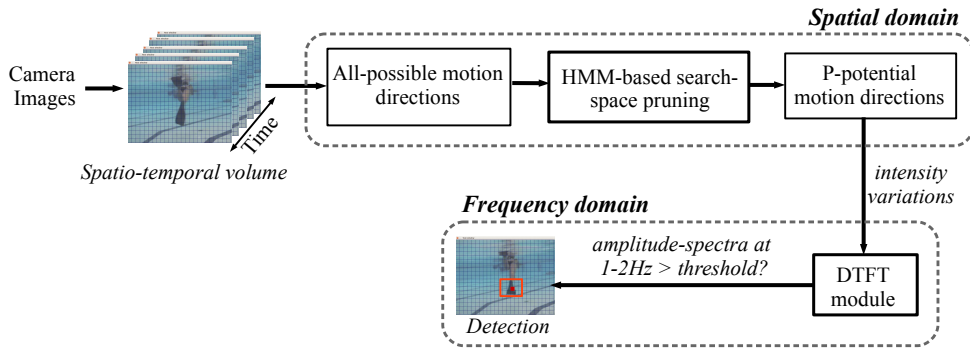


Figure 3.1: An outline of the MPDM tracker.

### 3.1 Mixed Domain Periodic Motion (MDPM) Tracker

MDPM tracker uses both spatial domain and frequency domain features to visually track a diver's motion over time. As illustrated in Figure 3.1, the motion direction of a diver is modeled as a sequence of non-overlapping image sub-windows over time, and it is quantified as a vector of intensity values corresponding to those sub-windows. These captured intensity values (for all possible motion directions) are then exploited by an HMM-based pruning method to discard the motion directions that are unlikely to be the direction where the diver is swimming. Subsequently, the potentially optimal motion directions are inspected in the frequency domain. A high amplitude-spectra in the 1-2 Hz frequency band is an indicator of a human swimming motion, which is used to locate the diver in the image space.

#### 3.1.1 Modeling the Motion Directions of a Diver

First, the image frame at time-step  $t$  is divided into a set of  $M$  rectangular windows labeled as  $w_0^{(t)}, w_1^{(t)}, \dots, w_{M-1}^{(t)}$ . Then, as demonstrated in Figure 3.2, the motion directions are quantified

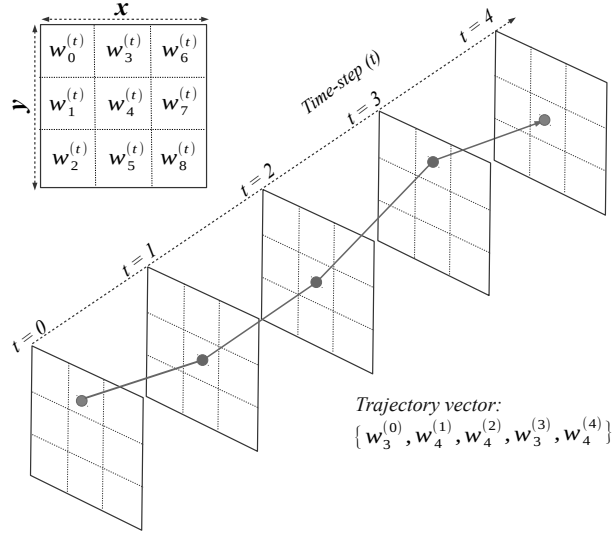


Figure 3.2: A simple scenario with the image space divided into  $M=9$  windows is shown on the top-left corner. One possible motion direction is shown on the bottom, where the corresponding trajectory vector for  $T=5$  time-steps is  $v = \{w_3^{(0)}, w_4^{(1)}, w_4^{(2)}, w_3^{(3)}, w_4^{(4)}\}$ .

as vectors of the form  $v = \{w_i^{(0)}, w_i^{(1)}, \dots, w_i^{(t)}, \dots, w_i^{(T-1)}\}$ . Here,  $T$  stands for the *slide-size* and  $w_i^{(t)}$  denotes one particular window on the  $t^{th}$  frame, *i.e.*,  $i \in [0, M - 1]$  and  $t \in [0, T - 1]$ . We call  $v$  the *trajectory vector*. Now, let  $x_v$  denote the *intensity vector*<sup>1</sup> corresponding to the trajectory vector  $v$ . We interpret this sequence of  $T$  numbers in  $x_v$  as values of a discrete aperiodic function defined on  $t$ . This interpretation allows us to take the Discrete Time Fourier Transform (DTFT) of  $x_v$  and get a  $T$ -periodic sequence of complex numbers which we denote by  $X_v$ . The values of  $X_v$  represents the discrete frequency components of  $x_v$  in the frequency domain. The standard equations [98] that relate the spatial and frequency domains through a Fourier Transform are:

$$X_v[k] = \sum_{t=0}^{T-1} x_v[t] e^{-j2\pi tk/N}, \quad (k \in [0, N - 1]); \text{ and} \quad (3.1)$$

$$x_v[t] = \frac{1}{N} \sum_{k=0}^{N-1} X_v[k] e^{j2\pi tk/N}. \quad (3.2)$$

As mentioned earlier, we try to capture the periodic motion of the diver in  $x_v$  by keeping track of the variations of intensity values along  $v$ . Then, we take the DTFT of  $x_v$  to inspect its amplitude-spectra of the discrete frequency components. The flippers of a human diver typically oscillate at 1-2 Hz frequencies [23]. Hence, our goal is to find the motion direction  $v$  for which the corresponding intensity vector  $x_v$  produces maximum amplitude-spectra within 1-2 Hz in its frequency domain ( $X_v$ ). Therefore, if  $F(v)$  is the function that performs DTFT on  $x_v$  to generate  $X_v$  and subsequently finds the amplitude-spectra with high energy responses, we can formulate the following optimization problem by predicting the motion direction of a diver as:

$$v^* = \arg \max_v F(v). \quad (3.3)$$

The search-space under consideration in optimizing Equation 3.3 is of size  $M^T$ , as there are  $M^T$  different trajectory vectors considering  $M$  number of windows and slide-size  $T$ . Performing  $O(M^T)$  computations in a single detection is computationally too expensive for real-time

<sup>1</sup>We refer to *intensity value* of a window as the Gaussian-filtered average intensity of that window

implementation. Besides, a large portion of all possible motion directions is irrelevant due to the limited body movement capabilities of human divers. Consequently, we adopt a search-space pruning step to eliminate these unfeasible solutions.

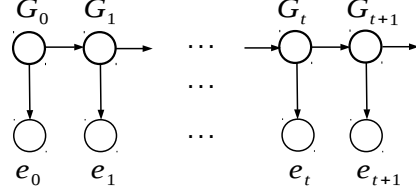


Figure 3.3: An HMM-based representation for the search-space of all possible motion directions. Here, the observed states  $(e_t)$  represent an *evidence vector* containing intensity values for  $w_i^{(t)}$ ,  $i \in [0, M - 1]$ , whereas the hidden states  $G_t$  represent the probabilities that  $w_i^{(t)}$  contains (part-of) a diver's flippers.

### 3.1.2 HMM-based Search-space Pruning

We have discussed that the periodic variations of intensity values, being transformed into the frequency domain, carry information about the swimming direction of the diver. On the other hand, in the spatial domain, the intensity value (or RGB values) of a particular window suggests whether (a part of) the diver's body or flippers might be present in that window. Therefore, we can exploit this information to assign some degree of confidence that the diver is present in a particular window. We do this by first using prior knowledge about the color of the diver's flipper to set an intensity range  $R$ . We choose  $R$  such that the probability of the diver's flipper being present in a window  $w_i^{(t)}$  at time-step  $t$  is given by the following equation:

$$P\{G_t = w_i^{(t)} | e_t\} \propto \frac{1}{Dist(I(w_i^{(t)}), R)}. \quad (3.4)$$

Here,  $e_t$  is the *evidence vector* that contains intensity values for window  $w_i^{(t)}$ , whereas  $Dist(I(w_i^{(t)}), R)$  measures the numeric distance between the intensity of  $w_i^{(t)}$  and the intensity range  $R$ . As depicted in Figure 3.3, we define the HMM structure by considering  $G_t$  as a *hidden state* (as we want to predict which windows contain the diver's flippers) and  $e_t$  as an *observed state* (as we can observe the intensity values of these windows) at time-step  $t$ . Additionally, we consider it unlikely that the diver's flippers will move too far away from a given window in a single time-step. Based on these assumptions, we define the following Markovian transition probabilities:

$$\begin{aligned} & P\{G_{t+1} = w_i^{(t+1)} | G_0 = w_i^{(0)}, G_1 = w_i^{(1)}, \dots, G_t = w_i^{(t)}\} \\ &= P\{G_{t+1} = w_i^{(t+1)} | G_t = w_i^{(t)}\} \propto \frac{1}{Dist(w_i^{(t+1)}, w_i^{(t)})}; \end{aligned} \quad (3.5)$$

$$P\{e_t | G_t = w_i^{(t)}\} = \begin{cases} 1 - \epsilon & \text{if } I(w_i^{(t)}) \in R \\ \epsilon & \text{otherwise.} \end{cases} \quad (3.6)$$

In our implementation, we take  $\epsilon = 0.1$ , and adopt an intensity-based range  $R$  to define  $P\{G_t = w_i^{(t)} | e_t\}$ ; color-based ranges (in RGB-space or HSV-space) can also be adopted instead. One advantage of using intensity-based range is that the intensity values of each window are already available in the trajectory vector and therefore no additional computation is required. We use this HMM-based setup to predict *the most likely sequence of states*  $(G_0, \dots, G_{T-1})$  that

leads to a given state  $G_T = w_i^{(T)}$  at time-step  $t$ . In terms of the parameters and notations mentioned above, this is defined as follows:

$$\begin{aligned}\mu^*(T) &= \arg \max_{w_i^{(0)}, \dots, w_i^{(T-1)}} P\left\{G_0 = w_i^{(0)}, \dots, G_T = w_i^{(T)} \mid e_0, \dots, e_T\right\} \\ &= \arg \max_{w_i^{(0:T-1)}} P\left\{G_{0:T} = w_i^{(0:T)} \mid e_{0:T}\right\}.\end{aligned}\quad (3.7)$$

Here, we adopted the short-form notations in the second line for convenience. Now, using the properties of the Bayesian chain rule and Markovian transition [99], a recursive definition of  $\mu^*(T)$  can be obtained as follows (see Appendix A.1 for the derivation):

$$\mu^*(T) = P\left\{e_T \mid G_T = w_i^{(T)}\right\} \times \arg \max_{w_i^{(T-1)}} \left( P\left\{G_T = w_i^{(T)} \mid G_{T-1} = w_i^{(T-1)}\right\} \times \mu^*(T-1) \right). \quad (3.8)$$

Using this recursive definition of  $\mu^*(T)$ , we can efficiently keep track of the most likely sequence of states over  $T$  time-steps. This sequence of states corresponds to a sequence of windows, which is effectively the desired trajectory vector. However, a pool of such trajectory vectors is needed so that we can inspect the frequency responses to choose the one having the strongest response. Therefore, we choose the  $p$  most likely sequences of states, which we define as  $\mu^*(T, p)$ . Here,  $p$  is the *pool-size*. Finally, we rewrite the problem definition in Equation 3.3 as follows:

$$v^* = \arg \max_{\mu \in \mu^*(T, p)} F(\mu). \quad (3.9)$$

### 3.1.3 Frequency Domain Detection

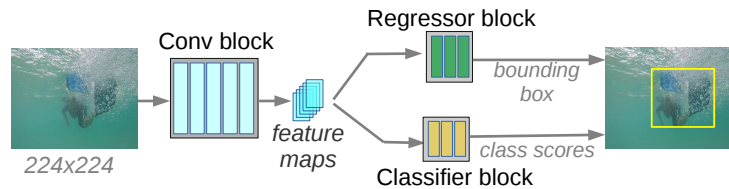
The algorithmic procedure for finding  $v^*$  is outlined in Appendix A.2. At each detection cycle, we first find the  $p$  most potential motion directions (*i.e.*, trajectory vectors) through the HMM-based pruning mechanism. We do this efficiently using the notion of *dynamic programming*. It requires  $\mathcal{O}(M^2)$  operations to update the dynamic table of probabilities at each detection cycle. Once the potential trajectory vectors are found, we perform DTFT to observe their frequency domain responses. The trajectory vector producing the highest amplitude-spectra at 1-2 Hz frequencies is selected as the optimal solution. DTFT can be performed very efficiently; for instance, the run-time of a Fast Fourier Transform algorithm is  $\mathcal{O}(T \times \log T)$ . Therefore, we need only  $\mathcal{O}(p \times T \times \log T)$  operations for inspecting all potential trajectory vectors. Additionally, the approximated location of the diver is readily available in the solution; therefore, no additional computation is required for tracking.

## 3.2 Deep Diver Detection

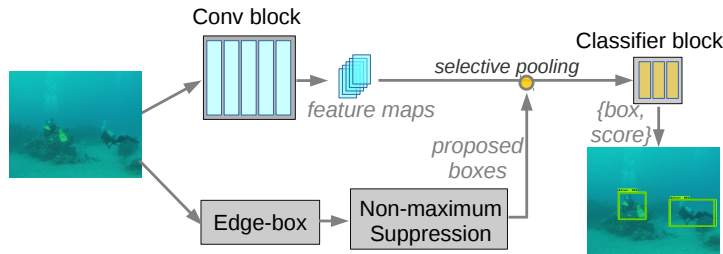
A major limitation of MDPM tracker is that it does not model the appearance of a diver, it only detects the periodic signals pertaining to a diver's flipping motion. Besides, its performance is affected by the diver's swimming trajectory (straight-on, sideways, etc.), the color of wearables, etc. We try to address these issues and ensure robust detection performance by using a CNN-based deep model for diver detection. We also demonstrate the feasibility of using state-of-the-art deep object detection models [36] for multi-diver detection in quasi-real-time.

### 3.2.1 CNN-based Model for Single Diver Detection

Figure 3.4a shows a schematic diagram of the proposed CNN-based diver detection model. It is particularly designed for detecting a single diver in RGB image space. Five convolutional layers are used to extract the spatial features by learning a set of convolutional kernels. The extracted features are then fed to the classifier and regressor block for detecting a diver and localizing the corresponding bounding box, respectively. Both the classifier and regressor block consist of three fully connected layers. Therefore, the task of the regressor block is to locate a potential diver in the image space, whereas the classifier block provides the confidence scores associated with that detection. Detailed network parameters and dimensions are specified in Table 3.1.



(a) The base model for single diver detection.



(b) Allowing detection of multiple divers by using a region selector named Edge-box [100].

Figure 3.4: A schematic diagram of the proposed CNN-based model for diver detection in image space.

As demonstrated in Table 3.1, the proposed model uses a sparse regressor block for single object localization rather than using a computationally expensive Region Proposal Network (RPN). The idea is to facilitate a fast on-board inference for single diver detection as *single-robot-single-diver* interaction framework is typically adopted in practice. Moreover, only a few object categories (e.g., diver, robot, coral reefs, etc.) are relevant in underwater human-robot collaborative applications. Therefore, unlike the general-purpose deep visual models, we avoid using RPNs to gain much faster run-time for single instance detection of a few object categories.

### 3.2.2 Allowing Multiple Detections

Although following a single diver is the most common diver-following scenario, detecting multiple divers and other objects can be useful in many applications. As shown in Figure 3.4b, we can add multi-object detection capabilities in the proposed model by replacing the regressor with a region selector. In our implementation, we use the state-of-the-art class-agnostic region selector named Edge-box [100]. Edge-box utilizes the image-level statistics like edges and contours to measure *objectness scores* in various prospective regions in the image space. The bounding boxes generated by Edge-box are filtered based on their objectness scores and then non-maxima suppression techniques are applied to get the dominant regions of interest in

Table 3.1: Parameters and dimensions of the CNN model outlined in Figure 3.4. (convolutional block: conv1-conv5, classifier block: fc1-fc3, regression block: rc1-rc3;  $n$ : the number of object categories; \*an additional pooling layer was used before passing the conv5 features-maps to fc1)

Layer	Input feature-map	Kernel size	Strides	Output feature-map
conv1	$224 \times 224 \times 3$	$11 \times 11 \times 3 \times 64$	$[1, 4, 4, 1]$	$56 \times 56 \times 64$
pool1	$56 \times 56 \times 64$	$1 \times 3 \times 3 \times 1$	$[1, 2, 2, 1]$	$27 \times 27 \times 64$
conv2	$27 \times 27 \times 64$	$5 \times 5 \times 64 \times 192$	$[1, 1, 1, 1]$	$27 \times 27 \times 192$
pool2	$27 \times 27 \times 192$	$1 \times 3 \times 3 \times 1$	$[1, 2, 2, 1]$	$13 \times 13 \times 192$
conv3	$13 \times 13 \times 192$	$3 \times 3 \times 192 \times 192$	$[1, 1, 1, 1]$	$13 \times 13 \times 192$
conv4	$13 \times 13 \times 192$	$3 \times 3 \times 192 \times 192$	$[1, 1, 1, 1]$	$13 \times 13 \times 192$
conv5	$13 \times 13 \times 192$	$3 \times 3 \times 192 \times 128$	$[1, 1, 1, 1]$	$13 \times 13 \times 128$
fc1	$4608 \times 1^*$	—	—	$1024 \times 1$
fc2	$1024 \times 1$	—	—	$128 \times 1$
fc3	$128 \times 1$	—	—	$n$
rc1	$21632 \times 1$	—	—	$4096 \times 1$
rc2	$4096 \times 1$	—	—	$192 \times 1$
rc3	$192 \times 1$	—	—	$4n$

the image space. The corresponding feature maps are then fed to the classifier block to predict the object categories. Although we need additional computation for Edge-box, it runs independently and in parallel with the convolutional block; hence, the overall pipeline is still reasonably fast in practice.

### 3.2.3 State-of-the-art Object Detectors

Furthermore, we exploit the state-of-the-art deep object detectors to address the inherent difficulties of underwater visual detection. We use the following four models: Faster R-CNN [101] with Inception V2 [102] as a feature extractor, Single Shot MultiBox Detector (SSD) [103] with MobileNet V2 [104, 105] as a feature extractor, You Only Look Once (YOLO) V2 [106], and Tiny YOLO [107]. These are the fastest (in terms of processing time of a single frame) among the family of current state-of-the-art models for general object detection; we refer to [36, 107] for detailed comparisons of their detection performances and run-times. Appendix B.1 briefly discusses their methodologies and the related design choices in terms of major computational components.

## Chapter 4

# Human-Robot Communication

In this chapter, we present a hand gesture-based underwater human-robot communication framework, which we name *Robo-Chat-Gest*. Robo-Chat-Gest is built on several components: the choice of hand gestures to map to instruction tokens, the robust recognition of hand gestures, and the use of a finite-state machine to enforce the instruction structure and ignore erroneous detection. Each of these components is described in detail in the following sections.

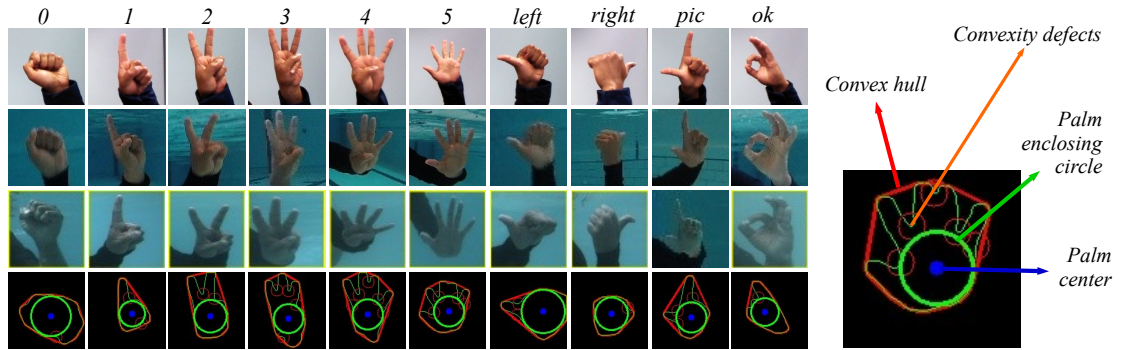


Figure 4.1: The first three rows on the left show a few sample training images for the ten classes of hand gestures used in Robo-Chat-Gest; the bottom row shows the expected hand-contours with different curvature markers for each class of gestures. The annotated curvature markers for a particular example are shown on the right.

### 4.1 Mapping Hand Gestures to Instruction Tokens

Our objective is to design a simple yet expressive framework that can be easily interpreted and adopted by divers for communicating with the robot without memorizing complex language rules. Therefore, we choose a small collection of visually distinctive and intuitive gestures, which would improve the likelihood of robust recognition in degraded visual conditions. Specifically, we use only the ten gestures shown in Figure 4.1; as seen in this figure, each gesture is intuitively associated with the command it delivers. Sequences of different combinations of these gestures formed with both hands are mapped to specific instructions. We concentrate on the following two sets of instructions in Robo-Chat-Gest:

- **Task switching:** This is to instruct the robot to stop the execution of the current pro-

Instruction-token	Type	Hand gestures		Gesture-token {left, right}
		Left	Right	
STOP current-program	Start-token			{0, ok}
HOVER	Task			{5, 5}
FOLLOW me	Task			{5, 1}
Go LEFT	Task			{0, left}
Go RIGHT	Task			{0, right}
Go UP	Task			{right, right}
Go DOWN	Task			{left, left}
EXECUTE Program	Task			{pic, 2}
CONTD current-program	Start-token			{pic, 0}
Take SNAPSHOT	Task			{pic, pic}
N (number)	[0-5]*			{ok, 0-5}
P (parameter number)	[0-5]*			{0-5, pic}
next_digit	indicator			{pic, ok}
Increase	step			{right, pic}
Decrease	step			{left, pic}
Default	step			{ok, pic}
GO	End-token			{ok, ok}

Figure 4.2: The mapping of gesture-tokens to instruction-tokens used in Robo-Chat-Gest.

gram and start a new task specified by the diver, such as hovering, following, or moving left/right/up/down, etc. These commands are atomic behaviors that the robot is capable of executing. An optional argument can be provided to specify the duration of the new task (in seconds). An operational requirement is that the desired programs need to be numbered and known to the robot beforehand.

- **Parameter reconfiguration:** This is to instruct the robot to continue the current program with updated parameter values. This enables underwater missions to continue unimpeded, without interrupting the current task or requiring the robot to be brought to the surface. Here, the requirement is that the tunable parameters need to be numbered and their choice of values needs to be specified beforehand. The robot can also be instructed to take pictures (for some time) while executing the current program.

Robo-Chat-Gest supports a variety of task switching and parameter reconfiguration instructions, which can be extended to accommodate more instructions by simply changing or appending a user-editable configuration file. The hand gesture-to-token mapping is carefully designed so that the robot formulates executable instructions only when intended by the diver. This is done by attributing specific hand gestures as sentinels (*i.e.*, *start*- or *end*-tokens). Figure 4.2 illustrates the gesture to atomic-instruction mapping used in Robo-Chat-Gest. Also in Appendix C.2-C.2, a series of (*start\_token*, *instruction*, *end\_token*) tuples are mapped to their corresponding sequences of *gesture\_tokens* for demonstration.

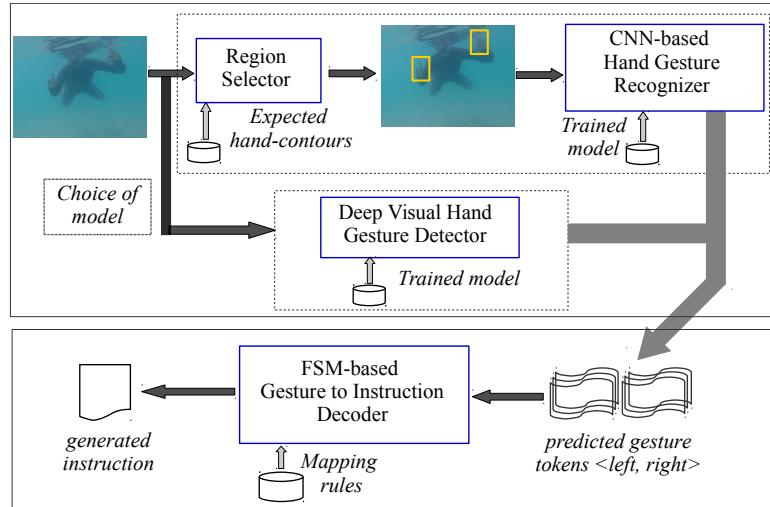


Figure 4.3: An overview of the process of mapping hand gestures to instructions in Robo-Chat-Gest. The top block demonstrates two (choices of) hand gesture recognition systems, and the bottom block depicts a finite-state machine for hand gesture-to-instruction mapping.

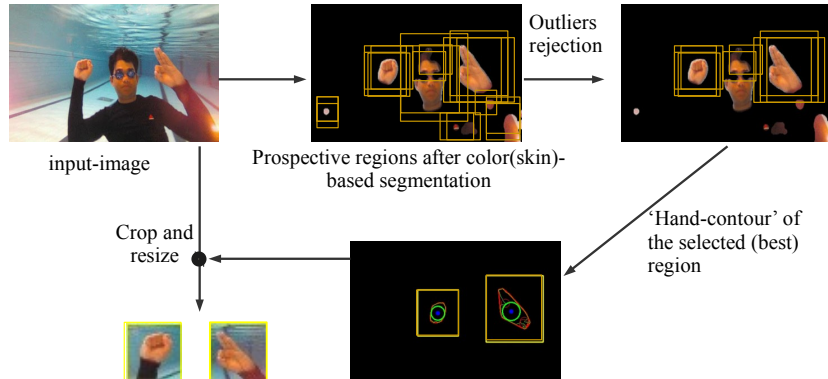


Figure 4.4: Outline of the region selection mechanism shown in Figure 4.3: first, the (skin) color-based segmentation is performed to get potential regions for hand gestures; then, the outlier regions are discarded based on cached information about the previous locations of the hands.

## 4.2 Hand Gesture Recognition and Instruction Generation

Robust mapping of gesture-tokens to instruction-tokens is essential for a gesture-based human-robot communication system in general. In Robo-Chat-Gest, the challenges lie in localizing the hand gestures in the image space, accurately recognizing those hand gestures, and then mapping them to the correct instruction-tokens. We now provide the implementation details of these components in the following sections.

### 4.2.1 Region Selection

To detect gestures, the hand regions need to be cleanly extracted from the image. The CNN-based region proposal networks [101] or classical methods such as Edge-box [100] are known to be robust and highly accurate in segmenting prospective regions for object detection. However, due to their slow running time in embedded platforms, we adopt the classical image processing

techniques to select prospective hand regions in the image space. As illustrated in Figure 4.4, the overall region selection process can be summarized as follows:

- i. First, the camera image (RGB) is blurred using Gaussian smoothing and then filtered in the HSV space for skin-color segmentation [108]. We assume that the diver performs gestures with bare hands; if the diver is to wear gloves, the color thresholding range in the HSV space needs to be adjusted accordingly.
- ii. Contours of the different segmented regions in the filtered image space are then extracted (see Figure 4.1). Subsequently, different contour properties such as convex hull boundary and center, convexity defects, and important curvature points are extracted. We refer readers to [109] for details about the properties and significance of these contour properties. Next, the outlier regions are rejected using cached information about the scale and location of hand gestures detected in the previous frame (if available).
- iii. Finally, the hand contours of potential regions are matched with a bank of hand contours that are extracted from training data (one for each class of hand gestures as shown in the bottom row of Figure 4.1). The final regions for left- and right-hand gestures are selected using the proximity values of the closest contour match [109]; *i.e.*, the region that is most likely to contain a hand gesture is selected.

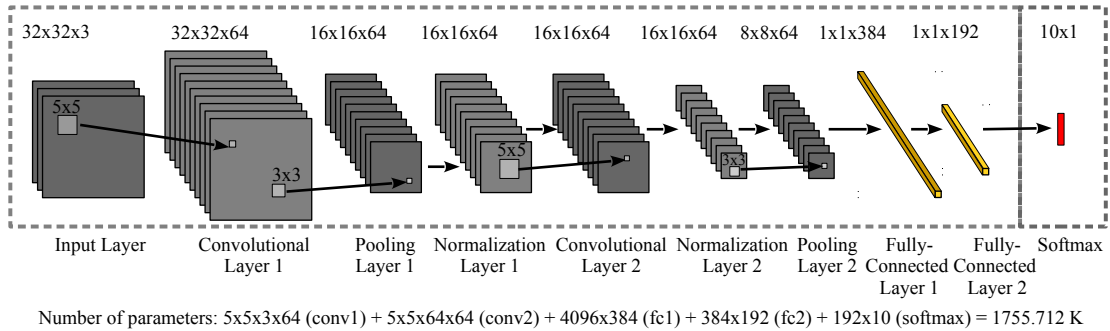


Figure 4.5: Architecture of the CNN model used in Robo-Chat-Gest for hand gesture recognition.

### 4.2.2 CNN-based Model for Hand Gesture Recognition

Following region selection, the cropped and resized  $32 \times 32$  image-patches are fed to a CNN-based model for hand gesture recognition. The architecture of the model is illustrated in Figure 4.5. Two convolutional layers are used for extracting and learning the spatial information within the images. Spatial down-sampling is done by max-pooling, while the normalization layer is used for scaling and re-centering the data before feeding it to the next layer. The extracted feature-maps are then fed to the fully connected layers to learn decision hyper-planes within the distribution of training data. Finally, a soft-max layer provides the output probabilities for each class, given the input data. Note that similar CNN-based models are known to perform well for small-scale (*i.e.*, 10-class classification) problems that are analogous to ours. The dimensions of each layer and associated hyper-parameters are specified in Figure 4.5; details about the training process will be provided in Section 7.2.2.

### 4.2.3 Deep Visual Detectors for Hand Gesture Recognition

One operational convenience of hand gesture-based programming is that the robot stays in ‘hover’ mode during the process, and the overall operation is not as time-critical as in the diver following scenario. Therefore, we investigate if we could use deeper and denser models to improve the robustness and accuracy of hand gesture recognition by sacrificing its running time. Specifically, we explore the applicability of the state-of-the-art deep visual models for hand gesture recognition and try to balance the trade-offs between accuracy and running time. We use the same object detection models that are discussed in Section 3.2.3: Faster RCNN with Inception v2 and Single Shot MultiBox Detector (SSD) with MobileNet v2. These are end-to-end models, *i.e.*, perform region selection and hand gesture classification in a single pass. Additionally, they are known to provide accurate and robust performances in noisy visual conditions; their methodological details are provided in Appendix B.1.

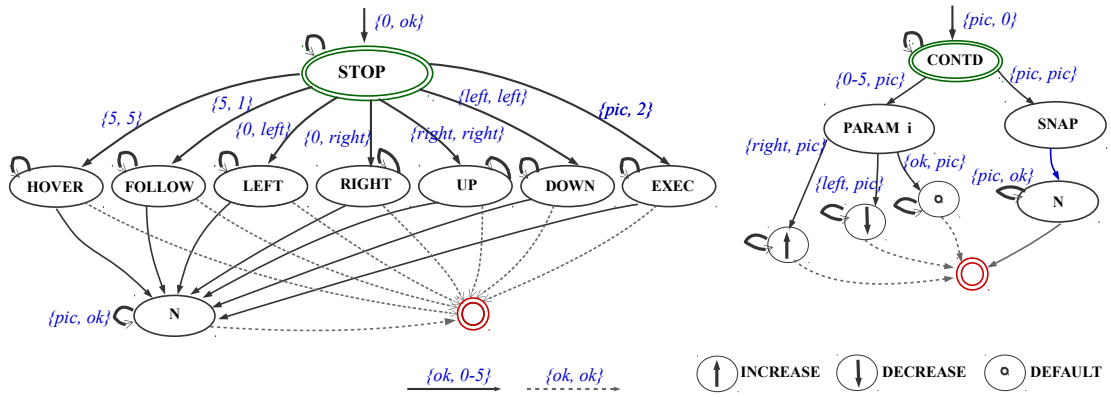


Figure 4.6: An FSM-based deterministic mapping of hand gestures to instructions (based on the rules defined in Figure 4.2).

## 4.3 FSM-based Gesture to Instruction Decoder

An FSM-based deterministic model is used in Robo-Chat-Gest for efficient gesture-to-instruction mapping. As illustrated in Figure 4.6, the transitions between the instruction-tokens are defined as functions of gesture-tokens based on the rules defined in Figure 4.2. Here, we impose an additional constraint that each gesture-token has to be detected for 10 consecutive frames for the transition to be activated. This constraint adds robustness to prevent missed or wrong classification for a particular gesture-token. Additionally, it helps to discard noisy tokens which may be detected when the diver changes from one hand gesture to the next. Furthermore, since the mapping is one-to-one, it is highly unlikely that a wrong instruction will be generated even if the diver mistakenly performs some inaccurate gestures because there are no transition rules other than the correct ones at each state.

## Chapter 5

# Automatic Image Enhancement

The following sections present the network architecture and specification of the proposed GAN-based model for fast underwater image enhancement, which we refer to as FUnIE-GAN. In addition, we provide detailed information about the proposed EUVP dataset.



Figure 5.1: A few instances of naturally distorted and corresponding enhanced underwater images.

### 5.1 FUnIE-GAN Architecture

Given a source domain  $X$  (of distorted images) and desired domain  $Y$  (of enhanced images), our goal is to learn a mapping  $G : X \rightarrow Y$  in order to perform automatic image enhancement. We adopt a conditional GAN-based model where the generator tries to learn this mapping by evolving with an adversarial discriminator through an iterative min-max game. As illustrated in Figure 5.2, we design a generator network by following the principles of U-Net [110]. It is an encoder-decoder network ( $e_1$ - $e_5, d_1$ - $d_5$ ) with connections between the mirrored layers, *i.e.*, between  $(e_1, d_5)$ ,  $(e_2, d_4)$ ,  $(e_3, d_2)$ , and  $(e_4, d_4)$ . Specifically, the outputs of each encoders are concatenated to the respective mirrored decoders. This idea of *skip-connections* in the generator network is shown to be very effective for image-to-image translation and image-quality enhancement problems [46, 53, 9]. In FUnIE-GAN, however, we employ a much simpler model with fewer parameters to achieve fast inference. The input to the network is set to  $256 \times 256 \times 3$  and the encoder ( $e_1$ - $e_5$ ) learns only 256 feature-maps of size  $8 \times 8$ . The decoder ( $d_1$ - $d_5$ ) utilizes these feature-maps and inputs from the skip-connections to learn to generate a  $256 \times 256 \times 3$

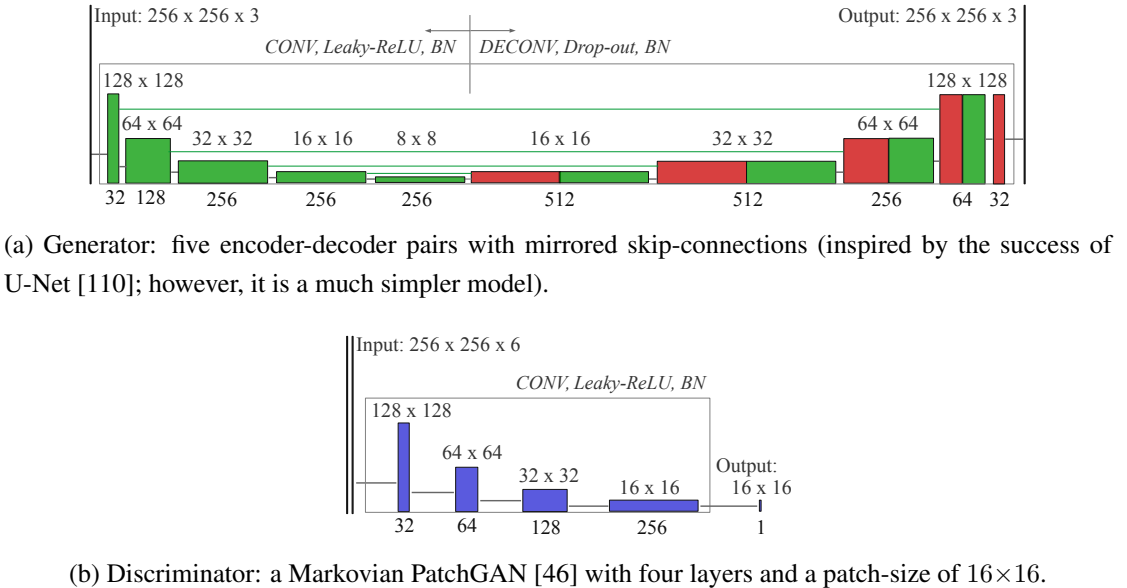


Figure 5.2: Network architecture of the proposed model (FUnIE-GAN).

(enhanced) image as output. The network is fully-convolutional as no fully-connected layers are used. Additionally, 2D convolutions with  $4 \times 4$  filters are applied at each layer, which is then followed by a Leaky-ReLU non-linearity [111] and Batch Normalization (BN) [112]. The feature-map sizes in each layer and other model parameters are annotated in Figure 5.2a.

For the discriminator, we employ a Markovian PatchGAN [46] architecture that assumes the independence of pixels beyond the patch-size, *i.e.*, only discriminates based on the patch-level information. This assumption is important to effectively capture high-frequency features such as local texture and style [52]. Additionally, this configuration is computationally more efficient as it requires fewer parameters compared to discriminating globally at the image level. As shown in Figure 5.2b, four convolutional layers are used to transform a  $256 \times 256 \times 6$  input (real and generated image) to a  $16 \times 16 \times 1$  output that represents the averaged *validity* responses of the discriminator. At each layer,  $3 \times 3$  convolutional filters are used with a stride size of 2; then the non-linearity and BN are applied the same way as the generator. Traditionally, PatchGANs use  $70 \times 70$  patches for  $256 \times 256$  images (*e.g.*, in Pix2Pix [46], DualGAN [52], etc.). However, we use a patch-size of only  $16 \times 16$  in FUnIE-GAN.

## 5.2 Objective Function Formulation

A standard conditional GAN-based model learns a mapping  $G : \{X, Z\} \rightarrow Y$ , where  $X$  ( $Y$ ) represents the source (desired) domain, and  $Z$  denotes random noise. The conditional adversarial loss function [50] is expressed as:

$$\mathcal{L}_{cGAN}(G, D) = \mathbb{E}_{X, Y} [\log D(Y)] + \mathbb{E}_{X, Y} [\log(1 - D(X, G(X, Z)))] \quad (5.1)$$

Here, the generator  $G$  tries to minimize  $\mathcal{L}_{cGAN}$  while the discriminator  $D$  tries to maximize it. In FUnIE-GAN, we associate three additional aspects, *i.e.*, global similarity, image content, and local texture and style information in the objective in order to quantify perceptual image quality.

- **Global similarity:** existing methods have shown that adding an  $L_1$  ( $L_2$ ) loss to the objective function enables  $G$  to learn to sample from a globally similar space in an  $L_1$  ( $L_2$ ) sense [46, 59]. Since the  $L_1$  loss is less prone to introduce blurring, we add the following loss term in the objective:

$$\mathcal{L}_1(G) = \mathbb{E}_{X,Y,Z} [\|Y - G(X, Z)\|_1]. \quad (5.2)$$

- **Image content:** we add a *content loss* term in the objective in order to encourage  $G$  to generate enhanced image that has similar content (*i.e.*, feature representation) as the target (*i.e.*, real) image. Being inspired by [73, 55], we define the image content function  $\Phi(\cdot)$  as the high-level features extracted by the `block5_conv2` layer of a pre-trained VGG-19 network. Then, we formulate the content loss as follows:

$$\mathcal{L}_{con}(G) = \mathbb{E}_{X,Y,Z} [\|\Phi(Y) - \Phi(G(X, Z))\|_2]. \quad (5.3)$$

- **Local texture and style:** as mentioned, Markovian PatchGANs are effective in capturing high-frequency information pertaining to the local texture and style [46]. Hence, we rely on  $D$  to enforce the local texture and style consistency in adversarial fashion.

### 5.2.1 Paired Training

For paired training, we formulate an objective function that guides  $G$  to learn to improve the perceptual image quality so that the generated image is close to the respective ground truth in terms of its global appearance and high-level feature representation. On the other hand,  $D$  will discard a generated image that has locally inconsistent texture and style. Specifically, we use the following objective function for paired training:

$$G^* = \arg \min_G \max_D \mathcal{L}_{cGAN}(G, D) + \lambda_1 \mathcal{L}_1(G) + \lambda_c \mathcal{L}_{con}(G).$$

Here,  $\lambda_1$  and  $\lambda_c$  are scaling factors that are empirically tuned as hyper-parameters.

### 5.2.2 Unpaired Training

For unpaired training, we do not enforce the global similarity and content loss constraints as the pairwise ground truth is not available. Instead, the objective is to learn both the forward mapping  $G_F : \{X, Z\} \rightarrow Y$  and the reconstruction  $G_R : \{Y, Z\} \rightarrow X$  simultaneously by maintaining cycle-consistency. As suggested by Zhu *et al.* [51], we formulate the cycle-consistency loss as follows:

$$\mathcal{L}_{cyc}(G_F, G_R) = \mathbb{E}_{X,Y,Z} [\|X - G_R(G_F(X, Z))\|_1] + \mathbb{E}_{X,Y,Z} [\|Y - G_F(G_R(Y, Z))\|_1]. \quad (5.4)$$

Therefore, our objective for the unpaired training is:

$$G_F^*, G_R^* = \arg \min_{G_F, G_R} \max_{D_Y, D_X} \mathcal{L}_{cGAN}(G_F, D_Y) + \mathcal{L}_{cGAN}(G_R, D_X) + \lambda_{cyc} \mathcal{L}_{cyc}(G_F, G_R).$$

Here,  $D_Y$  ( $D_X$ ) is the discriminator associated with the generator  $G_F$  ( $G_R$ ) and  $\lambda_{cyc}$  is a scaling factor that is empirically tuned as a hyper-parameter.



(a) Paired instances: ground truth images are shown on the top row and their respective distorted pairs are shown on the bottom row.



(b) Unpaired instances: good and poor quality images are shown on the top and bottom row (in no particular order), respectively.

Figure 5.3: A few sample images from the EUVP dataset are shown.

### 5.3 EUVP Dataset

The EUVP dataset contains a large collection of paired and unpaired underwater images of poor and good perceptual quality. Seven different cameras, which include multiple GoPros [113], Aqua AUV’s uEye cameras [114], low-light USB cameras [115], and Trident ROV’s HD camera [116], have been used by the authors to collect images for the dataset. The data was collected during oceanic explorations and human-robot collaborative experiments in different locations under various visibility conditions. Additionally, images extracted from a few publicly available YouTube™ videos are included in the dataset as well.

The paired dataset is prepared using a procedure suggested by Fabbri *et al.* [9]. Specifically, a subset of underwater images contained in the ImageNet dataset [117] is separated and used to train an underwater distortion model based on CycleGAN [51]. Subsequently, a collection of good quality images are distorted using that model in order to generate respective pairs. On the other hand, the unpaired data is labeled (*i.e.*, poor or good quality) based on visual inspection by six individuals. A few sample images from the EUVP dataset are provided in Figure 5.3. It contains roughly 12K paired and 8K unpaired instances. The images are of various resolutions, *e.g.*,  $800 \times 600$ ,  $640 \times 480$ ,  $256 \times 256$ , and  $224 \times 224$ .

## Chapter 6

# Underwater Image Super-Resolution

We now present the design and network architecture of the proposed model for underwater image super-resolution (see Figure 6.1). We also provide details on the objective function formulation and associated training pipeline. We refer to the proposed model as SRDRM when it is trained as a standalone generative model; for adversarial training, we refer to it as SRDRM-GAN. In addition, we provide detailed information about the proposed USE-248 dataset.

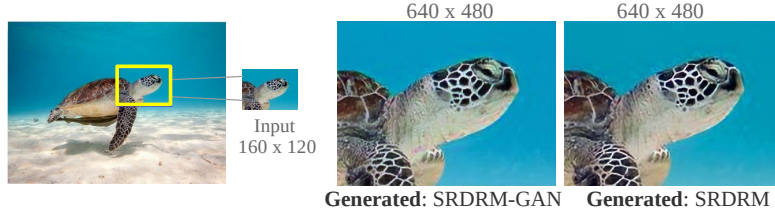


Figure 6.1: Underwater image super-resolution using our proposed models: SRDRM and SRDRM-GAN.

### 6.1 Deep Residual Multiplier (DRM)

The core element of the proposed model is a fully-convolutional deep residual block, designed to learn  $2\times$  interpolation in the RGB image space. We denote this building block as Deep Residual Multiplier (DRM) as it scales the input features' spatial dimensions by a factor of two. As illustrated in Figure 6.2a, DRM consists of a convolutional (conv) layer, followed by 8 repeated residual layers, then another conv layer, and finally a de-convolutional (*i.e.*, deconv) layer for up-scaling. Each of the repeated residual layers (consisting of two conv layers) is designed by following the principles outlined in the EDSR model [77]. Several choices of hyper-parameters, *e.g.*, the number of filters in each layer, the use of ReLU non-linearity [118], and/or Batch Normalization (BN) [112] are annotated in Figure 6.2a. As a whole, DRM is a 10 layer residual network that learns to scale up the spatial dimension of input features by a factor of two. It uses a series of 2D convolutions of size  $3\times 3$  (in repeated residual block) and  $4\times 4$  (in the rest of the network) to learn this spatial interpolation from paired training data.

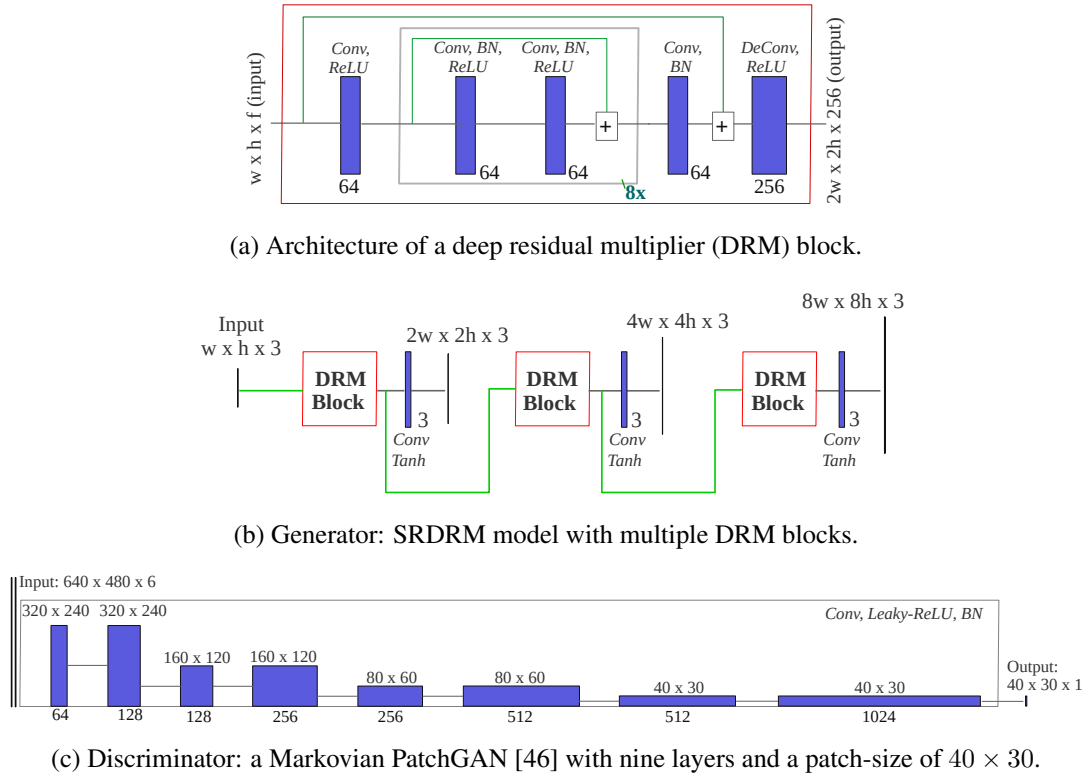


Figure 6.2: Network architecture of the proposed model.

## 6.2 SRDRM and SRDRM-GAN Architecture

As Figure 6.2b demonstrates, the SRDRM makes use of  $n \in \{1, 2, 3\}$  DRM blocks in order to learn to generate  $2^n \times$  HR outputs. An additional `conv` layer with  $\text{tanh}$  non-linearity [119] is added after the final DRM block in order to reshape the output features to the desired shape. Specifically, it generates a  $2^n w \times 2^n h \times 3$  output for an input of size  $w \times h \times 3$ .

For adversarial training, we use the same SRDRM model as the *generator* and employ a Markovian PatchGAN [46]-based model for the *discriminator*. As illustrated by Figure 6.2c, nine `conv` layers are used to transform a  $640 \times 480 \times 6$  input (real and generated image) to a  $40 \times 30 \times 1$  output that represents the averaged *validity* responses of the discriminator. At each layer,  $3 \times 3$  convolutional filters are used with a stride size of 2, followed by a Leaky-ReLU non-linearity [111] and BN. Although traditionally PatchGANs use  $70 \times 70$  patches [46, 52], we use a patch-size of  $40 \times 30$  as our input/output image-shapes are 4:3.

## 6.3 Objective Function Formulation

The SISR problem is defined as learning a function or mapping  $G : \{X\} \rightarrow Y$ , where  $X$  ( $Y$ ) represents the LR (HR) image domain. We propose formulating an objective function that evaluates the following properties of  $G(X)$  compared to  $Y$ :

- **Global similarity and perceptual loss:** existing methods have shown that adding an  $L_1$  ( $L_2$ ) loss to the objective function enables the generator to learn to sample from a globally similar space in an  $L_1$  ( $L_2$ ) sense [46]. In our implementation, we measure the

*global similarity* loss as:

$$\mathcal{L}_2(G) = \mathbb{E}_{X,Y} [\| \|Y - G(X)\| \|_2]. \quad (6.1)$$

Additionally, as suggested in [120], we define a *perceptual loss* function based on the per-channel disparity between  $G(X)$  and  $Y$  as:

$$\mathcal{L}_P(G) = \mathbb{E}_{X,Y} [\| \| (512 + \bar{r})\mathbf{r}^2 + 4\mathbf{g}^2 + (767 - \bar{r})\mathbf{b}^2 \| \|_2]. \quad (6.2)$$

Here,  $\mathbf{r}$ ,  $\mathbf{g}$ , and  $\mathbf{b}$  denote the normalized numeric differences of the red, green, and blue channels between  $G(X)$  and  $Y$ , respectively; whereas  $\bar{r}$  denotes the mean of  $\mathbf{r}$ .

- **Image content loss:** being inspired by the success of state-of-the-art SISR models [84], we also formulate the *content loss* as:

$$\mathcal{L}_C(G) = \mathbb{E}_{X,Y} [\| \| \Phi(Y) - \Phi(G(X)) \| \|_2]. \quad (6.3)$$

Here, the function  $\Phi(\cdot)$  denotes the high-level features extracted by the `block5_conv4` layer of a pre-trained VGG-19 network.

Finally, we formulate the multi-modal objective function for the generator as:

$$\mathcal{L}_G(G) = \lambda_c \mathcal{L}_C(G) + \lambda_p \mathcal{L}_P(G) + \lambda_2 \mathcal{L}_2(G). \quad (6.4)$$

Here,  $\lambda_c$ ,  $\lambda_p$ , and  $\lambda_2$  are scalars that are empirically tuned as hyper-parameters. Therefore, the generator  $G$  needs to solve the following minimization problem:

$$G^* = \arg \min_G \mathcal{L}_G(G). \quad (6.5)$$

On the other hand, adversarial training requires a two-player min-max game [44] between the generator  $G$  and discriminator  $D$ , which is expressed as:

$$\mathcal{L}(G, D) = \mathbb{E}_{X,Y} [\log D(Y)] + \mathbb{E}_{X,Y} [\log(1 - D(X, G(X)))] . \quad (6.6)$$

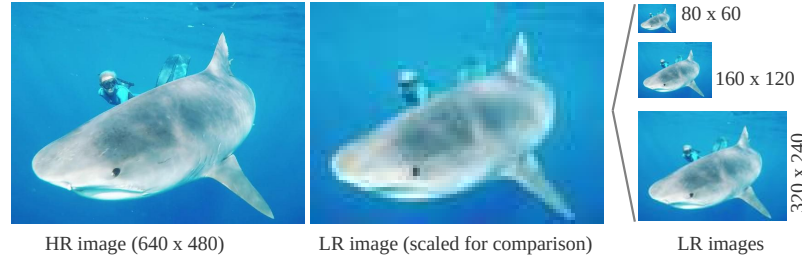
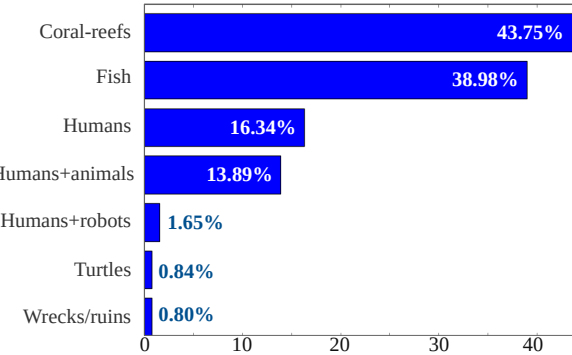
Here, the generator tries to minimize  $\mathcal{L}(G, D)$  while the discriminator tries to maximize it. Therefore, the optimization problem for adversarial training becomes:

$$G^* = \arg \min_G \max_D \mathcal{L}_{GAN}(G, D) + \mathcal{L}_G(G). \quad (6.7)$$

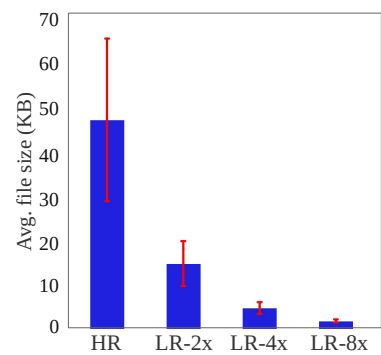
## 6.4 USR-248 Dataset

The USR-248 dataset contains a large collection of HR underwater images and their respective LR pairs. As mentioned earlier, there are three sets of LR images of size  $80 \times 60$ ,  $160 \times 120$ , and  $320 \times 240$ ; whereas, the HR images are of size  $640 \times 480$ . Each set has over 7K RGB images, which are partitioned into *train*, *validation*, and *test* sets of size 6888, 345, and 112, respectively. A few sample images from the dataset are provided in Figure 6.3.

To prepare the dataset, we collected HR underwater images: (i) during various oceanic explorations and field experiments, and (ii) from publicly available Flickr<sup>TM</sup> images and YouTube<sup>TM</sup> videos. The field experiments are performed in a number of different locations over a diverse set of visibility conditions. Multiple GoPros [113], Aqua AUV's uEye cameras [114], low-light USB cameras [115], and Trident ROV's HD camera [116] are used to collect HR images during the experiments. On the other hand, we compiled a large sample of HR underwater

(a) A few instances sampled from the HR set; the HR images are of size  $640 \times 480$ .(b) A particular instance is shown with three LR counterparts of size  $320 \times 240$ ,  $160 \times 120$ , and  $80 \times 60$ .

(c) Modality in the USR-248 dataset based on major objects of interest in the scene.



(d) Avg. files sizes for the HR and LR sets of images.

Figure 6.3: The proposed USR-248 dataset has one HR set and three corresponding LR sets of images; hence, there are three options (*i.e.*,  $2\times$ ,  $4\times$  and  $8\times$ ) for supervised training of SISR models.

images containing natural scenes from Flickr<sup>TM</sup> and YouTube<sup>TM</sup>. We avoided multiple instances of similar scenes and made sure they contain different objects of interest (*e.g.*, coral reefs, fish, divers, wrecks/ruins, etc.) in a variety of backgrounds. Figure 6.3c shows the modality in the data in terms of object categories. Once the HR images are selected and resized to  $640 \times 480$ , three sets of LR images are generated by compressing and then gradually downsizing the images to  $320 \times 240$ ,  $160 \times 120$ , and  $80 \times 60$ ; a comparison of the average file sizes for these image sets are shown in Figure 6.3d. Overall, USR-248 provides large-scale paired data for training  $2\times$ ,  $4\times$ , and  $8\times$  underwater SISR models. It also includes the respective validation and test sets that are used to evaluate our proposed model.

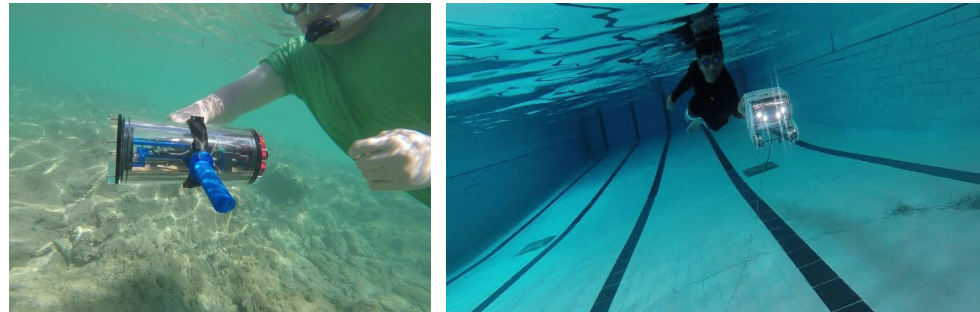
## Chapter 7

# Implementation Details and Evaluation

In the following sections, we provide the implementation details of our proposed methodologies and discuss the relevant operational considerations. We also specify hardware and software platforms used in our implementation and demonstrate several experimental setups. Subsequently, we present the evaluation criteria and discuss the experimental results.



(a) An Aqua 8 UAV [114] named MinneBot. (b) A couple of Trident ROVs [116].



(c) A stereo camera rig build in-house. (d) An OpenROV [121].

Figure 7.1: Underwater robots and embedded rigs that are used in our experiments and data collection.

### 7.1 Systems: Robots and Embedded Platforms

As shown in Figure 7.1, we use several underwater robots and embedded platforms for real-world experiments and data collection. We use an AUV named MinneBot in most of our field experiments. MinneBot is an eighth-generation Aqua robot [114]. It uses six flippers for underwater propulsion with five DOF: surge, heave, pitch, roll, and yaw. For perception, it has three cameras on-board: stereo vision on the front, and monocular vision on the back. Information

passing through these cameras is handled by one of the two on-board computers, namely the vision stack. The other on-board computer, the control stack, is responsible for handling motor commands controlling the robot either teleoperated or autonomously. A recent modification to Aqua led to the addition of the Jetson TX2 [122] embedded computing device. In addition to vision, there is an Inertial Measurement Unit (IMU) and a depth sensor as well; a detailed hardware specification of MinneBot is illustrated in Figure 7.2.

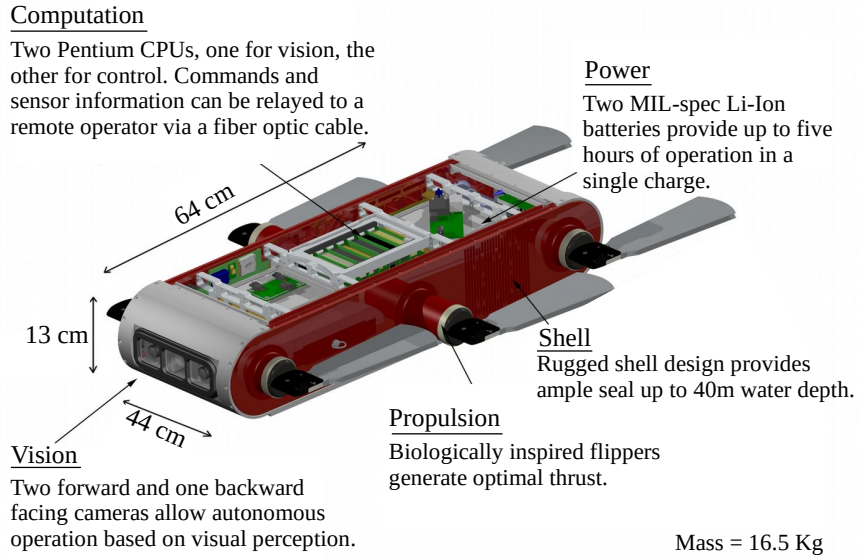


Figure 7.2: The main hardware components of the Aqua robot [114].

We also use a number of ROVs for data collection purposes; specifically, we use one Open-ROV [121] and two Trident ROVs [116]. These ROVs are equipped with on-board HD cameras; they are rugged, easy-to-use, and ideal for capturing data by remote teleoperation. In addition to the ROVs, we use a stereo camera rig (with two low-light USB cameras [115]) and several GoPro cameras [113] for image-based data collection. As demonstrated in Figure 7.1, we use these robots and embedded devices during our field experiments in open-water and closed-water environments, *i.e.*, in oceans and pools, respectively.

## 7.2 Systems: Model Training Pipeline

We discussed several deep visual models for diver detection, hand gesture recognition, image enhancement, and image super-resolution in Chapter 3 through Chapter 6. We now discuss the dataset preparation processes and respective training pipelines.

### 7.2.1 Dataset Preparation

We perform numerous field experiments in pools, lakes, and oceans in order to prepare training data for the deep visual models. Additionally, we collected data from underwater field trials that are performed by different research groups over the years in various locations [8, 1, 12]. This variety of experimental setups is crucial to ensure comprehensiveness of the dataset so that the supervised models can learn the inherent diversity of various application scenarios. In particular,

for diver detection and hand gesture recognition, we made sure that the training data capture the following variability:

- Natural variability: different sources of water, lighting conditions at varying depths, chromatic distortions, etc.
- Artificial variability: data collected using different robots and cameras.
- Human variability: different humans and appearances, choice and variations of wearable such as suits, flippers, goggles, etc.

Moreover, for image enhancement and image super-resolution application, we collect training data: (i) during various oceanic explorations, and (ii) from publicly available Flickr<sup>TM</sup> images and YouTube<sup>TM</sup> videos. We discussed the relevant data collection processes in Section 5.3 (for EUVP dataset) and in Section 6.4 (for USR-248 dataset). The images for EUVP and USR-248 datasets are processed and paired for supervised training. On the other hand, the images of object detection datasets are annotated using the *LabelImg* software [123]. Our colleagues and several other participants contributed to the data collection and annotation processes (acknowledged later in the paper).

### 7.2.2 Implementation and Training

We train all the supervised deep models on a Linux machine with multiple NVIDIA<sup>TM</sup> GTX 1080 GPU cards. TensorFlow [124] and Darknet [107] libraries are used for implementation. Once the training is done, the trained inference model (and parameters) is saved and transferred to the robot CPU for validation and real-time experiments.

Table 7.1: Several hyper-parameter choices adopted in our implementation.

Model	Objective function	Optimizer	Batch-size (epoch)
CNN-based diver detector [1]	Cross-entropy and $L_2$	RMSProp [125]	16 (50)
CNN-based hand gesture recognizer [10]	Cross-entropy	RMSProp [125]	128 (50)
FUnIE-GAN (paired) [12]	Equation 5.2.1	Adam [126]	8 (30)
FUnIE-GAN (unpaired) [12]	Equation 5.2.2	Adam [126]	8 (30)
SRDRM [13]	Equation 6.5	Adam [126]	4 (20)
SRDRM-GAN [13]	Equation 6.7	Adam [126]	4 (20)

In addition, we use the pre-trained models of Faster R-CNN (Inception V2), YOLO v2, Tiny YOLO, and SSD (MobileNet V2) and further train them on diver detection and hand gesture recognition dataset. These state-of-the-art models (see Appendix B.1) are trained with the recommended configurations provided in their APIs; we refer to [107, 36] for the detailed processes.

## 7.3 Experiments and Results

We perform extensive quantitative and qualitative experiments to evaluate the performance of our proposed methodologies. Additionally, we conduct numerous field experiment to validate

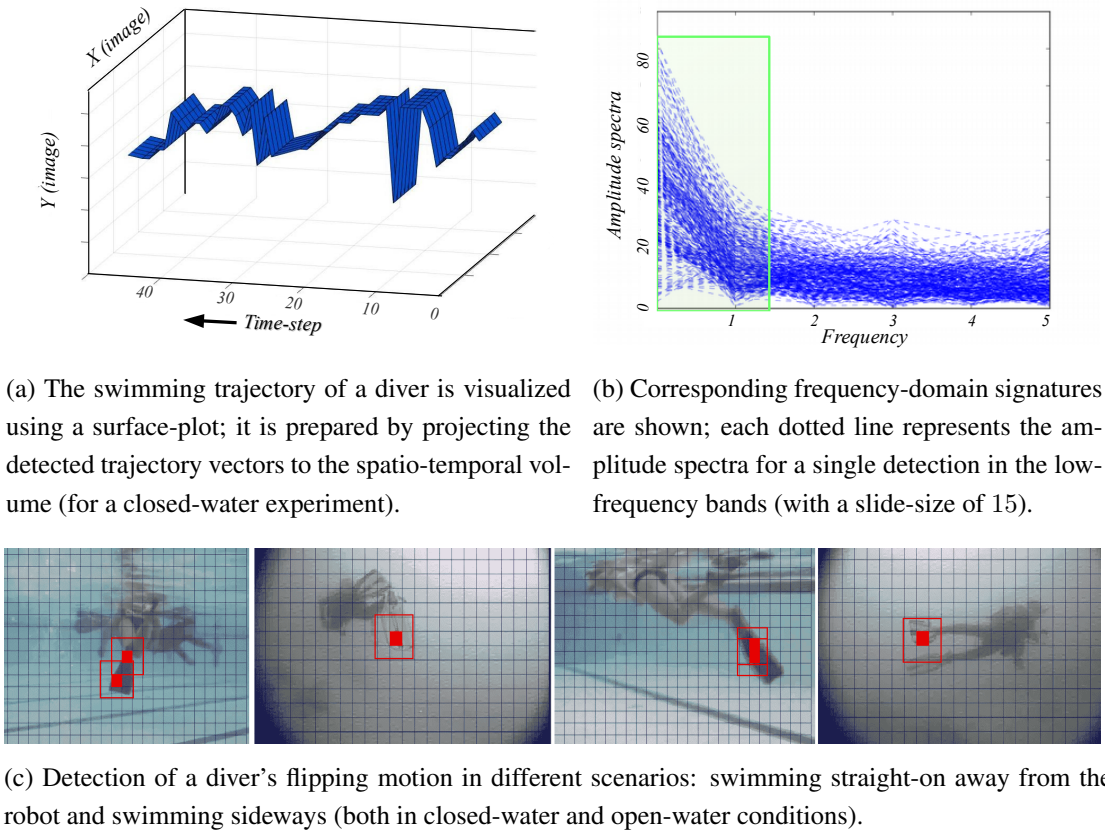


Figure 7.3: Experimental results for autonomous diver following using the proposed MDPM tracker [7].

their applicability in real-world applications. In the following sections, we present and analyze these experimental results and findings.

### 7.3.1 Performance Evaluation: MDPM Tracker

As discussed in Section 3.1, the MDPM tracker has three hyper-parameters: the slide-size ( $T$ ), the size of the sub-windows, and the amplitude threshold ( $\delta$ ) in the frequency-domain. We empirically determine their values through extensive simulations on video footage of diver-following. We found that  $T=15$  and a sub-window size of  $30\times 30$  work well in practice; also, we set the frequency threshold  $\delta=75$ . Once the bootstrapping is done with the first  $T$  frames, mixed-domain detection is performed at every  $T$  frames onward in a sliding-window fashion. At each detection, the tracker estimates the potential trajectory vectors that represent a set of motion directions in spatio-temporal volume. If a potential motion direction produces amplitude-spectra more than  $\delta$ , it is reported as a positive detection at that time-step. Subsequently, the diver's flippers are located in the image space, and a bounding box is generated.

Figure 7.3 demonstrates how MDPM tracker detects a diver using spatial- and frequency-domain cues. It keeps track of the diver's motion direction through a sequence of  $30\times 30\times 15$  sub-windows in the spatio-temporal volume. The corresponding surface through the image space over time mimics the actual motion direction of the diver, which indicates the effectiveness of the algorithm. Table 7.2 provides the performance of MDPM tracker in terms of positive detections, missed detections, and wrong detections for different experimental cases. It achieves

Table 7.2: Detection performance of MDPM tracker in different swimming conditions.

Cases	Closed Water		Open Water	
	Straight-on	Sideways	Straight-on	Sideways
Correct detection (True positives on the target image sub-windows, true negatives on the rest)	647 (91.7%)	463 (87.3%)	294 (85.2%)	240 (84.2%)
Missed detection (False negatives on the target image sub-windows)	46 (6.5%)	57 (10.8%)	38 (11%)	43 (15%)
Wrong detection (False positives on the non-target image sub-windows)	12 (1.8%)	10 (1.9%)	13 (3.8%)	2 (0.8%)

a positive detection accuracy of 84.2-91.7%, which suggests that it provides 8-9 positive detections of a diver per second (considering a frame-rate of 10 fps). We have found this detection rate quite sufficient for successfully following a diver in practice.

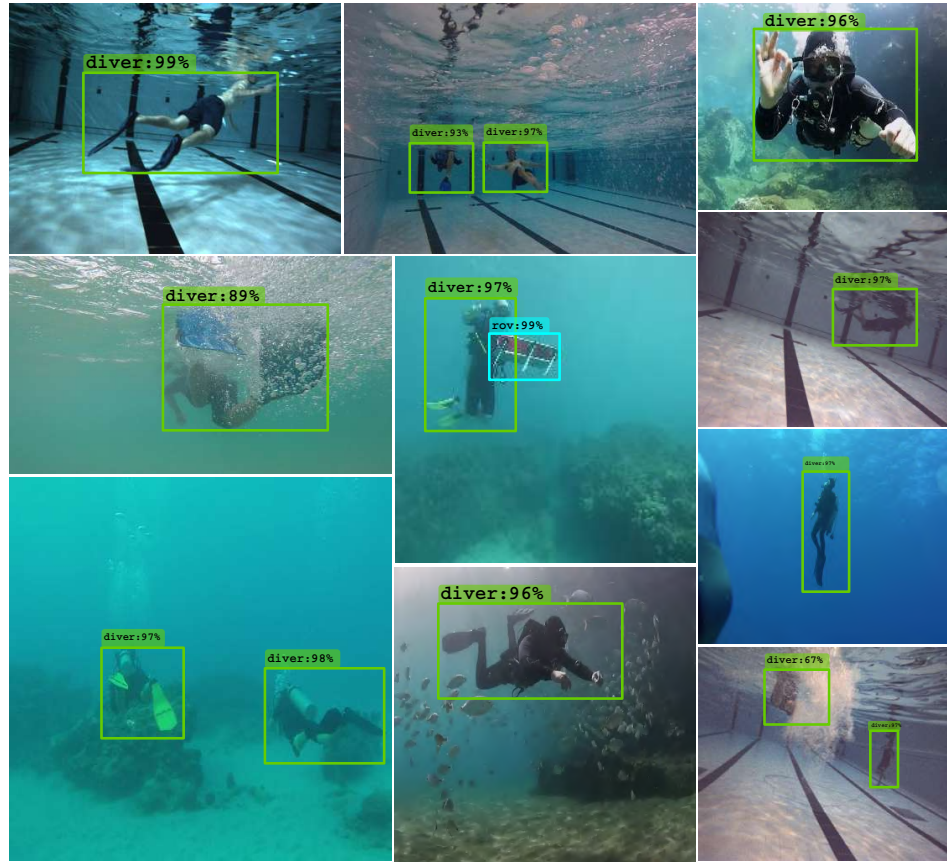


Figure 7.4: Snapshots of a set of diverse first-person views of the robot from different diver-following scenarios. Notice the variation in appearances of the divers and possible noise or disturbances in the scene over different scenarios. The rectangles and text overlaid on the images are the outputs generated by our CNN-based model at test time.

### 7.3.2 Performance Evaluation: Deep Diver Detection

Next, we analyze the detection performance of the deep visual models for diver detection. The test dataset contain 2.2K images that are chosen from separate field experiments, *i.e.*, they are excluded from the training dataset. We use the following two standard performance metrics:

- **mAP (mean Average Precision):** it is the average of the maximum precisions at different recall values. The precision and recall are defined as  $precision = \frac{TP}{TP+FP}$  and  $recall = \frac{TP}{TP+FN}$ ; here, the terms TP, FP, and FN are short forms of True Positive, False Positive, and False Negative, respectively.
- **IoU (Intersection over Union):** it is a measure of how well a model predicts the locations of the objects. It is calculated using the area of overlapping regions of the predicted and ground truth bounding boxes, defined as  $IoU = \frac{Area\ of\ overlap}{Area\ of\ union}$ .

As their definitions suggest, mAP measures the detection accuracy, and IoU measures the object localization performance. We also evaluate and compare the running times of the models based on FPS (Frames Per Second), the average number of frames that a model can process in one second. We measure the run-times on three different devices: NVIDIA™ GTX 1080 GPU, Embedded GPU (NVIDIA™ Jetson TX2), and Robot CPU (Intel™ i3-6100U).

Table 7.3: Performance comparison for the diver detection models based on standard metrics.

Models	mAP (%)	IoU (%)	FPS		
			GTX 1080	Jetson TX2	Robot CPU
Faster R-CNN (Inception V2)	71.1	78.3	17.3	2.1	0.52
YOLO V2	57.84	62.42	73.3	6.2	0.11
Tiny YOLO	52.33	59.94	220	20	5.5
SSD (MobileNet V2)	61.25	69.8	92	9.85	3.8
Proposed CNN-based Model	53.75	67.4	263.5	17.35	6.85

The performances of the diver detection models based on mAP, IoU, and FPS are illustrated in Table 7.3. The Faster R-CNN (Inception V2) model achieves much better detection performances compared to the other models although it is slowest in terms of run-time. On the other hand, YOLO V2, SSD (MobileNet V2), and the proposed CNN-based model provide comparable detection performance. Although Tiny YOLO provides fast running time, its detection performance is not as good as the other models. As the results demonstrate, the proposed CNN-based model runs at a rate of 6.85 FPS on the robot CPU and 17.35 FPS on the embedded GPU, which validate its applicability for real-time diver-following applications. This fast run-time comes at a cost of losing approximately 18% mAP and 11% IoU compared to the Faster R-CNN (Inception V2) model. Nevertheless, in our real-world experiments (Figure 7.4), we have found these detection rates to be sufficient for achieving reasonable tracking performance.

### 7.3.3 Field Experiments: Autonomous Diver Following

As seen in Figure 7.5, we perform several real-world experiments both in closed-water and in open-water conditions. During the experiments, a diver swims in front of the robot in arbitrary directions. The task of the robot is to visually detect the diver using its camera feed and follow behind them with a smooth motion. We do this by implementing a visual servo controller [97] that uses the bounding box generated by the diver detector to regulate robot motion commands in order to follow the diver.



Figure 7.5: The detection of divers and other objects (e.g., other robots) by deep visual models. A video demonstration can be seen here: <https://youtu.be/9xukzT8dqzQ>.

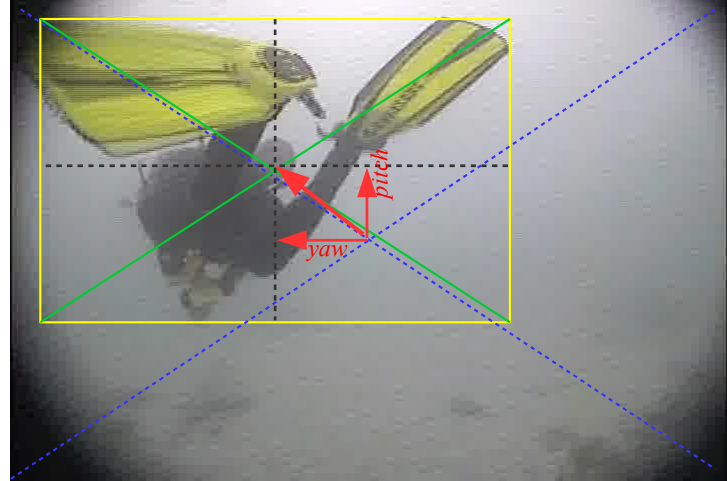


Figure 7.6: Illustration of how the yaw and pitch commands are generated based on the horizontal and vertical displacements of the center of the detected bounding box.

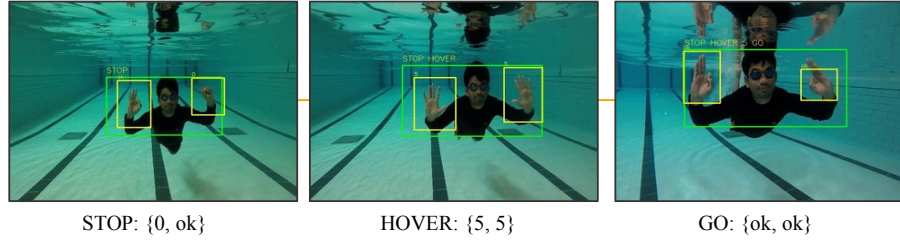
As mentioned, we use the MinneBot AUV for diver following experiments, which has five DOF of control: three angular (yaw, pitch, and roll) and two linear (surge and heave) controls. In our implementation, we adopt a tracking-by-detection method where the controller tries to bring the observed bounding box of the target diver to the center of the camera image. The distance of the diver is approximated by the size of the bounding box and forward velocity rates are generated accordingly. Additionally, the yaw and pitch commands are normalized based on the horizontal and vertical displacements of the observed bounding box center from the image center (Figure 7.6); these navigation commands are then regulated by separate PID controllers. On the other hand, the roll stabilization and hovering are handled by the robot’s autopilot module [127].

Since we adopt a bounding box reactive servo control, correct detection of the diver is essential to ensure good tracking performance. During the field experiments, we have found 6-7 positive detection per second on an average, which is sufficient for successfully following a diver in real-time [8]. Moreover, the proposed model is considerably robust to occlusion and noise, in addition to being invariant to divers’ appearance and wearable. Lastly, our training data include a large collection of gray-scale and color distorted underwater images; hence the proposed models are considerably robust to noise and color distortions.

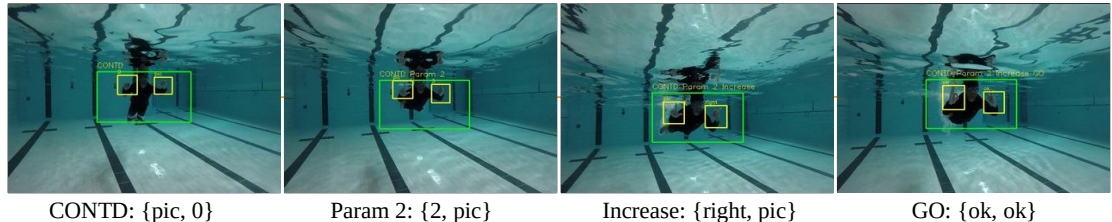
### 7.3.4 Performance Evaluation: Robo-Chat-Gest

The performance of our proposed human-robot communication framework named Robo-Chat-Gest mostly depends on the accuracy and correctness of the hand gesture recognition module. This is because the FSM-based instruction decoder is deterministic and has a one-to-one gesture-to-instruction mapping. As mentioned in Section 4.3, the robustness of the mapping is ensured by the following transition rules:

- State transitions are activated only if the corresponding gesture-tokens are detected for 10 consecutive frames. Therefore, an incorrect recognition has to happen 10 consecutive frames to generate an incorrect instruction-token, which is highly unlikely.
- There are no transition rules (to other states) for incorrect gesture-tokens. Consequently, incorrect instruction-tokens are not going to generate a complete wrong instruction.



(a) Instructing the robot to stop executing the current program and hover.



(b) Instructing the robot to continue its program but increase the value of parameter 2 (by one step).

Figure 7.7: Demonstrations of hand gesture-based robot programming using Robo-Chat-Gest. The yellow bounding boxes represent the hand gestures detected by our CNN-based model; note that the {left, right} hand gestures are ordered as the person's left and right hands.

Table 7.4: Performance of our framework on test data using different hand gesture recognizers.

Hand Gesture Recognizer	Total # of Instructions (Gestures)	Correct Detection	Accuracy (%)	FPS (robot CPU)
Our Model	30 (162)	24 (128)	80 (78)	17-18
Faster RCNN (Inception V2)	30 (162)	29 (152)	96.6 (93.8)	2-3
SSD (MobileNet V2)	30 (162)	27 (144)	90 (88.8)	6-7

Figure 7.7 demonstrates how divers can communicate instructions to the robot using a sequence of hand gestures in Robo-Chat-Gest. We test our framework extensively using the three different hand gesture recognizers. The test dataset contains a diverse set of 30 instructions that

involve a total of 162 hand gestures. Table 7.4 illustrates the performance of Robo-Chat-Gest for different choices of hand gesture recognizers; it shows that our CNN-based model is significantly faster than the state-of-the-art models. However, the detection accuracy is not very good; it correctly detected 24 out of 30 instructions with a hand gesture recognition accuracy of 78%. We inspected the failed cases and found the following issues:

- In some cases, the diver’s hand(s) appeared in front of his face or only partially appeared in the field-of-view. In these cases, not all of the hand(s) appeared in the selected region which caused the gesture recognizer to detect ‘ok’s as ‘0’s, or ‘pic’s as ‘1’s, etc.
- Surface reflection and air bubbles often cause problems for the region selector. Although surface reflection is not common in deep water, suspended particles and limited visibility are additional challenges in deep water scenarios.



(a) Detections using Faster RCNN (inception v2).



(b) Detections using SSD (MobileNet v2).

Figure 7.8: A few snapshots of robust hand gesture recognition by the state-of-the-art object detectors used in our framework.

The state-of-the-art deep visual detectors perform much better in such challenging conditions. As demonstrated in Table 7.4, Faster RCNN correctly detected 29 out of 30 instructions with a hand gesture recognition accuracy of 93.8%. On the other hand, SSD correctly detected 27 out of 30 instructions with an 88.8% hand gesture recognition accuracy. Although these detectors are slower than our model, they are significantly more robust and accurate. We have used both Faster RCNN and SSD in Robo-Chat-Gest for real-time experiments (Figure 7.8); their slow running times do not affect the overall operation significantly. Detecting hand gestures is not as time-critical as tracking a diver in real-time; therefore, even 2-3 detections per second is good enough for practical implementations. Currently, we use SSD (MobileNet V2) as the hand gesture recognizer to balance the trade-offs between performance and running time.

### 7.3.5 Field Experiments: Robo-Chat-Gest

The qualitative and quantitative results illustrated so far are based on numerous field experiments in pools and oceans. We now demonstrate the practical use-cases of Robo-Chat-Gest

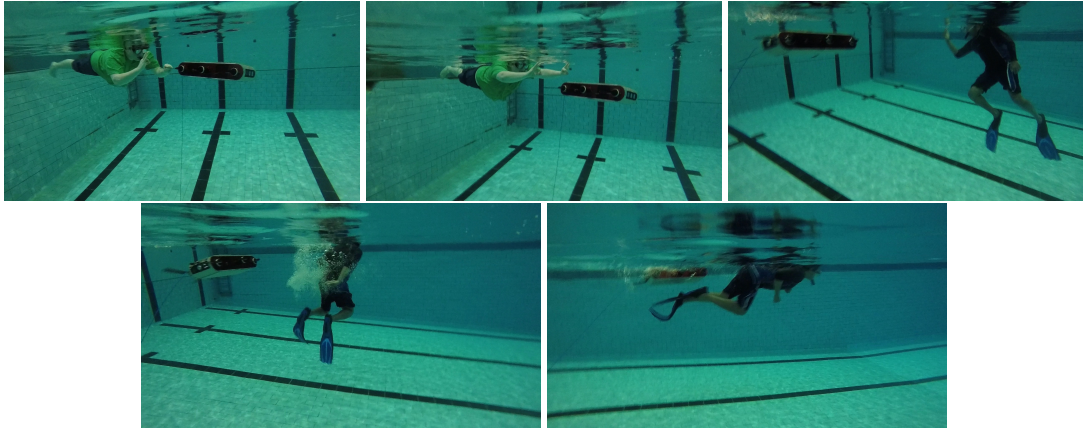


Figure 7.9: Image sequence demonstrating gesture-based communication to enable person following underwater (left-to-right, top-to-bottom). An individual is using hand gestures to instruct the robot to switch to diver-following mode from its current (hovering) mode. The robot detects these hand gestures through its back camera, decodes the instruction, and executes the diver-following program. Subsequently, it detects the person to follow using its front camera and starts following him. A short video of the experiment can be found at: [https://youtu.be/An4IdMV\\_VtU](https://youtu.be/An4IdMV_VtU).

in human-robot collaborative applications. Specifically, we perform experiments where Robo-Chat-Gest is used to instruct a robot to perform various atomic instructions such as calibrating the flippers, swimming forward, hovering, etc. Additionally, we tested the task switching operations, *i.e.*, instructing the robot to stop its current task and execute another specified task. As an operational constraint, these tasks are specified to the robot beforehand and the hand gesture-based communication framework is configured such that these modules are invoked when the corresponding instructions are detected. Demonstration of a sample experiment is illustrated in Figure 7.9, in which a person communicates the following instruction to the MinneBot AUV:

STOP current program and EXECUTE the DIVER-FOLLOWING module.

Since MinneBot has its ‘menu selection screen’ on the rear end, its back camera is used for human-robot communication purposes. First, the person performs a correct sequence of hand gestures in front of the back camera. Once the hand gestures are detected, the corresponding instruction is generated and the diver-following module is invoked. Then, it detects the diver in front (using its front camera) and starts following him. It is important to note that the overall operation is independent of this setup; the same diver can perform hand gestures and start leading the robot using front cameras only. However, we have found the current setup operationally convenient for our experiments.

### 7.3.6 User Study: Human-Robot Communication

We also perform simulation experiments on controlling an Aqua robot based on the instructions generated from sequences of hand gestures performed by participants. The gesture sequences are captured through a web-cam and the simulation is performed in Gazebo on the ROS Kinetic platform. As illustrated in Figure 7.10, gesture-tokens are successfully decoded to control the robot. Although a noise-free simulation environment does not pose most challenges that are common in the real world, it helps to set benchmarks for expected performance bounds and is

useful in human interaction studies. We conduct such a study where the participants are introduced to Robo-Chat-Gest, the fiducial-based Robo-Chat framework [32], and the Robo-Chat-Motion framework [33] where a set of discrete motions from a pair of fiducials are interpreted as gesture-tokens. AprilTags [30] are used for the Robo-Chat trials to deliver commands. A total of ten individuals participated in the study, who were grouped according to their familiarity with robot programming paradigms in the following manner:

- Beginner (2 participants): unfamiliar with gesture/fiducial based robot programming.
- Medium (7 participants): familiar with gesture/fiducial based robot programming.
- Expert (1 participants): familiar and practicing these frameworks for some time.

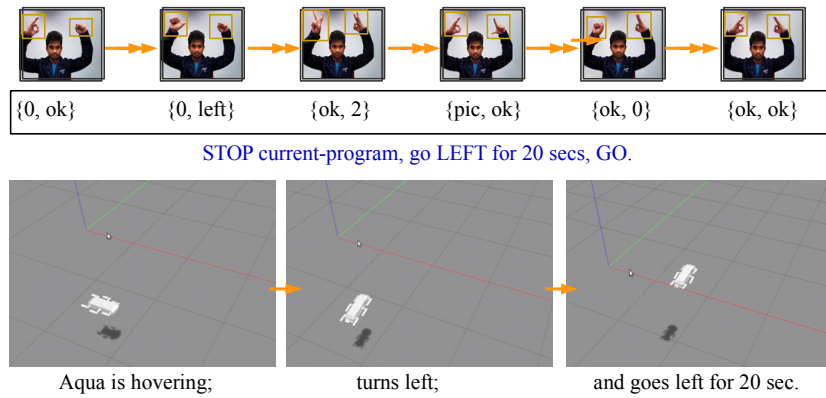


Figure 7.10: Controlling an Aqua robot using instructions generated from a sequence of hand gestures performed by a person; the simulation is performed in Gazebo on the ROS-kinetic platform.

The study is similar to the one conducted by Xu *et al.* [33]. In the first set of trials, participants are asked to perform sequences of gestures to generate the following instructions in all three interaction paradigms:

1. STOP current-program, HOVER for 50 seconds, GO.
2. CONTD current-program, take SNAPSHOTS for 20 seconds, GO.
3. CONTD current-program, Update Parameter 3 to DECREASE, GO.
4. STOP current-program, EXECUTE Program 1, GO.

In the second set of trials, the participants are asked to program the robot for the following two relatively more complex scenarios:

- a. The robot has to stop its current task and execute program 2 while taking snapshots, and
- b. The robot has to take pictures for 50 seconds and then start following the diver.

For all the experiments mentioned above, participants perform gestures with hands, AprilTags, and discrete motions with AprilTags. Correctness and the amount of time taken were recorded in each case. Figure 7.11 shows the comparison of the average time taken to perform gestures for generating different types of instructions. Participants quickly adopted the

Table 7.5: Average number of mistakes using [hand gesture, Robochat, AprilTags with motion] for different users before correctly generating the instruction.

Instruction Type	Total # of Instructions (Gestures)	Beginner User	Medium User
STOP	2 (10)	[2, 1, 3]	[1, 0, 1]
CONTD	2 (10)	[0, 0, 1]	[0, 0, 0]
Complex	2 (16)	[2, 3, 7]	[2, 2, 3]

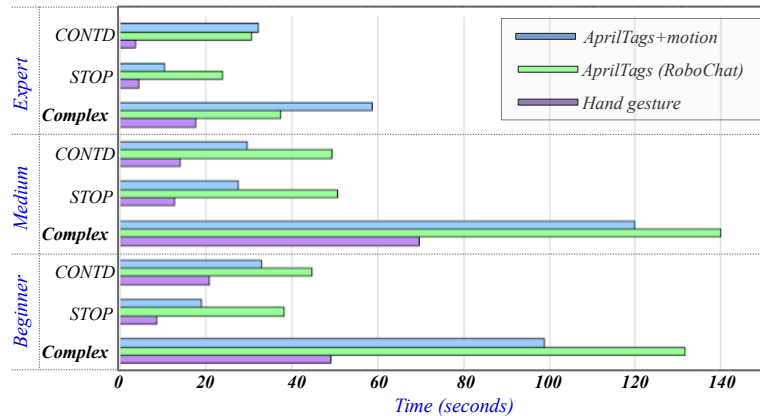
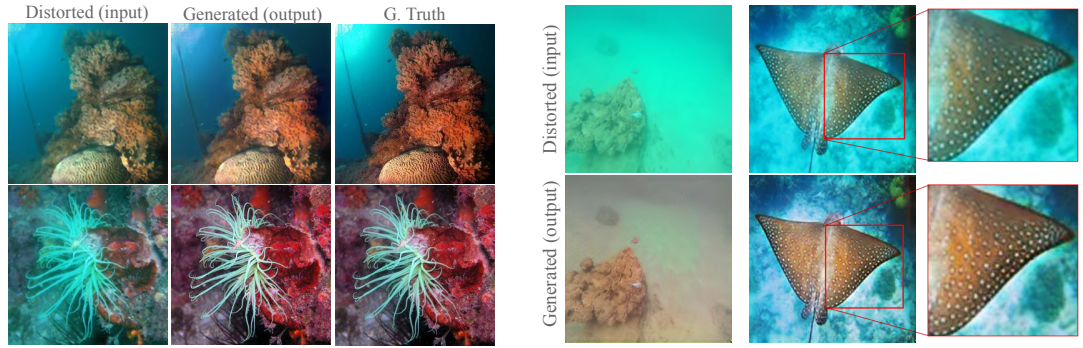


Figure 7.11: Comparison of average time taken to perform gestures to successfully generate different programs (STOP: instructions 1 and 4, CONTD: instructions 2 and 3, Complex: scenarios *a* and *b*).

hand gestures-to-instruction mapping and took significantly less time to finish programming compared to the other two alternatives. Specifically, participants found it inconvenient and time-consuming to search through all the tags for each instruction token. On the other hand, although performing a set of discrete motions with only two AprilTags saves time, it was less intuitive to the participants. As a result, it still took a long time to formulate the correct gestures for complex instructions, as evident from the results. One interesting result is that the *beginner* users took less time to complete the instructions compared to *medium* users. This is probably because unlike the beginner users, medium users were trying to intuitively interpret and learn the syntax while performing the gestures. However, as illustrated by Table 7.5, beginner users made more mistakes on an average before completing an instruction successfully. The expert user performed all tasks on the first try, hence only comparison for beginner and medium users is presented. Since there are no significant differences in the number of mistakes for any type of user, we conclude that simplicity, efficiency, and intuitiveness are the major advantages of Robo-Chat-Gest over the existing methods.

### 7.3.7 Qualitative Evaluation: FUnIE-GAN

We first qualitatively analyze the enhanced color and sharpness of the FUnIE-GAN-generated images compared to their respective ground truths. As Fig. 7.12a shows, the true color and sharpness is mostly recovered in the enhanced images. Moreover, as shown in Fig. 7.12b, we observe that the greenish hue in underwater images are rectified and the global contrast is enhanced. These are primary characteristics of an effective underwater image enhancer. Next, we conduct a qualitative comparison of perceptual image enhancement by FUnIE-GAN with a number of state-of-the-art models; we consider (i) underwater GAN with gradient penalty



(a) True color and sharpness is restored in the enhanced image.  
 (b) The greenish hue is rectified and global contrast is enhanced.

Figure 7.12: Improved image attributes by FUnIE-GAN in terms of color, sharpness, and contrast.

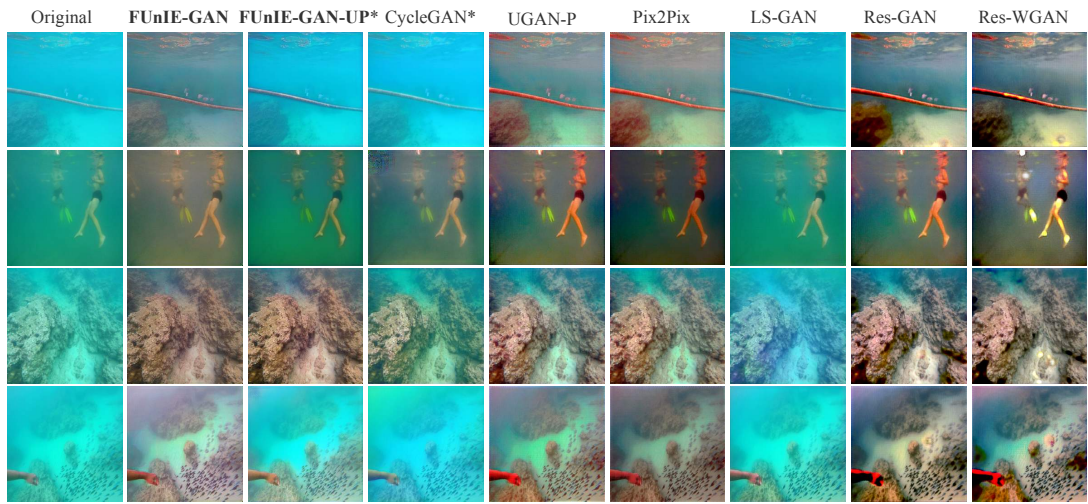


Figure 7.13: Qualitative performance comparison of FUnIE-GAN and FUnIE-GAN-UP with CycleGAN [51], UGAN-P [9], Pix2Pix [46], least-squared GAN (LS-GAN [49]), residual GAN (Res-GAN [128]), and residual Wasserstein GAN (Res-WGAN [47]). The super-scripted asterisk (\*) represents unpaired training.

(UGAN-P [9]), (ii) Pix2Pix [46], (iii) least-squared GAN (LS-GAN [49]), (iv) GAN with residual blocks [128] in the generator (Res-GAN), and (v) Wasserstein GAN [47] with residual blocks in the generator (Res-WGAN). These models are implemented with 8 encoder-decoder pairs (or 16 residual blocks) in the generator network and 5 convolutional layers in the discriminator. They are trained on the paired EUVP dataset using the same setup as the FUnIE-GAN. In addition, we consider CycleGAN [51] as a baseline for comparing the performance of FUnIE-GAN with unpaired training (*i.e.*, FUnIE-GAN-UP). Their perceptual image enhancements are compared on a common test set; we present a few sample comparisons in Fig. 7.13.

As demonstrated in Fig. 7.13, Res-GAN and Res-WGAN suffer from over-saturation, while LS-GAN generally fails to rectify the greenish hue in images. UGAN-P and Pix2Pix perform reasonably well and their enhanced images are comparable to that of FUnIE-GAN; however, UGAN-P often over-saturates bright objects in the scene while Pix2Pix fails to enhance global brightness in some cases. On the other hand, we observe that achieving color consistency and

hue rectification are relatively more challenging through unpaired learning. This is mostly because of the lack of reference color or texture information in the loss function. Nevertheless, FUnIE-GAN-UP still outperforms CycleGAN in general. Overall, FUnIE-GAN performs as well and often better compared to these models for underwater image enhancement despite having a much simpler network architecture.

Table 7.6: Average PSNR and SSIM values on 1K paired test images of EUVP dataset.

Model	$PSNR(G(\mathbf{x}), \mathbf{y})$ Input: $17.27 \pm 2.88$	$SSIM(G(\mathbf{x}), \mathbf{y})$ Input: $0.62 \pm 0.075$
Res-WGAN	$16.46 \pm 1.80$	$0.5762 \pm 0.014$
Res-GAN	$14.75 \pm 2.22$	$0.4685 \pm 0.122$
LS-GAN	$17.83 \pm 2.88$	$0.6725 \pm 0.062$
Pix2Pix	$20.27 \pm 2.66$	$0.7081 \pm 0.069$
UGAN-P	$19.59 \pm 2.54$	$0.6685 \pm 0.075$
CycleGAN	$17.14 \pm 2.65$	$0.6400 \pm 0.080$
<b>FUnIE-GAN-UP</b>	$21.36 \pm 2.17$	$0.8164 \pm 0.046$
<b>FUnIE-GAN</b>	$21.92 \pm 1.07$	$0.8876 \pm 0.068$

Table 7.7: Average UIQM values on 1K paired and 2K unpaired test images of EUVP dataset.

Model	<b>Paired data</b>	<b>Unpaired data</b>
	Input: $2.20 \pm 0.69$ G. Truth: $2.91 \pm 0.65$	Input: $2.29 \pm 0.62$ G. Truth: N/A
Res-WGAN	$2.55 \pm 0.64$	$2.46 \pm 0.67$
Res-GAN	$2.62 \pm 0.89$	$2.28 \pm 0.34$
LS-GAN	$2.37 \pm 0.78$	$2.59 \pm 0.52$
Pix2Pix	$2.65 \pm 0.55$	$2.76 \pm 0.39$
UGAN-P	$2.72 \pm 0.75$	$2.77 \pm 0.34$
CycleGAN	$2.44 \pm 0.71$	$2.62 \pm 0.67$
<b>FUnIE-GAN-UP</b>	$2.56 \pm 0.63$	$2.81 \pm 0.65$
<b>FUnIE-GAN</b>	$2.78 \pm 0.43$	$2.98 \pm 0.51$

### 7.3.8 Quantitative Evaluation: FUnIE-GAN

We consider two standard metrics [129, 12] named Peak Signal-to-Noise Ratio (PSNR) and Structural Similarity (SSIM) in order to quantitatively compare FUnIE-GAN-enhanced images with their respective ground truth. We conduct a similar analysis for Underwater Image Quality Measure (UIQM) [130, 131], which quantifies underwater image colorfulness, sharpness, and contrast. Their definitions and relevant details are provided in Appendix D.1.

We use a set of 1K paired test images ( $\mathbf{x} \in X, \mathbf{y} \in Y$ ) in our evaluation. At first, we use FUnIE-GAN to generate enhanced images  $G(\mathbf{x})$  for each  $\mathbf{x}$  and then compute  $PSNR(G(\mathbf{x}), \mathbf{y})$  and  $SSIM(G(\mathbf{x}), \mathbf{y})$  using Eq. D.1 and D.2, respectively. In Table 7.6, we provide the averaged PSNR and SSIM values over 1K test images for FUnIE-GAN and compare the results with the same models used in the qualitative evaluation. The results indicate that FUnIE-GAN performs best on both PSNR and SSIM metrics. Moreover, the results in Table 7.7 indicates that although FUnIE-GAN-UP performs better than CycleGAN, its UIQM values on the the

Table 7.8: Run-time of FUnIE-GAN and UGAN-P on different hardware (in milliseconds).

Model	Titan Xp	Jetson TX2	Robot CPU
<b>FUnIE-GAN</b>	11.10 (90 fps)	65.81 (15.2 fps)	126 (7.9 fps)
UGAN-P	19.23 (52 fps)	370.3 (2.7 fps)	—

paired dataset are relatively poor. Interestingly, the models trained on paired data, particularly FUnIE-GAN, UGAN-P, and Pix2Pix, produce better results. We postulate that the global similarity loss in FUnIE-GAN and Pix2Pix, or the gradient-penalty term in UGAN-P contribute to this enhancement, as they all add an  $L_1$  term in the adversarial objective.

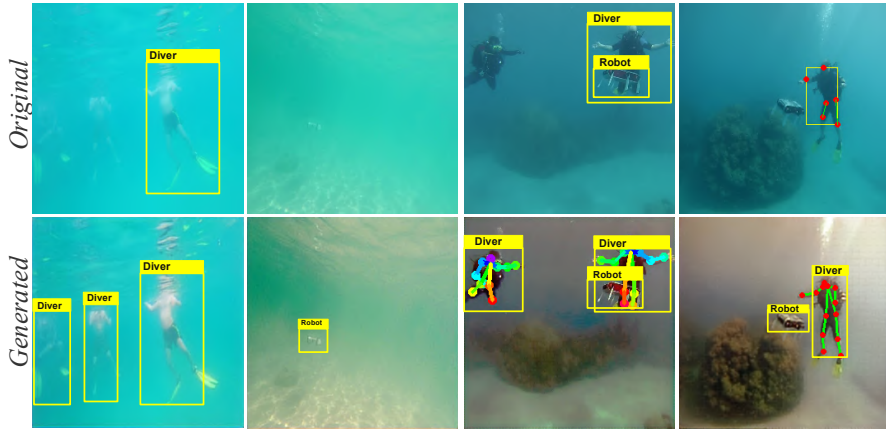


Figure 7.14: Improved performance for object detection and human pose estimation on FUnIE-GAN-enhanced images. A detailed demonstration can be found at: <https://youtu.be/1ewcXQ-jgB4>.

Our motivation for designing an architecturally simple model was to achieve a fast inference-time so that it can be used in real-time applications. FUnIE-GAN operates at a rate of 15.2 fps on a single-board computer (NVIDIA<sup>TM</sup> Jetson TX2), 90 fps on a graphics card (NVIDIA<sup>TM</sup> Titan Xp), and 7.9 fps on a CPU (Intel Core<sup>TM</sup> i3-6100U) used in a robotic platform. As demonstrated in Table 7.8, these rates are significantly faster than its closest competitor UGAN-P (based on the performance metrics discussed so far). Moreover, FUnIE-GAN’s memory requirement is 17 MB, which is 5 times less than UGAN-P. As illustrated in Fig. 7.14, we conduct further experiments in order to quantitatively interpret the effectiveness of FUnIE-GAN-enhanced images for underwater visual perception. Specifically, we analyze the performance of standard deep visual models for underwater object detection [1] and human pose estimation [132] over a variety of test cases. On an average, we observe 11-14% improvement on diver detection, 7-12% improvement on robot detection, and 22-28% improvement on human pose-based 2D key-point detection in enhanced images compared to the original ones. It is to be noted that the numbers vary depending on the image qualities of a particular test set. However, these results validate the feasibility of using FUnIE-GAN for improving real-time perception of visually-guided underwater robots.

### 7.3.9 User Study: Automatic Image Enhancement

We also conduct a user study to add human preferences to our qualitative performance analysis. As Fig. 7.15 illustrates, the participants are shown different sets of 9 images (one for each

Table 7.9: Rank- $n$  accuracy ( $n = 1, 2, 3$ ) for the top four models based on 312 responses provided by 78 individuals during the user study.

Model	Rank-1 (%)	Rank-2 (%)	Rank-3 (%)
<b>FUnIE-GAN</b>	24.50	68.50	88.60
<b>FUnIE-GAN-UP</b>	18.67	48.25	76.18
UGAN-P	21.25	65.75	80.50
Pix2Pix	11.88	45.15	72.45

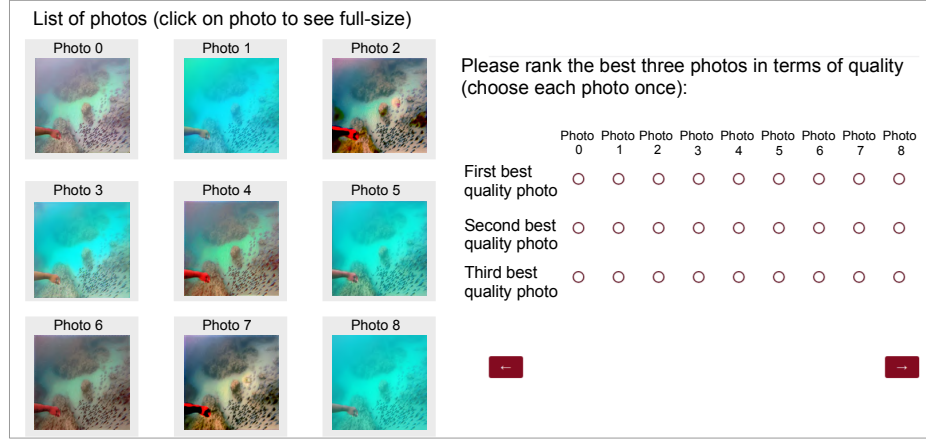


Figure 7.15: A snapshot of the user interface used in our study.

category considered in Fig. 7.13) and asked to rank top 3 best quality images. A total of 78 individuals participated in the study and a total of 312 responses are recorded. Table 7.9 compares the average rank-1, rank-2, and rank-3 accuracy of the top 4 (out of 9) categories. The average rank-3 accuracy of the original images is recorded to be 6.67, which suggests that the users clearly preferred enhanced images over the original ones. Moreover, the results indicate that the users prefer the images enhanced by FUnIE-GAN, UGAN-P, and Pix2Pix compared to the other models; these statistics are consistent with our qualitative and quantitative analysis.

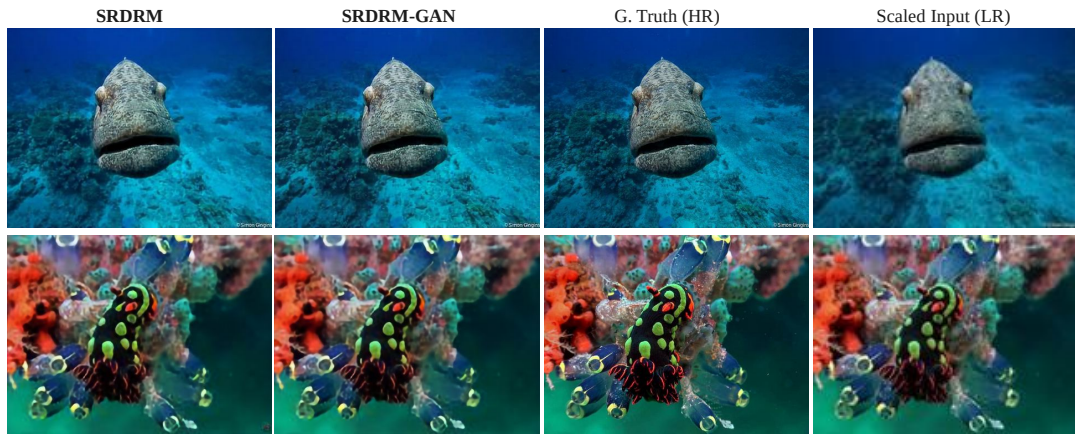


Figure 7.16: Color consistency and sharpness of the generated 4 $\times$  images compared to the ground truth.

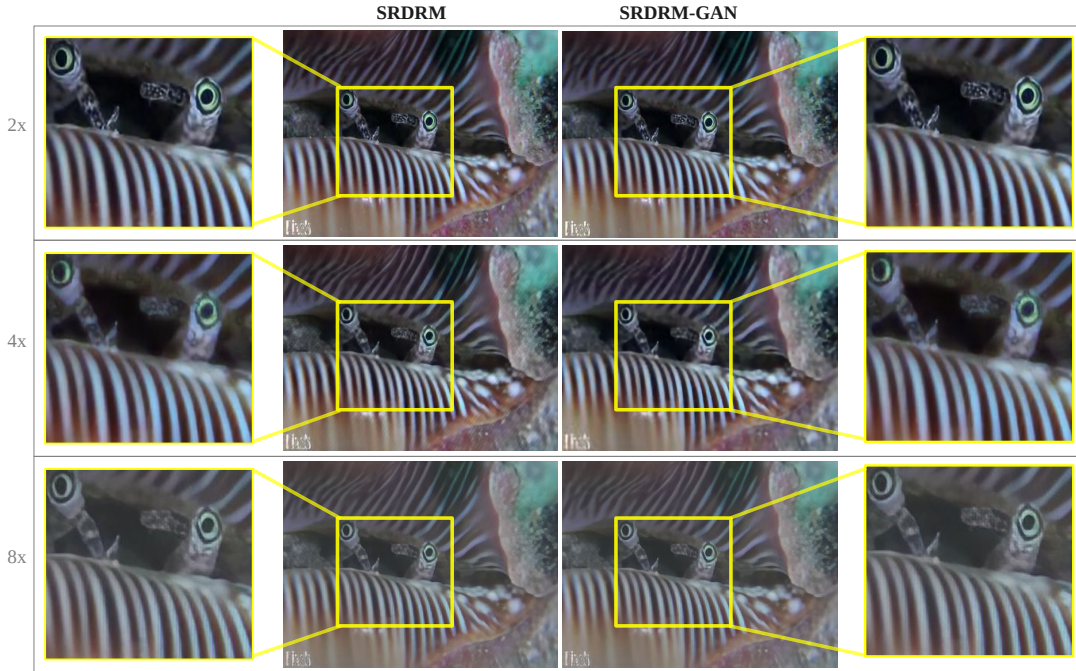


Figure 7.17: Global contrast and texture recovery for  $2\times$ ,  $4\times$ , and  $8\times$  SISR.

### 7.3.10 Qualitative Evaluation: SRDRM and SRDRM-GAN

At first, we analyze the sharpness and color consistency in the generated images of SRDRM and SRDRM-GAN. As Fig. 7.16 suggests, both models generate images that are comparable to the ground truths for  $4\times$  SISR. We observe even better results for  $2\times$  SISR, as it is a relatively less challenging problem. We demonstrate this relative performance margins at various scales in Fig. 7.17. This comparison shows that the global contrast and texture is mostly recovered in the  $2\times$  and  $4\times$  HR images generated by SRDRM and SRDRM-GAN. On the other hand, the  $8\times$  HR images miss the finer details and lack the sharpness in high-texture regions. The state-of-the-art SISR models have also reported such difficulties beyond the  $4\times$  scale [84].

Next, in Fig. 7.18, we provide a qualitative performance comparison with the state-of-the-art models for  $4\times$  SISR. We select multiple  $160 \times 120$  patches on the test images containing interesting textures and objects in contrasting background. Then, we apply all the SISR models (trained on  $4\times$  USR-248 data) to generate respective HR images of size  $640 \times 480$ . In the evaluation, we observe that SRDRM performs at least as well as and often better compared to the generative models, *i.e.*, SRResNet, SRCNN, and DSRCNN. Moreover, SRResNet and SRGAN are prone to inconsistent coloring and over-saturation in bright regions. On the other hand, ESRGAN and EDSRGAN often fail to restore the sharpness and global contrast. Furthermore, SRDRM-GAN generates sharper images and does a better texture recovery than SRDRM (and other generative models) in general. We postulate that the PatchGAN-based discriminator contributes to this, as it forces the generator to learn high-frequency local texture and style information [46]. More qualitative results are provided in the Appendix E.1; moreover, a video demonstration can be seen in <https://youtu.be/qOLZVgrxCwE>.

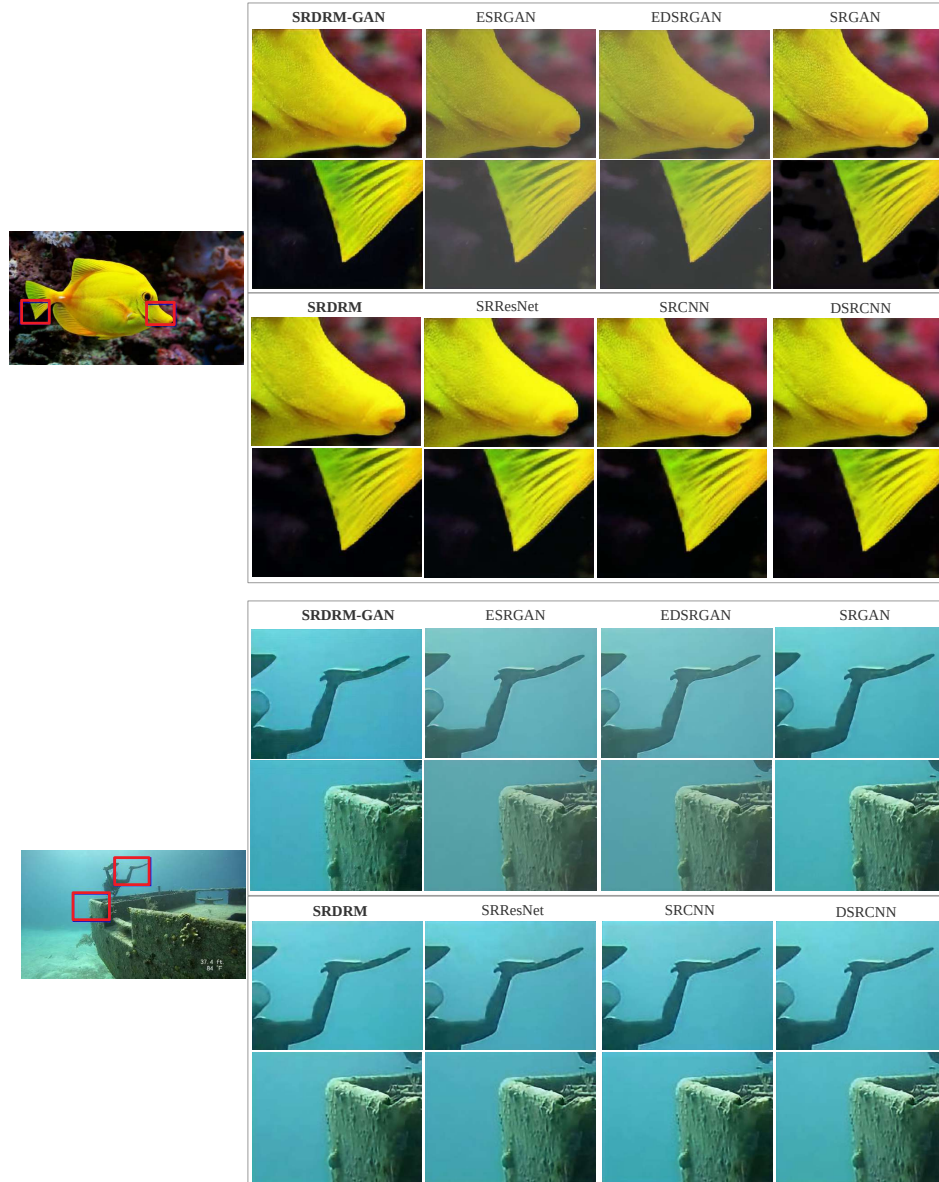


Figure 7.18: Qualitative performance comparison of SRDRM and SRDRM-GAN with SRCNN [72], SRRResNet [88, 84], DSRCNN [133], SRGAN [88], ESRGAN [89], and EDSRGAN [77].

### 7.3.11 Quantitative Evaluation: SRDRM and SRDRM-GAN

We now perform quantitative evaluation of SRDRM and SRDRM-GAN based on PSNR, SSIM, and UIQM. We already introduced these standard metrics in Section 7.3.8; their definition and relevant details are provided in Appendix D.1.

We use a total of 452 test images for the evaluation. As the results in Table 7.10 indicates, the SRDRM-GAN, SRDRM, SRGAN, and SRRResNet produce comparable values for PSNR and SSIM, and perform better than other models. Moreover, SRDRM-GAN outperforms other models by considerable margins in terms of UIQM measure. Furthermore, we compare the quantitative performance of SRDRM and SRDRM-GAN models for different scales (*i.e.*, 2 $\times$ , 4 $\times$ , and 8 $\times$ ); the results are provided in Appendix E.3 (in Table E.1 and E.2). These statistics are consistent with our qualitative analysis.

Table 7.10: Comparison for average PSNR, SSIM, and UIQM values.

Model	$PSNR(G(\mathbf{x}), \mathbf{y})$	$SSIM(G(\mathbf{x}), \mathbf{y})$	$UIQM(G(\mathbf{x}))$
SRResNet	$24.21 \pm 3.45$	$0.70 \pm 0.08$	$2.21 \pm 0.70$
SRCNN	$23.75 \pm 3.26$	$0.69 \pm 0.12$	$2.27 \pm 0.68$
DSRCNN	$23.91 \pm 3.41$	$0.68 \pm 0.10$	$2.33 \pm 0.62$
<b>SRDRM</b>	$24.96 \pm 3.36$	$0.72 \pm 0.11$	$2.35 \pm 0.71$
<b>SRDRM-GAN</b>	$24.77 \pm 3.32$	$0.70 \pm 0.12$	$2.81 \pm 0.56$
ESRGAN	$20.99 \pm 3.12$	$0.58 \pm 0.15$	$2.33 \pm 0.55$
EDSRGAN	$21.88 \pm 2.76$	$0.62 \pm 0.14$	$2.42 \pm 0.84$
SRGAN	$24.76 \pm 3.42$	$0.69 \pm 0.13$	$2.75 \pm 0.66$

Table 7.11: Run-time and memory requirement of SRDRM/SRDRM-GAN on Jetson TX2.

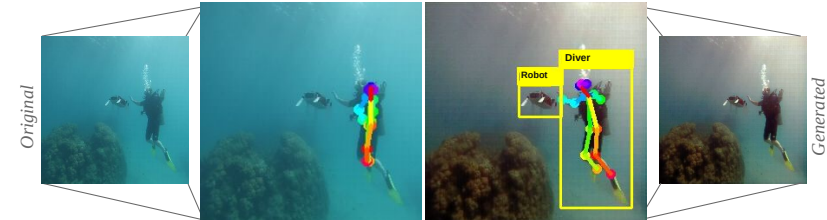
Model	$2\times$	$4\times$	$8\times$
Inference-time (ms)	140.6 ms	145.7 ms	245.7 ms
Frames per second (fps)	7.11 fps	6.86 fps	4.07 fps
Model-size	3.5 MB	8 MB	12 MB

The qualitative and quantitative results suggest that SRDRM and SRDRM-GAN provide good quality HR visualizations for LR image patches, which is potentially useful in tracking fast-moving targets, attention modeling, and detailed understanding of underwater scenes. Therefore, AUVs and ROVs can use this to *zoom in* a particular region of interest (RoI) for detailed and improved visual perception. One operational consideration for using such deep learning-based models in embedded robotic platforms is the computational complexity. As demonstrated in Table 7.11, the memory requirement for the proposed model is only 3.5-12 MB and it runs at 4-7 fps on NVIDIA™ Jetson TX2, which (and similar other embedded computing boards) are widely used by underwater robots [114, 134]. Therefore, it essentially takes about 140-246 milliseconds for a robot to take a closer look at an LR RoI. These results validate the feasibility of using the proposed model for improving real-time perception of visually-guided underwater robots.

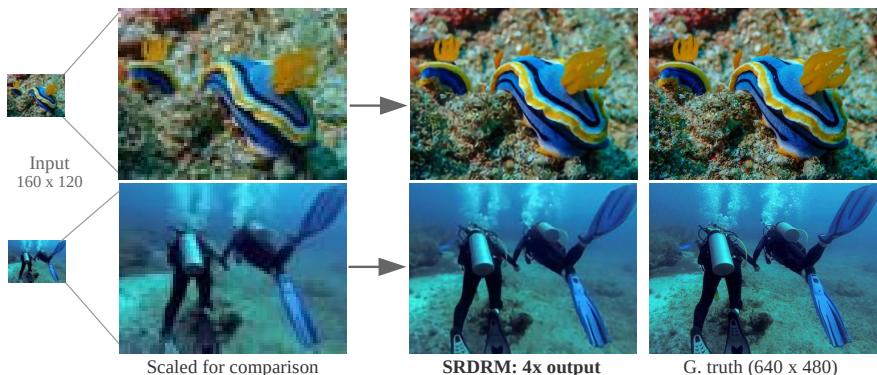
## Chapter 8

# Proposed Research Direction

The following sections present several research problems that we are looking forward to pursuing in the near future. In particular, we discuss the research problems, aspired methodologies, and relevant design choices.



(a) Improved performance for object detection and pose estimation on FUnIE-GAN-enhanced images.



(b) Realistic HR image generation by SRDRM from blurred LR images.

Figure 8.1: Improved visual perception using proposed image enhancement and super-resolution models.

### 8.1 Simultaneous Image Enhancement and Super-Resolution

As illustrated in Fig. 7.14, our proposed image enhancement and super-resolution models (*i.e.*, FUnIE-GAN and SRDRM) are effective in improving underwater image quality in terms of color, contrast, and sharpness. In Section 7.3.8 and 7.3.10, we quantitatively evaluated the degree of improvement and validated their applicability for improving real-time perception of visually-guided underwater robots. One immediate extension is to design a combined model that

can simultaneously learn to enhance and interpolate underwater images at a higher resolution. Specifically, we are trying to design a deep generative model that can learn to generate HR enhanced images from poor quality LR images. The objective is to achieve a better on-board operating performance compared to using two models sequentially (see Table 8.1). We believe that running two models one after another is inefficient as there are possibly a lot of repeated computations, particularly in the earlier layers.

Table 8.1: Comparison of run-time and memory requirement for image enhancement and super-resolution in sequential order (*i.e.*, output of one model is propagated to another).

Model	Output	Run-time (msec)	Memory (MB)
FUnIE-GAN + SRDRM	2 $\times$	206.4	21
FUnIE-GAN + SRDRM	4 $\times$	212.2	25
FUnIE-GAN + SRDRM	8 $\times$	314.5	29

There are quite a few challenges involved in designing such a combined model. First, the training pipeline needs to be ordered correctly, *i.e.*, whether to learn enhancement before up-sampling or vice versa. This influences the choice of loss functions as well. Secondly, designing the minimal network architecture that accommodates the combined end-to-end learning is going to be crucial for ensuring a fast run-time. Moreover, there are no significant research attempts on simultaneous learning of image enhancement and super-resolution in the literature. Hence, it promises to be a challenging and exciting exploration.

## 8.2 Robot-to-robot Relative Pose Estimation from Human Pose

Accurate computation of relative pose is essential in multi-robot estimation problems such as cooperative tracking, localization [135], planning, mapping [136], and more. Unless global positioning information (*e.g.*, GPS) is available, the robots need to estimate their positions and orientations relative to each other based on their exteroceptive sensory measurements and noisy odometry [14]. This process is necessary for registering their measurements to a common frame of reference in order to maintain coordination. Therefore, robust estimation of robot-to-robot relative pose is crucial for deploying a team of robots in GPS-denied environments.

In a cooperative setting, robots with visual sensing capabilities solve the relative pose estimation problem by triangulating mutually visible local features and landmarks. A lack of salient features significantly affects the accuracy of this estimation [137], which eventually hampers the overall success of the operation. Such difficulties often arise in poor visibility conditions underwater due to a lower number of salient features and natural landmarks [138, 3]. Nevertheless, close proximity of human divers to robots is a fairly common occurrence in underwater applications [8]. In addition, humans are frequently present and clearly visible in many social scenarios [2, 139] where natural landmarks are not reliably identifiable due to repeated textures, noisy visual conditions, etc. Hence, the problem of having limited natural landmarks can be alleviated by using mutually visible humans as *markers* (*i.e.*, features correspondences), particularly in human-robot collaborative applications. Despite the potential, the feasibility of using human presence or body-pose for robot-to-robot relative pose estimation has not been explored

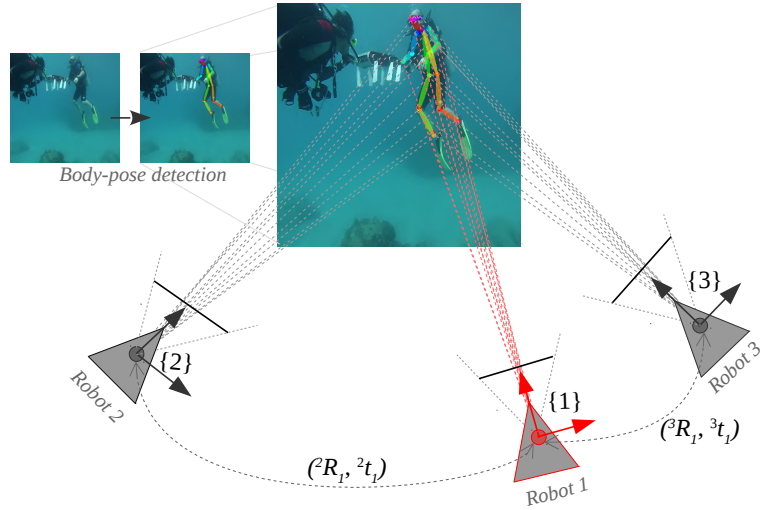


Figure 8.2: A simplified illustration of 3D relative pose estimation between robot 1 and robot 2 (3). The robots know the transformations between their intrinsically calibrated cameras and respective global frames, *i.e.*,  $\{1\}$ ,  $\{2\}$ , and  $\{3\}$ . Robot 1 is considered as the leader (equipped with a stereo camera) and its pose in global coordinates  $({}^1R_G, {}^1t_G)$  is known. Robot 2 (3) finds its unknown global pose by cooperatively localizing itself relative to robot 1 using the human pose-based key-points as common landmarks.

in the literature.

In our work [140], we are formulating a method for computing 6-DOF robot-to-robot transformation between pairs of communicating robots by using mutually detected humans' pose-based key-points as correspondences. As illustrated in Figure 8.2, we adopt a *leader-follower* framework where one of the robots (equipped with a stereo camera) is assigned as a leader. First, the leader robot detects and triangulates 3D positions of the key-points in its own frame of reference. Then the follower robot matches the corresponding 2D projections on its intrinsically calibrated camera and localizes itself by solving the perspective-n-point (PnP) problem [141]. It is to be noted that this entire process of *extrinsic calibration* is automatic and does not require prior knowledge about the robots' initial positions. Additionally, it is straightforward to extend the leader-follower framework for multi-robot teams from the pairwise solutions. Furthermore, if the leader robot has global positioning information, *i.e.*, has a GPS or an ultra-short baseline (USBL) receiver, the follower robots can use that information to localize themselves in the global frame as well.

In addition to designing a conceptual model, we are developing efficient solutions to the practicalities involved in the proposed robot-to-robot pose estimation method. We use Open-Pose [132] for detecting human body-poses in the image space. Although it provides reliable detection performance, the extracted 2D key-points across different views do not necessarily associate as a correspondence. We propose a twofold solution to this; first, we design an efficient person re-identification technique by evaluating the hierarchical similarities of the key-point regions in the image space. We investigate the applicability of state-of-the-art appearance-based person re-identification models [142, 143] as well. Subsequently, we formulate an iterative optimization algorithm that refines the preliminarily associated noisy key-points by further exploiting their local structural properties in respective images. This two-stage process facilitates

efficient and robust key-point correspondences across viewpoints for accurate robot-to-robot relative pose estimation. In the near future, we plan to evaluate the proposed estimation method over a number of terrestrial and underwater field experiments; we will also analyze its feasibility in various multi-robot cooperative systems.

### 8.2.1 Background

The problem of robot-to-robot relative pose estimation has been thoroughly studied for 2D planar robots, particularly using range and bearing sensors. Analytic solutions for determining 3-DOF robot-to-robot transformation using mutual distance and/or bearing measurements involve solving an over-determined system of nonlinear equations [14, 15]. Similar solutions for 3D case, *i.e.*, for determining 6-DOF transformation using inter-robot distance and/or bearing measurements, has been proposed as well [144, 145]. In practice, these analytic solutions are used as an initial estimate for the relative pose, and then iteratively refined using optimization techniques (*e.g.*, nonlinear weighted least-squares) in order to account for noisy observation and uncertainty in the robots' motion.

Robots that rely on visual perception (*i.e.*, use cameras as exteroceptive sensors) solve the relative pose estimation problem by triangulating mutually visible features and landmarks [146]. Therefore, it reduces to solving the PnP problem by using sets of 2D-3D correspondences between geometric features and their projections on respective image planes [141]. Although high-level geometric features (*e.g.*, lines, conics, etc.) have been proposed, point features are typically used in practice for relative pose estimation [147]. Moreover, the PnP problem is solved either using iterative approaches by formulating the over-constrained system ( $n > 3$ ) as a nonlinear least-squares problem, or by using sets of three non-collinear points ( $n = 3$ ) in combination with Random Sample Consensus (RANSAC) to remove outliers [148]. Besides, vision-based approaches often use temporal-filtering methods, the extended Kalman-filter (EKF) in particular, to reduce the effect of noisy measurements in order to provide near-optimal pose estimates [146, 147]. On the other hand, it is also common to simplify the relative pose estimation by attaching specially designed calibration-patterns on each robot [149]. However, this requires that the robots operate at a sufficiently close range, and remain mutually visible.

Human-awareness is essential for autonomous mobile robots operating in social settings and human-robot collaborative applications. A large body of literature and systems exist [8, 150, 2] which focus on the areas of understanding human motion, instructions, behaviors, etc. Additionally, tracking human pose relative to the robot is particularly common in applications such as person tracking [151], following [2], collaborative manipulation [152], behavior imitation [153], etc. However, the feasibility of using humans' presence or their body-poses as markers for robot-to-robot relative pose estimation has not been explored in the literature, which we attempt to address in this work.

### 8.2.2 Preliminary Results: Structure from Motion using Human Pose

We have obtained inspiring results during our early explorations. Specifically, we perform experiments to validate that the human pose-based key-points can be used as reliable correspondences for relative pose estimation. As illustrated in Figure 8.3a, we emulate an experimental

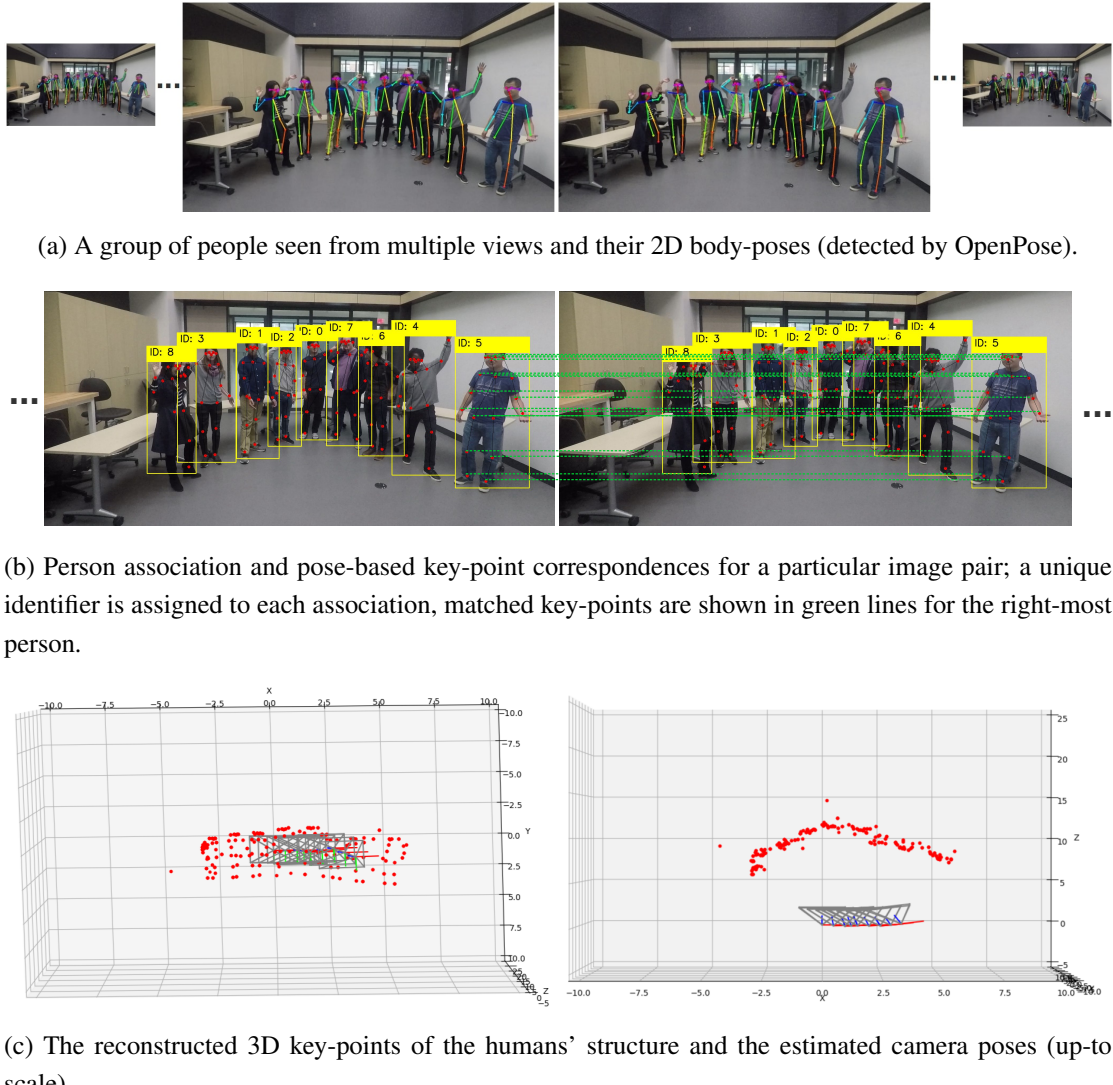


Figure 8.3: Results of estimating *structure from motion* using only human pose-based key-points as features.

set-up for *structure from motion* with humans; we use an intrinsically calibrated monocular camera to capture a group of nine (static) people from multiple views. Here, the goal is to estimate the camera poses and reconstruct the 3D structures of the humans using only their body-poses as features. First, we use OpenPose to detect the human pose-based 2D key-points in the images (Figure 8.3a). Then, we apply the proposed (current version of) person re-identification and key-point refinement processes to find the feature correspondences across multiple views (Figure 8.3b). Subsequently, we follow the standard procedures for *structure from motion* [154]: fundamental matrix computation using 8-point algorithm with RANSAC, essential matrix computation, camera pose estimation by enforcing the Cheirality constraint, and linear triangulation. Finally, the triangulated 3D points and camera poses are refined using bundle adjustment. As demonstrated in Figure 8.3c, the spatial structure of the reconstructed points on the human bodies and the camera poses are consistent with our setup. Moreover, we get an average re-projection error of  $6.85e^{-5}$  pixels which is reasonably accurate.

We are currently working on further improving the important computational components

of the proposed relative pose estimation method, in particular, the person re-identification and key-point refinement processes. Additionally, we plan to perform extensive field experiments in terrestrial and underwater environments to investigate its applicability in real-world applications.

## 8.3 Visual Attention Modeling

The problem of *where to look in the scene* is about finding the regions in the image space that are relevant for a particular task. The task can be either to localize objects, to predict objects' motion/activity, or to find interaction among objects in the scene. Such visual attention modeling can help speed up the salient feature-based task execution for visually-guided underwater robots.

### 8.3.1 Background

Visual attention modeling is a well-studied problem [155, 16] particularly in the area of computer vision, computational neuroscience, and human-robot interaction. The classical approaches [156, 157] are either bottom-up (*i.e.*, stimulus-driven) or top-down (*i.e.*, knowledge- or goal-driven). The stimulus-driven approaches use low-level image features such as luminance, color, texture, and often depth information to quantify feature contrast in the spatial domain. This feature contrast is subsequently exploited for the spatial saliency computation. Automatic saliency prediction over a sequence of frames (*i.e.*, videos) is also explored [9, 18] extensively because spatio-temporal features capture information about the motion and interaction among objects in the scene which are important cues for attention modeling. On the other hand, top-down approaches require an explicit understanding of the context of the scene [158, 17]. These approaches solve the problem of *visual question answering*, *i.e.*, finding the image regions that are relevant to a query.

The state-of-the-art visual attention models [16, 17] use CNNs to extract a hierarchical feature representation in the image space. Various encode-decoder network architectures with skip-connections are typically used to exploit the semantic features at multiple levels of abstraction. The spatial attention prediction is then learned end-to-end from the hierarchical feature representation by supervised training [158, 16]. Temporal deep models such as Long Short-Term Memory (LSTM) networks are also utilized for spatio-temporal learning of attention modeling. These recurrent models are particularly useful in applications such as attention-based video compression, activity recognition, video surveillance, etc. In a contemporary work, Bazzani *et al.* [18] introduce a recurrent mixture density network that learns attention modeling from human fixation data. Such models can be utilized to imitate humans' attention behavior, which is of particular interest to us.

A few research work [159, 160] focus on visual attention modeling for object detection and tracking in underwater videos. However, their usage is limited to salient feature extraction and image enhancement for better object detection performance [161, 162, 163]. Hence, they do not provide solutions for the *where to look* problem. Moreover, there are no large-scale datasets for underwater visual attention modeling to facilitate large-scale supervised training of deep models. We plan to address these limitations in our work.



Figure 8.4: A few illustrations of visual saliency prediction in underwater scenes; such saliency maps facilitate efficient visual search for regions of interest.

### 8.3.2 Desired Capabilities

We plan to design a bottom-up deep visual model that can accurately predict spatial saliency map in the image space. More importantly, we want the model to imitate human attention behavior so that visually-guided AUVs can intelligently identify *interesting* image regions. As shown in Figure 8.4, such saliency prediction can facilitate important decision-making such as where to look, where to go next, which samples to collect, etc. Moreover, in human-robot collaborative settings, a robot can use the saliency map to formulate its actions during implicit interactions [2], *e.g.*, when the companion human is intending to communicate, when to approach the human, when not to interrupt, etc.

We are currently exploring the performance of several state-of-the-art visual attention models on standard datasets. Additionally, we are in the process of preparing a large-scale underwater dataset for semantic segmentation and visual attention modeling. Furthermore, we are formulating a couple of ideas for designing a fast and memory-efficient visual attention model. Once the dataset is prepared, we will be able to train and evaluate various models for underwater applications. Subsequently, we plan to conduct field experiments for performance evaluation and feasibility analysis in real-world settings.

# Chapter 9

## Conclusion

In this paper, we provide robust and efficient solutions for a visually-guided underwater robot to accompany humans in a cooperative underwater mission. In particular, we present vision-based methodologies for autonomous diver following, human-robot communication, automatic image enhancement, and image super-resolution. We describe their algorithms and discuss various practicalities involved in real-time implementations on robotic platforms. Our results from simulation and field experiments validate that these solutions enable a robot to automatically enhance noisy underwater scenes to facilitate an improved visual perception performance. This enhanced vision eventually allows the robot to accurately detect, follow, and interact with the companion humans in unfavorable sensing conditions.

In the near future, we plan to investigate the problem of robot-to-robot relative pose estimation using human body-pose as markers. This will alleviate the problem of having limited natural landmarks in underwater scenes in multi-robot cooperative settings. Visual attention modeling based on humans' activity patterns is another problem of interest in our future research. This feature will potentially enable a visually-guided underwater robot to have a detailed scene understanding for more efficient human-robot cooperative task execution.

# Bibliography

- [1] M. J. Islam, M. Fulton, and J. Sattar, “Toward a Generic Diver-Following Algorithm: Balancing Robustness and Efficiency in Deep Visual Detection,” *IEEE Robotics and Automation Letters (RA-L)*, vol. 4, no. 1, pp. 113–120, 2018.
- [2] M. J. Islam, J. Hong, and J. Sattar, “Person Following by Autonomous Robots: A Categorical Overview,” *In Press at the International Journal of Robotics Research (IJRR)*. *arXiv:1803.08202*, 2018.
- [3] J. Sattar, G. Dudek, O. Chiu, I. Rekleitis, P. Giguere, A. Mills, N. Plamondon, C. Prähacs, Y. Girdhar, M. Nahon *et al.*, “Enabling Autonomous Capabilities in Underwater Robotics,” in *IEEE/RSJ International Conference on Intelligent Robots and Systems (IROS)*. IEEE, 2008, pp. 3628–3634.
- [4] F. Mandic, I. Rendulic, N. Miskovic, and D. Nad, “Underwater Object Tracking using Sonar and USBL Measurements,” *Journal of Sensors*, vol. 2016, 2016.
- [5] K. J. DeMarco, M. E. West, and A. M. Howard, “Sonar-based Detection and Tracking of a Diver for Underwater Human-robot Interaction Scenarios,” in *IEEE International Conference on Systems, Man, and Cybernetics (SMC)*. IEEE, 2013, pp. 2378–2383.
- [6] H. Slabbekoorn, N. Bouton, I. van Opzeeland, A. Coers, C. ten Cate, and A. N. Popper, “A Noisy Spring: the Impact of Globally Rising Underwater Sound Levels on Fish,” *Trends in Ecology & Evolution*, vol. 25, no. 7, pp. 419–427, 2010.
- [7] M. J. Islam and J. Sattar, “Mixed-domain Biological Motion Tracking for Underwater Human-robot Interaction,” in *IEEE International Conference on Robotics and Automation (ICRA)*. IEEE, 2017, pp. 4457–4464.
- [8] M. J. Islam, M. Ho, and J. Sattar, “Understanding Human Motion and Gestures for Underwater Human-Robot Collaboration,” *Journal of Field Robotics (JFR)*, pp. 1–23, 2018.
- [9] C. Fabbri, M. J. Islam, and J. Sattar, “Enhancing Underwater Imagery using Generative Adversarial Networks,” in *IEEE International Conference on Robotics and Automation (ICRA)*. IEEE, 2018, pp. 7159–7165.
- [10] M. J. Islam, M. Ho, and J. Sattar, “Dynamic Reconfiguration of Mission Parameters in Underwater Human-Robot Collaboration,” in *IEEE International Conference on Robotics and Automation (ICRA)*. IEEE, 2018, pp. 1–8.

- [11] M. Fiala, “ARTag, a fiducial marker system using digital techniques,” in *2005 IEEE Computer Society Conference on Computer Vision and Pattern Recognition (CVPR)*, vol. 2. IEEE, 2005, pp. 590–596.
- [12] M. J. Islam, Y. Xia, and J. Sattar, “Fast Underwater Image Enhancement for Improved Visual Perception,” *arXiv preprint arXiv:1903.09766*, 2019.
- [13] M. J. Islam, S. S. Enan, P. Luo, and J. Sattar, “Underwater Image Super-Resolution using Deep Residual Multipliers,” *arXiv preprint arXiv:1909.09437*, 2019.
- [14] X. S. Zhou and S. I. Roumeliotis, “Robot-to-robot Relative Pose Estimation from Range Measurements,” *IEEE Transactions on Robotics (TRO)*, vol. 24, no. 6, pp. 1379–1393, 2008.
- [15] N. Trawny and S. I. Roumeliotis, “On the Global Optimum of Planar, Range-based Robot-to-robot Relative Pose Estimation,” in *Proc. of the IEEE International Conference on Robotics and Automation (ICRA)*. IEEE, 2010, pp. 3200–3206.
- [16] W. Wang and J. Shen, “Deep Visual Attention Prediction,” *IEEE Transactions on Image Processing*, vol. 27, no. 5, pp. 2368–2378, 2017.
- [17] J. Lu, J. Yang, D. Batra, and D. Parikh, “Hierarchical Question-image co-attention for Visual question Answering,” in *Advances in Neural Information Processing Systems*, 2016, pp. 289–297.
- [18] L. Bazzani, H. Larochelle, and L. Torresani, “Recurrent Mixture Density Network for Spatiotemporal Visual Attention,” *arXiv preprint arXiv:1603.08199*, 2016.
- [19] J. Sattar and G. Dudek, “On the Performance of Color Tracking Algorithms for Underwater Robots under Varying Lighting and Visibility,” in *IEEE International Conference on Robotics and Automation (ICRA)*. IEEE, 2006, pp. 3550–3555.
- [20] J. Sattar, P. Giguere, G. Dudek, and C. Prahacs, “A Visual Servoing System for an Aquatic Swimming Robot,” in *IEEE/RSJ International Conference on Intelligent Robots and Systems (IROS)*. IEEE, 2005, pp. 1483–1488.
- [21] J. Sattar and G. Dudek, “Robust Servo-control for Underwater Robots using Banks of Visual Filters,” in *IEEE International Conference on Robotics and Automation (ICRA)*. IEEE, 2009, pp. 3583–3588.
- [22] H. Inoue, T. Tachikawa, and M. Inaba, “Robot Vision System with a Correlation Chip for Real-time Tracking, Optical Flow and Depth Map Generation,” in *IEEE International Conference on Robotics and Automation (ICRA)*. IEEE, 1992, pp. 1621–1626.
- [23] J. Sattar and G. Dudek, “Underwater human-robot interaction via biological motion identification,” in *Proceedings of the International Conference on Robotics: Science and Systems V, RSS*. Seattle, Washington, USA: MIT Press, June 2009, pp. 185–192.

- [24] F. Shkurti, W.-D. Chang, P. Henderson, M. J. Islam, J. C. G. Higuera, J. Li, T. Mander-son, A. Xu, G. Dudek, and J. Sattar, “Underwater Multi-Robot Convoying using Visual Tracking by Detection,” in *IEEE/RSJ International Conference on Intelligent Robots and Systems (IROS)*. IEEE, 2017.
- [25] E. Coronado, J. Villalobos, B. Bruno, and F. Mastrogiovanni, “Gesture-based robot control: Design challenges and evaluation with humans,” in *2017 IEEE International Conference on Robotics and Automation (ICRA)*. IEEE, 2017, pp. 2761–2767.
- [26] S. Chen, H. Ma, C. Yang, and M. Fu, “Hand gesture based robot control system using leap motion,” in *International Conference on Intelligent Robotics and Applications*. Springer, 2015, pp. 581–591.
- [27] M. T. Wolf, C. Assad, M. T. Vernacchia, J. Fromm, and H. L. Jethani, “Gesture-based robot control with variable autonomy from the JPL BioSleeve,” in *2013 IEEE International Conference on Robotics and Automation (ICRA)*. IEEE, 2013, pp. 1160–1165.
- [28] G. Dudek, P. Giguere, and J. Sattar, “Sensor-based Behavior Control for an Autonomous Underwater Vehicle,” in *Experimental Robotics*. Springer, 2008, pp. 267–276.
- [29] G. Dudek, M. Jenkin, C. Prahacs, A. Hogue, J. Sattar, P. Giguere, A. German, H. Liu, S. Saunderson, A. Ripsman *et al.*, “A Visually Guided Swimming Robot,” in *IEEE/RSJ International Conference on Intelligent Robots and Systems (IROS)*. IEEE, 2005, pp. 3604–3609.
- [30] E. Olson, “AprilTag: A robust and flexible visual fiducial system,” in *Robotics and Automation (ICRA), 2011 IEEE International Conference on*. IEEE, 2011, pp. 3400–3407.
- [31] J. Sattar, E. Bourque, P. Giguere, and G. Dudek, “Fourier Tags: Smoothly Degradable Fiducial Markers for use in Human-robot Interaction,” in *Canadian Conference on Computer and Robot Vision (CRV)*. IEEE, 2007, pp. 165–174.
- [32] G. Dudek, J. Sattar, and A. Xu, “A Visual Language for Robot Control and Programming: A Human-interface Study,” in *IEEE International Conference on Robotics and Automation (ICRA)*. IEEE, 2007, pp. 2507–2513.
- [33] A. Xu, G. Dudek, and J. Sattar, “A Natural Gesture Interface for Operating Robotic Systems,” in *IEEE International Conference on Robotics and Automation (ICRA)*. IEEE, 2008, pp. 3557–3563.
- [34] P. Molchanov, S. Gupta, K. Kim, and J. Kautz, “Hand gesture recognition with 3D convolutional neural networks,” in *Proceedings of 2015 IEEE conference on computer vision and pattern recognition workshops*. IEEE, 2015, pp. 1–7.
- [35] N. Neverova, C. Wolf, G. W. Taylor, and F. Nebout, “Multi-scale deep learning for gesture detection and localization,” in *Workshop at the European conference on computer vision*. Springer, 2014, pp. 474–490.

- [36] Tensorflow, “Tensorflow Object Detection Zoo,” [https://github.com/tensorflow/models/blob/master/research/object\\_detection/g3doc/detection\\_model\\_zoo.md](https://github.com/tensorflow/models/blob/master/research/object_detection/g3doc/detection_model_zoo.md), 2017, accessed: 2-20-2019.
- [37] M. Irani and S. Peleg, “Motion Analysis for Image Enhancement: Resolution, Occlusion, and Transparency,” *Journal of Visual Communication and Image Representation*, vol. 4, no. 4, pp. 324–335, 1993.
- [38] Z.-u. Rahman, D. J. Jobson, and G. A. Woodell, “Retinex Processing for Automatic Image Enhancement,” *Journal of Electronic Imaging*, vol. 13, no. 1, pp. 100–111, 2004.
- [39] R. Zhang, P. Isola, and A. A. Efros, “Colorful Image Colorization,” in *European Conference on Computer Vision (ECCV)*. Springer, 2016, pp. 649–666.
- [40] Z. Cheng, Q. Yang, and B. Sheng, “Deep Colorization,” in *Proc. of the IEEE International Conference on Computer Vision (ICCV)*, 2015, pp. 415–423.
- [41] B. Cai, X. Xu, K. Jia, C. Qing, and D. Tao, “DehazeNet: An End-to-end System for Single Image Haze Removal,” *IEEE Transactions on Image Processing*, vol. 25, no. 11, pp. 5187–5198, 2016.
- [42] W. Yang, R. T. Tan, J. Feng, J. Liu, Z. Guo, and S. Yan, “Joint Rain Detection and Removal via Iterative Region Dependent Multi-task Learning,” *CoRR, abs/1609.07769*, vol. 2, no. 3, 2016.
- [43] P. Svoboda, M. Hradis, D. Barina, and P. Zemcik, “Compression Artifacts Removal using Convolutional Neural Networks,” *arXiv preprint arXiv:1605.00366*, 2016.
- [44] I. Goodfellow, J. Pouget-Abadie, M. Mirza, B. Xu, D. Warde-Farley, S. Ozair, A. Courville, and Y. Bengio, “Generative Adversarial Nets,” in *Advances in Neural Information Processing Systems (NIPS)*, 2014, pp. 2672–2680.
- [45] L. A. Gatys, A. S. Ecker, and M. Bethge, “Image Style Transfer using Convolutional Neural Networks,” in *Proc. of the IEEE Conference on Computer Vision and Pattern Recognition (CVPR)*, 2016, pp. 2414–2423.
- [46] P. Isola, J.-Y. Zhu, T. Zhou, and A. A. Efros, “Image-to-image Translation with Conditional Adversarial Networks,” in *Proc. of the IEEE Conference on Computer Vision and Pattern Recognition (CVPR)*, 2017, pp. 1125–1134.
- [47] M. Arjovsky, S. Chintala, and L. Bottou, “Wasserstein Generative Adversarial Networks,” in *International Conference on Machine Learning (ICML)*, 2017, pp. 214–223.
- [48] J. Zhao, M. Mathieu, and Y. LeCun, “Energy-based Generative Adversarial Network,” *arXiv preprint arXiv:1609.03126*, 2017.
- [49] X. Mao, Q. Li, H. Xie, R. Y. Lau, Z. Wang, and S. Paul Smolley, “Least Squares Generative Adversarial Networks,” in *Proc. of the IEEE International Conference on Computer Vision (ICCV)*, 2017, pp. 2794–2802.

- [50] M. Mirza and S. Osindero, “Conditional Generative Adversarial Nets,” *arXiv preprint arXiv:1411.1784*, 2014.
- [51] J.-Y. Zhu, T. Park, P. Isola, and A. A. Efros, “Unpaired Image-to-image Translation using Cycle-consistent Adversarial Networks,” in *Proc. of the IEEE International Conference on Computer Vision (ICCV)*, 2017, pp. 2223–2232.
- [52] Z. Yi, H. Zhang, P. Tan, and M. Gong, “DualGAN: Unsupervised Dual Learning for Image-to-image Translation,” in *Proc. of the IEEE International Conference on Computer Vision (ICCV)*, 2017, pp. 2849–2857.
- [53] Y.-S. Chen, Y.-C. Wang, M.-H. Kao, and Y.-Y. Chuang, “Deep Photo Enhancer: Unpaired Learning for Image Enhancement from Photographs with GANs,” in *Proc. of the IEEE Conference on Computer Vision and Pattern Recognition (CVPR)*. IEEE, 2018, pp. 6306–6314.
- [54] J. Park, D. K. Han, and H. Ko, “Adaptive Weighted Multi-Discriminator CycleGAN for Underwater Image Enhancement,” *Journal of Marine Science and Engineering*, vol. 7, no. 7, p. 200, 2019.
- [55] A. Ignatov, N. Kobyshev, R. Timofte, K. Vanhoey, and L. Van Gool, “DSLR-quality Photos on Mobile Devices with Deep Convolutional Networks,” in *Proc. of the IEEE International Conference on Computer Vision (ICCV)*, 2017, pp. 3277–3285.
- [56] H. Lu, Y. Li, and S. Serikawa, “Underwater Image Enhancement using Guided Trigonometric Bilateral Filter and Fast Automatic Color Correction,” in *IEEE International Conference on Image Processing*. IEEE, 2013, pp. 3412–3416.
- [57] S. Zhang, T. Wang, J. Dong, and H. Yu, “Underwater Image Enhancement via Extended Multi-scale Retinex,” *Neurocomputing*, vol. 245, pp. 1–9, 2017.
- [58] P. Liu, G. Wang, H. Qi, C. Zhang, H. Zheng, and Z. Yu, “Underwater Image Enhancement With a Deep Residual Framework,” *IEEE Access*, vol. 7, pp. 94 614–94 629, 2019.
- [59] X. Yu, Y. Qu, and M. Hong, “Underwater-GAN: Underwater Image Restoration via Conditional Generative Adversarial Network,” in *International Conference on Pattern Recognition*. Springer, 2018, pp. 66–75.
- [60] J. Li, K. A. Skinner, R. M. Eustice, and M. Johnson-Roberson, “WaterGAN: Unsupervised Generative Network to Enable Real-time Color Correction of Monocular Underwater Images,” *IEEE Robotics and Automation Letters (RAL)*, vol. 3, no. 1, pp. 387–394, 2018.
- [61] W. T. Freeman, T. R. Jones, and E. C. Pasztor, “Example-based Super-resolution,” *IEEE Computer Graphics and Applications*, no. 2, pp. 56–65, 2002.
- [62] H. Chang, D.-Y. Yeung, and Y. Xiong, “Super-resolution Through Neighbor Embedding,” in *Proc. of the IEEE Conference on Computer Vision and Pattern Recognition (CVPR)*, vol. 1. IEEE, 2004, pp. I–I.

- [63] D. O. Melville and R. J. Blaikie, “Super-resolution Imaging through a Planar Silver Layer,” *Optics Express*, vol. 13, no. 6, pp. 2127–2134, 2005.
- [64] J. Sun, Z. Xu, and H.-Y. Shum, “Image Super-resolution using Gradient Profile Prior,” in *IEEE Conference on Computer Vision and Pattern Recognition (CVPR)*. IEEE, 2008, pp. 1–8.
- [65] K. I. Kim and Y. Kwon, “Single-image Super-resolution using Sparse Regression and Natural Image Prior,” *IEEE Transactions on Pattern Analysis and Machine Intelligence*, vol. 32, no. 6, pp. 1127–1133, 2010.
- [66] M. Protter, M. Elad, H. Takeda, and P. Milanfar, “Generalizing the Nonlocal-means to Super-resolution Reconstruction,” *IEEE Transactions on Image Processing*, vol. 18, no. 1, pp. 36–51, 2008.
- [67] D. Glasner, S. Bagon, and M. Irani, “Super-resolution from a Single Image,” in *IEEE International Conference on Computer Vision (ICCV)*. IEEE, 2009, pp. 349–356.
- [68] J. Yang, Z. Wang, Z. Lin, S. Cohen, and T. Huang, “Coupled Dictionary Training for Image Super-resolution,” *IEEE Transactions on Image Processing*, vol. 21, no. 8, pp. 3467–3478, 2012.
- [69] J.-B. Huang, A. Singh, and N. Ahuja, “Single Image Super-resolution from Transformed Self-exemplars,” in *Proc. of the IEEE Conference on Computer Vision and Pattern Recognition (CVPR)*, 2015, pp. 5197–5206.
- [70] J. Yang, J. Wright, T. S. Huang, and Y. Ma, “Image Super-resolution via Sparse Representation,” *IEEE Transactions on Image Processing*, vol. 19, no. 11, pp. 2861–2873, 2010.
- [71] S. Schulter, C. Leistner, and H. Bischof, “Fast and Accurate Image Upscaling with Super-resolution Forests,” in *Proc. of the IEEE Conference on Computer Vision and Pattern Recognition (CVPR)*, 2015, pp. 3791–3799.
- [72] C. Dong, C. C. Loy, K. He, and X. Tang, “Image Super-resolution using Deep Convolutional Networks,” *IEEE Transactions on Pattern Analysis and Machine Intelligence*, vol. 38, no. 2, pp. 295–307, 2015.
- [73] J. Johnson, A. Alahi, and L. Fei-Fei, “Perceptual Losses for Real-time Style Transfer and Super-resolution,” in *European Conference on Computer Vision (ECCV)*. Springer, 2016, pp. 694–711.
- [74] J. Kim, J. Kwon Lee, and K. Mu Lee, “Accurate Image Super-resolution using Very Deep Convolutional Networks,” in *Proc. of the IEEE Conference on Computer Vision and Pattern Recognition (CVPR)*, 2016, pp. 1646–1654.
- [75] ——, “Deeply-recursive Convolutional Network for Image Super-resolution,” in *Proc. of the IEEE Conference on Computer Vision and Pattern Recognition (CVPR)*, 2016, pp. 1637–1645.

- [76] D. Liu, Z. Wang, B. Wen, J. Yang, W. Han, and T. S. Huang, “Robust Single Image Super-resolution via Deep Networks with Sparse Prior,” *IEEE Transactions on Image Processing*, vol. 25, no. 7, pp. 3194–3207, 2016.
- [77] B. Lim, S. Son, H. Kim, S. Nah, and K. Mu Lee, “Enhanced Deep Residual Networks for Single Image Super-resolution,” in *Proc. of the IEEE Conference on Computer Vision and Pattern Recognition (CVPR) workshops*, 2017, pp. 136–144.
- [78] Y. Tai, J. Yang, and X. Liu, “Image Super-resolution via Deep Recursive Residual Network,” in *Proc. of the IEEE Conference on Computer Vision and Pattern Recognition (CVPR)*, 2017, pp. 3147–3155.
- [79] W. Shi, J. Caballero, F. Huszár, J. Totz, A. P. Aitken, R. Bishop, D. Rueckert, and Z. Wang, “Real-time Single Image and Video Super-resolution using an Efficient Sub-pixel Convolutional Neural Network,” in *Proc. of the IEEE Conference on Computer Vision and Pattern Recognition (CVPR)*, 2016, pp. 1874–1883.
- [80] C. Dong, C. C. Loy, and X. Tang, “Accelerating the Super-resolution Convolutional Neural Network,” in *European Conference on Computer Vision (ECCV)*. Springer, 2016, pp. 391–407.
- [81] W.-S. Lai, J.-B. Huang, N. Ahuja, and M.-H. Yang, “Deep Laplacian Pyramid Networks for Fast and Accurate Super-resolution,” in *Proc. of the IEEE Conference on Computer Vision and Pattern Recognition (CVPR)*, 2017, pp. 624–632.
- [82] T. Tong, G. Li, X. Liu, and Q. Gao, “Image Super-resolution using Dense Skip Connections,” in *Proc. of the IEEE International Conference on Computer Vision (ICCV)*, 2017, pp. 4799–4807.
- [83] Y. Zhang, Y. Tian, Y. Kong, B. Zhong, and Y. Fu, “Residual Dense Network for Image Super-resolution,” in *Proc. of the IEEE Conference on Computer Vision and Pattern Recognition (CVPR)*, 2018, pp. 2472–2481.
- [84] W. Yang, X. Zhang, Y. Tian, W. Wang, J.-H. Xue, and Q. Liao, “Deep learning for Single Image Super-resolution: A Brief Review,” *IEEE Transactions on Multimedia*, 2019.
- [85] C. K. Sønderby, J. Caballero, L. Theis, W. Shi, and F. Huszár, “Amortised Map Inference for Image Super-resolution,” *arXiv preprint arXiv:1610.04490*, 2016.
- [86] M. S. Sajjadi, B. Scholkopf, and M. Hirsch, “Enhancenet: Single Image Super-resolution through Automated Texture Synthesis,” in *Proc. of the IEEE International Conference on Computer Vision (ICCV)*, 2017, pp. 4491–4500.
- [87] Y. Chen, F. Shi, A. G. Christodoulou, Y. Xie, Z. Zhou, and D. Li, “Efficient and Accurate MRI Super-resolution using a Generative Adversarial Network and 3D Multi-level Densely Connected Network,” in *International Conference on Medical Image Computing and Computer-Assisted Intervention*. Springer, 2018, pp. 91–99.

- [88] C. Ledig, L. Theis, F. Huszár, J. Caballero, A. Cunningham, A. Acosta, A. Aitken, A. Tejani, J. Totz, Z. Wang *et al.*, “Photo-realistic Single Image Super-resolution using a Generative Adversarial Network,” in *Proc. of the IEEE Conference on Computer Vision and Pattern Recognition (CVPR)*, 2017, pp. 4681–4690.
- [89] X. Wang, K. Yu, S. Wu, J. Gu, Y. Liu, C. Dong, Y. Qiao, and C. Change Loy, “Esrgan: Enhanced Super-resolution Generative Adversarial Networks,” in *Proc. of the European Conference on Computer Vision (ECCV)*, 2018, pp. 0–0.
- [90] O. Kupyn, V. Budzan, M. Mykhailych, D. Mishkin, and J. Matas, “Deblurgan: Blind Motion Deblurring using Conditional Adversarial Networks,” in *Proc. of the IEEE Conference on Computer Vision and Pattern Recognition (CVPR)*, 2018, pp. 8183–8192.
- [91] Y. Yuan, S. Liu, J. Zhang, Y. Zhang, C. Dong, and L. Lin, “Unsupervised Image Super-resolution using Cycle-in-cycle Generative Adversarial Networks,” in *Proc. of the IEEE Conference on Computer Vision and Pattern Recognition (CVPR) Workshops*, 2018, pp. 701–710.
- [92] Y. Chen, B. Yang, M. Xia, W. Li, K. Yang, and X. Zhang, “Model-based Super-resolution Reconstruction Techniques for Underwater Imaging,” in *Photonics and Optoelectronics Meetings (POEM): Optoelectronic Sensing and Imaging*, vol. 8332. International Society for Optics and Photonics, 2012, p. 83320G.
- [93] F. Fan, K. Yang, B. Fu, M. Xia, and W. Zhang, “Application of Blind Deconvolution Approach with Image Quality Metric in Underwater Image Restoration,” in *International Conference on Image Analysis and Signal Processing*. IEEE, 2010, pp. 236–239.
- [94] Y. Yu and F. Liu, “System of Remote-operated-vehicle-based Underwater Blurred Image Restoration,” *Optical Engineering*, vol. 46, no. 11, p. 116002, 2007.
- [95] E. Quevedo, E. Delory, G. Callicó, F. Tobajas, and R. Sarmiento, “Underwater Video Enhancement using Multi-camera Super-resolution,” *Optics Communications*, vol. 404, pp. 94–102, 2017.
- [96] X. Sun, J. Shi, J. Dong, and X. Wang, “Fish Recognition from Low-resolution Underwater Images,” in *International Congress on Image and Signal Processing, BioMedical Engineering and Informatics (CISP-BMEI)*. IEEE, 2016, pp. 471–476.
- [97] B. Espiau, F. Chaumette, and P. Rives, “A New Approach to Visual Servoing in Robotics,” *IEEE Transactions on Robotics and Automation*, vol. 8, no. 3, pp. 313–326, 1992.
- [98] A. V. Oppenheim, A. S. Willsky, and S. H. Nawab, *Signals & Systems (2nd ed.)*. Upper Saddle River, NJ, USA: Prentice-Hall, Inc., 1996.
- [99] L. R. Rabiner, “A Tutorial on Hidden Markov Models and Selected Applications in Speech Recognition,” *Proceedings of the IEEE*, vol. 77, no. 2, pp. 257–286, 1989.
- [100] C. L. Zitnick and P. Dollár, “Edge boxes: Locating object proposals from edges,” in *European Conference on Computer Vision*. Springer, 2014, pp. 391–405.

- [101] S. Ren, K. He, R. Girshick, and J. Sun, “Faster R-CNN: Towards real-time object detection with region proposal networks,” in *Advances in Neural Information Processing Systems (NIPS)*, 2015.
- [102] C. Szegedy, V. Vanhoucke, S. Ioffe, J. Shlens, and Z. Wojna, “Rethinking the inception architecture for computer vision,” in *Proceedings of the IEEE Conference on Computer Vision and Pattern Recognition*. IEEE, 2016, pp. 2818–2826.
- [103] W. Liu, D. Anguelov, D. Erhan, C. Szegedy, S. Reed, C.-Y. Fu, and A. C. Berg, “SSD: Single Shot Multibox Detector,” in *European Conference on Computer Vision (ECCV)*. Springer, 2016, pp. 21–37.
- [104] M. Sandler, A. Howard, M. Zhu, A. Zhmoginov, and L.-C. Chen, “Inverted residuals and linear bottlenecks: Mobile networks for classification, detection and segmentation,” *arXiv preprint arXiv:1801.04381*, 2018.
- [105] A. G. Howard, M. Zhu, B. Chen, D. Kalenichenko, W. Wang, T. Weyand, M. Andreetto, and H. Adam, “MobileNets: Efficient Convolutional Neural Networks for Mobile Vision Applications,” *arXiv preprint arXiv:1704.04861*, 2017.
- [106] J. Redmon and A. Farhadi, “YOLO9000: Better, Faster, Stronger,” *arXiv preprint arXiv:1612.08242*, 2016.
- [107] J. Redmon and A. Farhadi, “Tiny YOLO,” <https://pjreddie.com/darknet/yolo/>, 2017, accessed: 11-10-2018.
- [108] V. Oliveira and A. Conci, “Skin detection using HSV color space,” in *H. Pedrini, & J. Marques de Carvalho, Workshops of Sibgrapi*, 2009, pp. 1–2.
- [109] H.-S. Yeo, B.-G. Lee, and H. Lim, “Hand tracking and gesture recognition system for human-computer interaction using low-cost hardware,” *Multimedia Tools and Applications*, vol. 74, no. 8, pp. 2687–2715, 2015.
- [110] O. Ronneberger, P. Fischer, and T. Brox, “U-Net: Convolutional Networks for Biomedical Image Segmentation,” in *International Conference on Medical Image Computing and Computer-assisted Intervention*. Springer, 2015, pp. 234–241.
- [111] A. L. Maas, A. Y. Hannun, and A. Y. Ng, “Rectifier Nonlinearities Improve Neural Network Acoustic Models,” in *International Conference on Machine Learning (ICML)*, vol. 30, no. 1, 2013, p. 3.
- [112] S. Ioffe and C. Szegedy, “Batch Normalization: Accelerating Deep Network Training by Reducing Internal Covariate Shift,” *CoRR, abs/1502.03167*, 2015.
- [113] GoPro, “GoPro Hero 5,” <https://gopro.com/>, 2016, accessed: 8-15-2019.
- [114] G. Dudek, P. Giguere, C. Prahacs, S. Saunderson, J. Sattar, L.-A. Torres-Mendez, Jenkin *et al.*, “Aqua: An Amphibious Autonomous Robot,” *Computer*, vol. 40, no. 1, pp. 46–53, 2007.

- [115] BlueRobotics, “Low-light HD USB Camera,” <https://www.bluerobotics.com/>, 2016, accessed: 3-15-2019.
- [116] OpenROV, “TRIDENT,” <https://www.openrov.com/>, 2017, accessed: 8-15-2019.
- [117] J. Deng, W. Dong, R. Socher, L.-J. Li, K. Li, and L. Fei-Fei, “ImageNet: A Large-scale Hierarchical Image Database,” in *Proc. of the IEEE Conference on Computer Vision and Pattern Recognition (CVPR)*. IEEE, 2009, pp. 248–255.
- [118] V. Nair and G. E. Hinton, “Rectified Linear Units Improve Restricted Boltzmann Machines,” in *Proc. of the International Conference on Machine Learning (ICML)*, 2010, pp. 807–814.
- [119] T. Raiko, H. Valpola, and Y. LeCun, “Deep Learning Made Easier by Linear Transformations in Perceptrons,” in *Artificial Intelligence and Statistics*, 2012, pp. 924–932.
- [120] Weights and Biases, Inc, “SuperRes Challenge,” <https://github.com/wandb/superres>, 2016, accessed: 8-30-2019.
- [121] O. CA, “OpenROV Underwater Drone 2.8,” <https://www.openrov.com/products/openrov28/>, accessed: 8-30-2017.
- [122] NVIDIA, “Embedded Machine Learning,” [devblogs.nvidia.com/parallelforall/](https://devblogs.nvidia.com/parallelforall/), 2014, accessed: 2-2-2019.
- [123] LIN, TZUTA, “LabelImg,” <https://github.com/tzutalin/labelImg>, 2017, accessed: 10-10-2019.
- [124] M. Abadi, P. Barham, J. Chen, Z. Chen, A. Davis, J. Dean *et al.*, “TensorFlow: A System for Large-scale Machine Learning,” in *USENIX Symposium on Operating Systems Design and Implementation (OSDI)*, 2016, pp. 265–283.
- [125] T. Tieleman and G. Hinton, “Lecture 6.5-rmsprop: Divide the gradient by a running average of its recent magnitude,” *COURSERA: Neural networks for machine learning*, vol. 4, no. 2, pp. 26–31, 2012.
- [126] D. P. Kingma and J. Ba, “Adam: A method for stochastic optimization,” *arXiv preprint arXiv:1412.6980*, 2014.
- [127] D. Meger, F. Shkurti, D. C. Poza, P. Giguere, and G. Dudek, “3d trajectory synthesis and control for a legged swimming robot,” in *IEEE/RSJ International Conference on Intelligent Robots and Systems (IROS)*. IEEE, 2014, pp. 2257–2264.
- [128] J. Li, X. Liang, Y. Wei, T. Xu, J. Feng, and S. Yan, “Perceptual Generative Adversarial Networks for Small Object Detection,” in *Proc. of the IEEE Conference on Computer Vision and Pattern Recognition (CVPR)*, 2017, pp. 1222–1230.
- [129] A. Hore and D. Ziou, “Image Quality Metrics: PSNR vs. SSIM,” in *International Conference on Pattern Recognition*. IEEE, 2010, pp. 2366–2369.

- [130] K. Panetta, C. Gao, and S. Agaian, “Human-visual-system-inspired Underwater Image Quality Measures,” *IEEE Journal of Oceanic Engineering*, vol. 41, no. 3, pp. 541–551, 2016.
- [131] R. Liu, M. Hou, X. Fan, and Z. Luo, “Real-world Underwater Enhancement: Challenging, Benchmark and Efficient Solutions,” *arXiv preprint arXiv:1901.05320*, 2019.
- [132] Z. Cao, T. Simon, S.-E. Wei, and Y. Sheikh, “Realtime Multi-person 2D Pose Estimation using Part Affinity Fields,” in *IEEE Conference on Computer Vision and Pattern Recognition (CVPR)*, 2017, pp. 7291–7299.
- [133] X.-J. Mao, C. Shen, and Y.-B. Yang, “Image Restoration using Convolutional Auto-encoders with Symmetric Skip Connections,” *arXiv preprint arXiv:1606.08921*, 2016.
- [134] QUT Robotics Team, “RangerBot,” <https://research.qut.edu.au/ras/research/rangerbot/>, 2018, accessed: 8-15-2019.
- [135] I. M. Rekleitis, G. Dudek, and E. E. Milios, “Multi-robot Cooperative Localization: A Study of Trade-offs Between Efficiency and Accuracy,” in *Proc. of the IEEE/RSJ International Conference on Intelligent Robots and Systems (IROS)*, vol. 3. IEEE, 2002, pp. 2690–2695.
- [136] S. Se, D. G. Lowe, and J. J. Little, “Vision-based Global Localization and Mapping for Mobile Robots,” *IEEE Transactions on Robotics (TRO)*, vol. 21, no. 3, pp. 364–375, 2005.
- [137] C. Valgren and A. J. Lilienthal, “SIFT, SURF & Seasons: Appearance-based Long-term Localization in Outdoor Environments,” *Robotics and Autonomous Systems*, vol. 58, no. 2, pp. 149–156, 2010.
- [138] H. Damron, A. Q. Li, and I. Rekleitis, “Underwater Surveying via Bearing only Cooperative Localization,” in *Proc. of the IEEE/RSJ International Conference on Intelligent Robots and Systems (IROS)*. IEEE, 2018, pp. 3957–3963.
- [139] R. Kümmerle, M. Ruhnke, B. Steder, C. Stachniss, and W. Burgard, “A Navigation System for Robots Operating in Crowded Urban Environments,” in *Proc. of the IEEE International Conference on Robotics and Automation (ICRA)*. IEEE, 2013, pp. 3225–3232.
- [140] M. J. Islam, J. Mo, and J. Sattar, “Robot-to-Robot Relative Pose Estimation using Humans as Markers,” *arXiv preprint arXiv:1903.00820*, 2019.
- [141] Y. Zheng, Y. Kuang, S. Sugimoto, K. Astrom, and M. Okutomi, “Revisiting the PnP Problem: A Fast, General and Optimal Solution,” in *Proc. of the IEEE International Conference on Computer Vision (ICCV)*, 2013, pp. 2344–2351.
- [142] E. Ahmed, M. Jones, and T. K. Marks, “An Improved Deep Learning Architecture for Person Re-identification,” in *IEEE Conference on Computer Vision and Pattern Recognition (CVPR)*, 2015, pp. 3908–3916.

- [143] W. Li, R. Zhao, T. Xiao, and X. Wang, “Deepreid: Deep Filter Pairing Neural Network for Person Re-identification,” in *IEEE Conference on Computer Vision and Pattern Recognition (CVPR)*, 2014, pp. 152–159.
- [144] X. S. Zhou and S. I. Roumeliotis, “Determining the Robot-to-robot 3D Relative Pose using Combinations of Range and Bearing Measurements (Part II),” in *IEEE International Conference on Robotics and Automation (ICRA)*. IEEE, 2011, pp. 4736–4743.
- [145] N. Trawny, X. S. Zhou, K. Zhou, and S. I. Roumeliotis, “Inter-robot transformations in 3D,” *IEEE Transactions on Robotics (TRO)*, vol. 26, no. 2, pp. 226–243, 2010.
- [146] J. Wang and W. J. Wilson, “3D Relative Position and Orientation Estimation using Kalman Filter for Robot Control,” in *Proc. of the IEEE International Conference on Robotics and Automation (ICRA)*. IEEE, 1992, pp. 2638–2645.
- [147] F. Janabi-Sharifi and M. Marey, “A Kalman-filter-based Method for Pose estimation in Visual Servoing,” *IEEE transactions on Robotics (TRO)*, vol. 26, no. 5, pp. 939–947, 2010.
- [148] M. A. Fischler and R. C. Bolles, “Random Sample Consensus: A Paradigm for Model Fitting with Applications to Image Analysis and Automated Cartography,” *Communications of the ACM*, vol. 24, no. 6, pp. 381–395, 1981.
- [149] I. Rekleitis, D. Meger, and G. Dudek, “Simultaneous Planning, Localization, and Mapping in a Camera Sensor Network,” *Robotics and Autonomous Systems*, vol. 54, no. 11, pp. 921–932, 2006.
- [150] R. Mead and M. J. Matarić, “Autonomous Human–robot Proxemics: Socially aware Navigation based on Interaction Potential,” *Autonomous Robots*, vol. 41, no. 5, pp. 1189–1201, 2017.
- [151] M. Montemerlo, S. Thrun, and W. Whittaker, “Conditional Particle Filters for Simultaneous Mobile Robot Localization and People-tracking,” in *Proc. of the IEEE International Conference on Robotics and Automation (ICRA)*, vol. 1. IEEE, 2002, pp. 695–701.
- [152] J. Mainprice and D. Berenson, “Human-robot Collaborative Manipulation Planning using Early Prediction of Human Motion,” in *Proc. of the IEEE/RSJ International Conference on Intelligent Robots and Systems (IROS)*. IEEE, 2013, pp. 299–306.
- [153] J. Lei, M. Song, Z.-N. Li, and C. Chen, “Whole-body Humanoid Robot Imitation with Pose Similarity Evaluation,” *Signal Processing*, vol. 108, pp. 136–146, 2015.
- [154] R. Hartley and A. Zisserman, *Multiple View Geometry in Computer Vision*. Cambridge University Press, 2003.
- [155] A. Borji and L. Itti, “State-of-the-art in Visual Attention Modeling,” *IEEE Transactions on Pattern Analysis and Machine Intelligence*, vol. 35, no. 1, pp. 185–207, 2012.

- [156] Y. Fang, C. Zhang, J. Li, J. Lei, M. P. Da Silva, and P. Le Callet, “Visual Attention Modeling for Stereoscopic Video: a Benchmark and Computational Model,” *IEEE Transactions on Image Processing*, vol. 26, no. 10, pp. 4684–4696, 2017.
- [157] Z. Lu, W. Lin, X. Yang, E. Ong, and S. Yao, “Modeling Visual Attention’s Modulatory Aftereffects on Visual Sensitivity and Quality Evaluation,” *IEEE transactions on Image Processing*, vol. 14, no. 11, pp. 1928–1942, 2005.
- [158] D. Yu, J. Fu, T. Mei, and Y. Rui, “Multi-level Attention Networks for Visual Question Answering,” in *Proc. of the IEEE Conference on Computer Vision and Pattern Recognition (CVPR)*, 2017, pp. 4709–4717.
- [159] C. Barat and M.-J. Rendas, “A Robust Visual Attention System for Detecting Manufactured Objects in Underwater Video,” in *OCEANS*. IEEE, 2006, pp. 1–6.
- [160] P. L. Correia, P. Y. Lau, P. Fonseca, and A. Campos, “Underwater Video Analysis for Norway Lobster Stock Quantification using Multiple Visual Attention Features,” in *European Signal Processing Conference*. IEEE, 2007, pp. 1764–1768.
- [161] L. Zhang, B. He, Y. Song, and T. Yan, “Underwater Image Feature Extraction and Matching based on Visual Saliency Detection,” in *OCEANS*. IEEE, 2016, pp. 1–4.
- [162] A. Maldonado-Ramírez and L. A. Torres-Méndez, “Robotic Visual Tracking of Relevant Cues in Underwater Environments with Poor Visibility Conditions,” *Journal of Sensors*, vol. 2016, 2016.
- [163] D. R. Edgington, K. A. Salamy, M. Risi, R. Sherlock, D. Walther, and C. Koch, “Automated Event Detection in Underwater Video,” in *Oceans*, vol. 5. IEEE, 2003, pp. 2749–2753.
- [164] R. Girshick, J. Donahue, T. Darrell, and J. Malik, “Rich Feature Hierarchies for Accurate Object Detection and Semantic Segmentation,” in *Proceedings of the 2014 IEEE Conference on Computer Vision and Pattern Recognition*, ser. CVPR ’14. Washington, DC, USA: IEEE Computer Society, 2014, pp. 580–587. [Online]. Available: <http://dx.doi.org/10.1109/CVPR.2014.81>
- [165] K. Simonyan and A. Zisserman, “Very deep convolutional networks for large-scale image recognition,” *arXiv preprint arXiv:1409.1556*, 2014.
- [166] J. Redmon, S. Divvala, R. Girshick, and A. Farhadi, “You only look once: Unified, real-time object detection,” in *IEEE Conference on Computer Vision and Pattern Recognition*. IEEE, 2016, pp. 779–788.
- [167] Z. Wang, A. C. Bovik, H. R. Sheikh, E. P. Simoncelli *et al.*, “Image Quality Assessment: from Error Visibility to Structural Similarity,” *IEEE Transactions on Image Processing*, vol. 13, no. 4, pp. 600–612, 2004.

# Appendix A

## A.1 Recursive formulation of $\mu^*(T)$

$$\begin{aligned}
\mu^*(T) &= \arg \max_{w_i^{(0:T-1)}} P\left\{G_{0:T} = w_i^{(0:T)} \mid e_{0:T}\right\} \\
&= \arg \max_{w_i^{(0:T-1)}} \left( P\left\{e_T \mid G_{0:T} = w_i^{(0:T)}\right\} \times P\left\{G_{0:T} = w_i^{(0:T)} \mid e_{0:T-1}\right\} \right) \\
&= \arg \max_{w_i^{(0:T-1)}} \left( P\left\{e_T \mid G_T = w_i^{(T)}\right\} \times P\left\{G_T = w_i^{(T)} \mid G_{T-1} = w_i^{(T-1)}\right\} \right. \\
&\quad \left. \times P\left\{G_{0:T-1} = w_i^{(0:T-1)} \mid e_{0:T-1}\right\} \right) \\
&= P\left\{e_T \mid G_T = w_i^{(T)}\right\} \times \arg \max_{w_i^{(T-1)}} \left( P\left\{G_T = w_i^{(T)} \mid G_{T-1} = w_i^{(T-1)}\right\} \right. \\
&\quad \left. \times \arg \max_{w_i^{(0:T-2)}} P\left\{G_{0:T-1} = w_i^{(0:T-1)} \mid e_{0:T-1}\right\} \right) \\
&= P\left\{e_T \mid G_T = w_i^{(T)}\right\} \times \arg \max_{w_i^{(T-1)}} \left( P\left\{G_T = w_i^{(T)} \mid G_{T-1} = w_i^{(T-1)}\right\} \times \mu^*(T-1) \right)
\end{aligned}$$

## A.2 Algorithm for finding optimal motion direction ( $v^*$ )

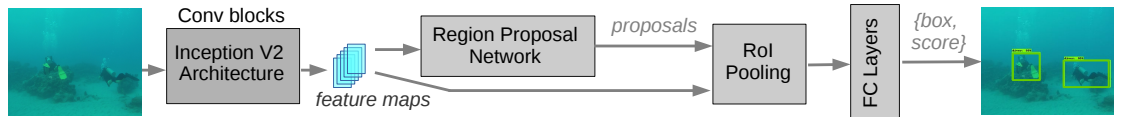
---

- 1: Set values for parameters:  $T, M, p, R$
- 2: Set initial values to dynamic table entries for Markovian
- 3: transition probabilities
- 4:  $t \leftarrow 0$
- 5: **while** Next frame ( $f^{(t)}$ ) is available **do** Define windows:  $w_{i_t}^{(t)}$  for  $i_t = 0 : M - 1$  Formulate evidence vector:  $e_t$
- 6: **if**  $t > 0$  **then** Update dynamic table entries for:
- 7:  $P\left\{G_t = w_{i_t}^{(t)} \mid G_{t-1} = w_{i_{t-1}}^{(t-1)}\right\}$  (for all
- 8:  $(t, t-1)$  pairs, using Equation 3.5)
- 9: **end if** Update dynamic table entries for:  $P\left\{e_t \mid G_t = w_{i_t}^{(t)}\right\}$
- 10: (using Equation 3.6)
- 11: **if**  $t > (T - 1)$  **then** Calculate  $\mu^*(T, p)$  using Equation 3.1.2 Find  $\mathbf{F}(\mu)$  for each  $\mu \in \mu^*(T, p)$  Find  $v^*$  using Equation 3.9 Shift detection window and update  $t$
- 12: **end if**
- 13: **end while**

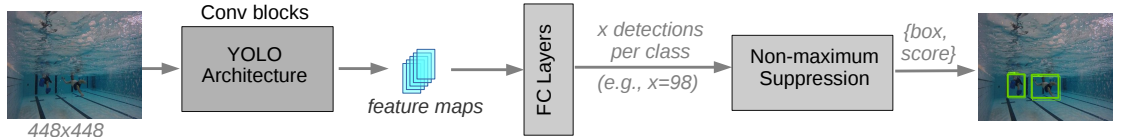
---

# Appendix B

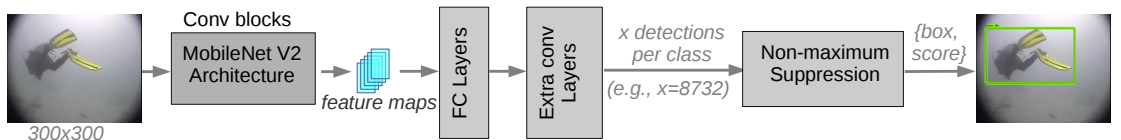
## B.1 Standard deep visual object detection models



(a) **Faster R-CNN with Inception V2**: Faster R-CNN [101] is an improvement of R-CNN [164] that introduces a Region Proposal Network (RPN) to make the whole object detection network end-to-end trainable. The RPN uses the last convolutional feature-maps to produce region proposals which are then fed to the fully connected layers for the final detection. The original implementation of Faster R-CNN uses VGG-16 [165] model for feature extraction. We use Inception V2 [102] model for feature extraction instead, as it is known to provide better object detection performances on standard datasets [36].



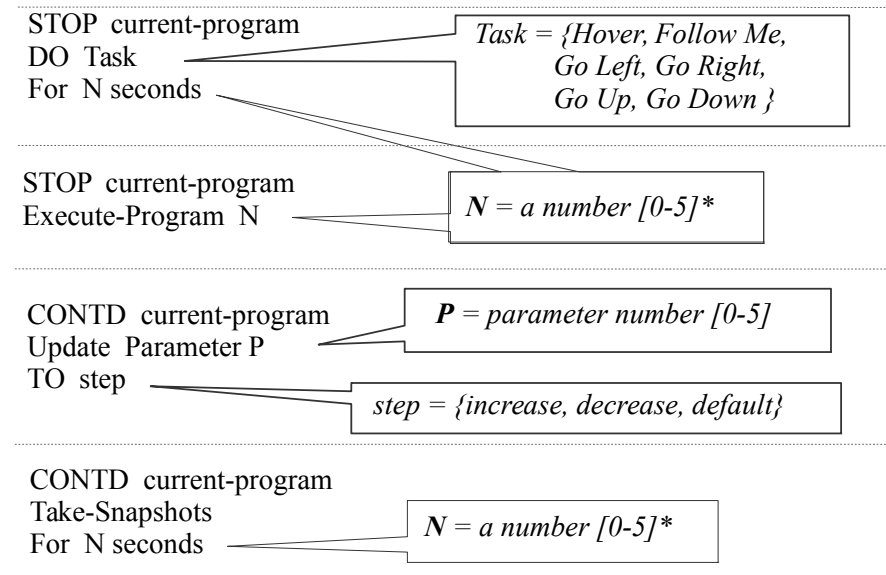
(b) **YOLO V2 and Tiny YOLO**: YOLO models [166, 106] formulate object detection as a regression problem in order to avoid using computationally expensive RPNs. They divide the image space into rectangular grids and predict a fixed number of bounding boxes, their corresponding confidence scores, and class probabilities. Although there are restrictions on the maximum number of object categories, they perform faster than the standard RPN-based object detectors. Tiny YOLO [107] is a scaled down version of the original model having sparser layers that runs much faster compared to the original model; however, it sacrifices detection accuracy in the process.



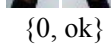
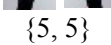
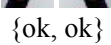
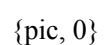
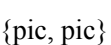
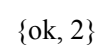
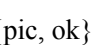
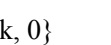
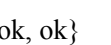
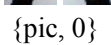
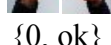
(c) **SSD with MobileNet V2**: SSD (Single-Shot Detector) [103] also performs object localization and classification in a single pass of the network using the regression trick as in the YOLO [166] model. The architectural difference of SSD with YOLO is that it introduces additional convolutional layers to the end of a base network, which results in improved performances. In our implementation, we use MobileNet V2 [104] as the base network to ensure faster running time.

# Appendix C

## C.1 Instruction format in Robo-Chat-Gest



## C.2 Generating instructions using hand gestures

STOP current-program,   {0, ok} {start_token}	HOVER   {5, 5} {task}	For 50 seconds,       {ok, 5} {number}	GO.   {ok, ok} {end_token}
CONTD current-program, take SNAPSHOTS   {pic, 0}	For 20 seconds,         {pic, pic} {ok, 2}	GO.   {ok, ok}	
CONTD current-program, Update Parameter 3   {pic, 0}	DECCREASE,   {3, pic}	GO.   {ok, pic}	
STOP current-program,   {0, ok}	EXECUTE   {pic, 2}	Program 1,   {ok, 1}	GO.   {ok, ok}

# Appendix D

## D.1 Standard performance metrics for image-quality analysis

- i. **Peak Signal-to-Noise Ratio (PSNR):** The PSNR approximates the reconstruction quality of a generated image  $\mathbf{x}$  compared to its ground truth  $\mathbf{y}$  based on their Mean Squared Error (MSE) as follows:

$$MSE(\mathbf{x}, \mathbf{y}) = \frac{1}{mn} \sum_{i=1}^m \sum_{j=1}^n |\mathbf{x}_{i,j} - \mathbf{y}_{i,j}|^2 \quad (D.1)$$

$$PSNR(\mathbf{x}, \mathbf{y}) = 20 \log_{10} [255/MSE(\mathbf{x}, \mathbf{y})].$$

- ii. **Structural Similarity (SSIM):** The SSIM [167] compares the image patches based on three properties: luminance, contrast, and structure. It is defined as:

$$SSIM(\mathbf{x}, \mathbf{y}) = \left( \frac{2\mu_{\mathbf{x}}\mu_{\mathbf{y}} + c_1}{\mu_{\mathbf{x}}^2 + \mu_{\mathbf{y}}^2 + c_1} \right) \left( \frac{2\sigma_{\mathbf{xy}} + c_2}{\sigma_{\mathbf{x}}^2 + \sigma_{\mathbf{y}}^2 + c_2} \right). \quad (D.2)$$

Here,  $\mu_{\mathbf{x}}$  ( $\mu_{\mathbf{y}}$ ) denotes the mean, and  $\sigma_{\mathbf{x}}^2$  ( $\sigma_{\mathbf{y}}^2$ ) denotes the variance of  $\mathbf{x}$  ( $\mathbf{y}$ ); whereas  $\sigma_{\mathbf{xy}}$  denotes the cross-correlation between  $\mathbf{x}$  and  $\mathbf{y}$ . Additionally,  $c_1 = (255 \times 0.01)^2$  and  $c_2 = (255 \times 0.03)^2$  are constants that ensure numeric stability.

- iii. **Underwater Image Quality Measure (UIQM):** The UIQM [130, 131] is a linear combination of three metrics: image colorfulness, sharpness, and contrast. The UIQM is expressed as follows:

$$UIQM(\mathbf{x}) = c_c \times UICM(\mathbf{x}) + c_s \times UISM(\mathbf{x}) + c_m \times UIConM(\mathbf{x}) \quad (D.3)$$

Here, the constant values are  $c_c = 0.0282$ ,  $c_s = 0.2953$ , and  $c_m = 3.5753$ ; We follow the standard definition of Eq. D.3 and relevant procedures for computing UICM, UISM, and UIConM that are described in [12].

# Appendix E

## E.1 Additional qualitative results for SRDRM and SRDRM-GAN

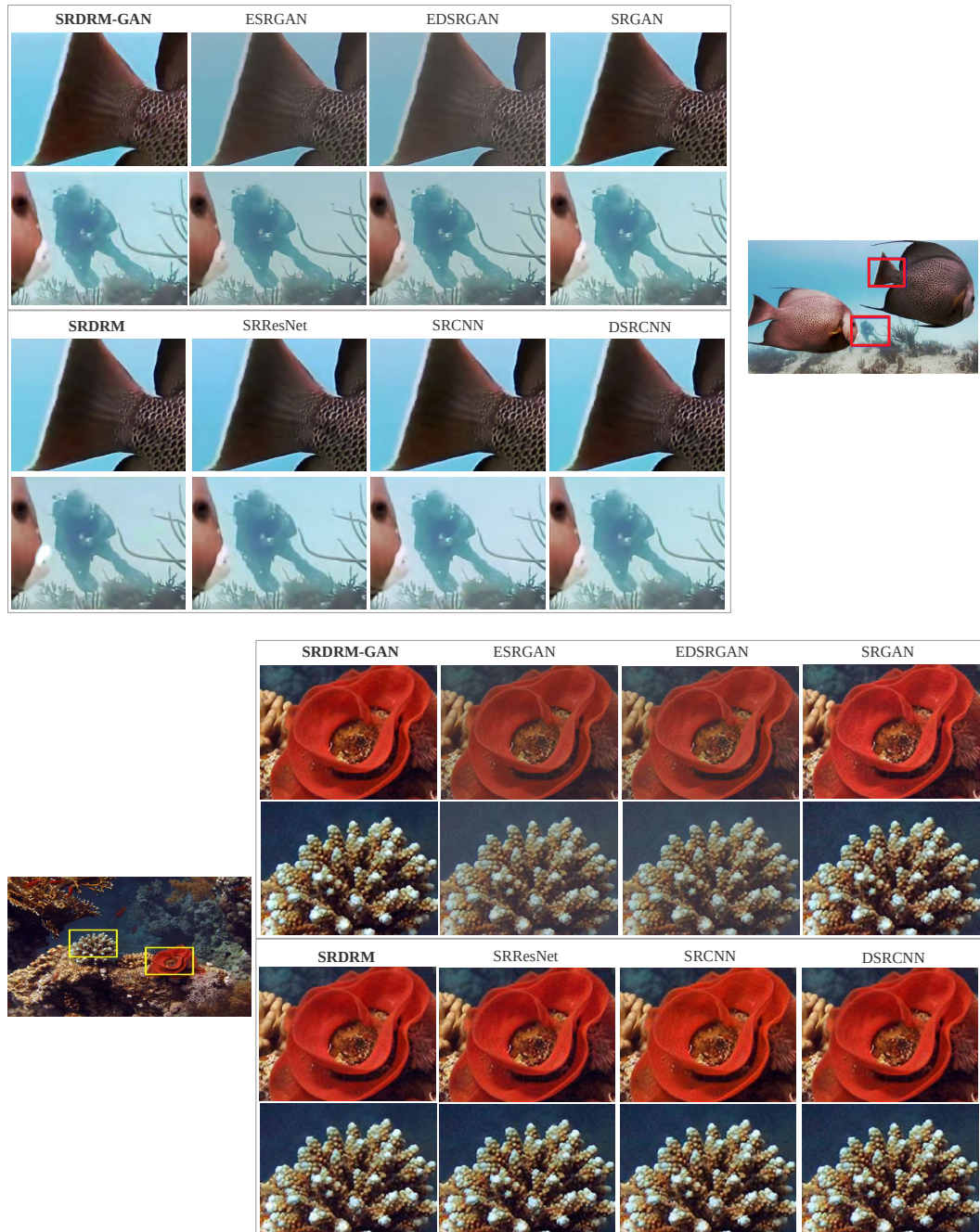


Figure E.1: Qualitative performance comparison of SRDRM and SRDRM-GAN with SRCNN [72], SRResNet [88, 84], DSRCNN [133], SRGAN [88], ESRGAN [89], and EDSRGAN [77].

## E.2 Additional qualitative results for SRDRM and SRDRM-GAN

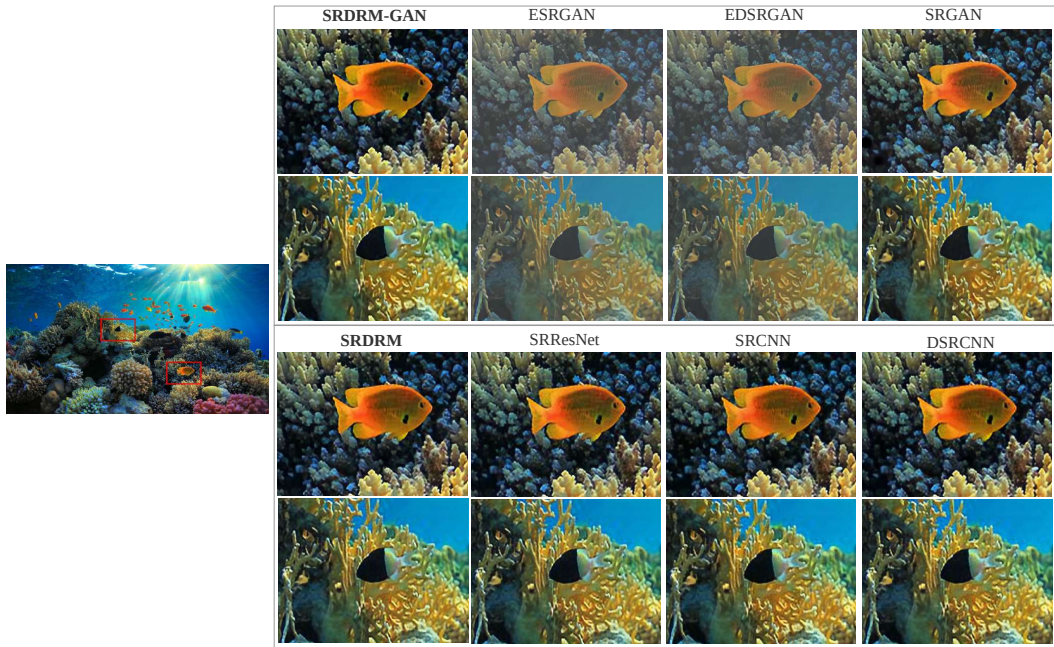


Figure E.2: Qualitative performance comparison of SRDRM and SRDRM-GAN with SRCNN [72], SRResNet [88, 84], DSRCNN [133], SRGAN [88], ESRGAN [89], and EDSRGAN [77].

## E.3 Additional quantitative results for SRDRM and SRDRM-GAN

Table E.1: Performance of  $2\times$ ,  $4\times$ , and  $8\times$  SISR for SRDRM model.

Metric	$2\times$	$4\times$	$8\times$
$PSNR(G(\mathbf{x}), \mathbf{y})$	$26.16 \pm 3.52$	$24.96 \pm 3.36$	$22.83 \pm 2.63$
$SSIM(G(\mathbf{x}), \mathbf{y})$	$0.77 \pm 0.10$	$0.72 \pm 0.11$	$0.66 \pm 0.07$
$UIQM(G(\mathbf{x}))$	$2.47 \pm 0.69$	$2.35 \pm 0.71$	$2.17 \pm 0.55$

Table E.2: Performance of  $2\times$ ,  $4\times$ , and  $8\times$  SISR for SRDRM-GAN model.

Metric	$2\times$	$4\times$	$8\times$
$PSNR(G(\mathbf{x}), \mathbf{y})$	$26.77 \pm 4.05$	$24.77 \pm 3.32$	$22.13 \pm 3.05$
$SSIM(G(\mathbf{x}), \mathbf{y})$	$0.817 \pm 0.07$	$0.70 \pm 0.12$	$0.59 \pm 0.16$
$UIQM(G(\mathbf{x}))$	$2.87 \pm 0.55$	$2.81 \pm 0.56$	$2.77 \pm 0.59$